Preliminary study of the heating mechanism of magnetic nanoparticles for induction welding

Emma Chiavelli

Delft University of Technology

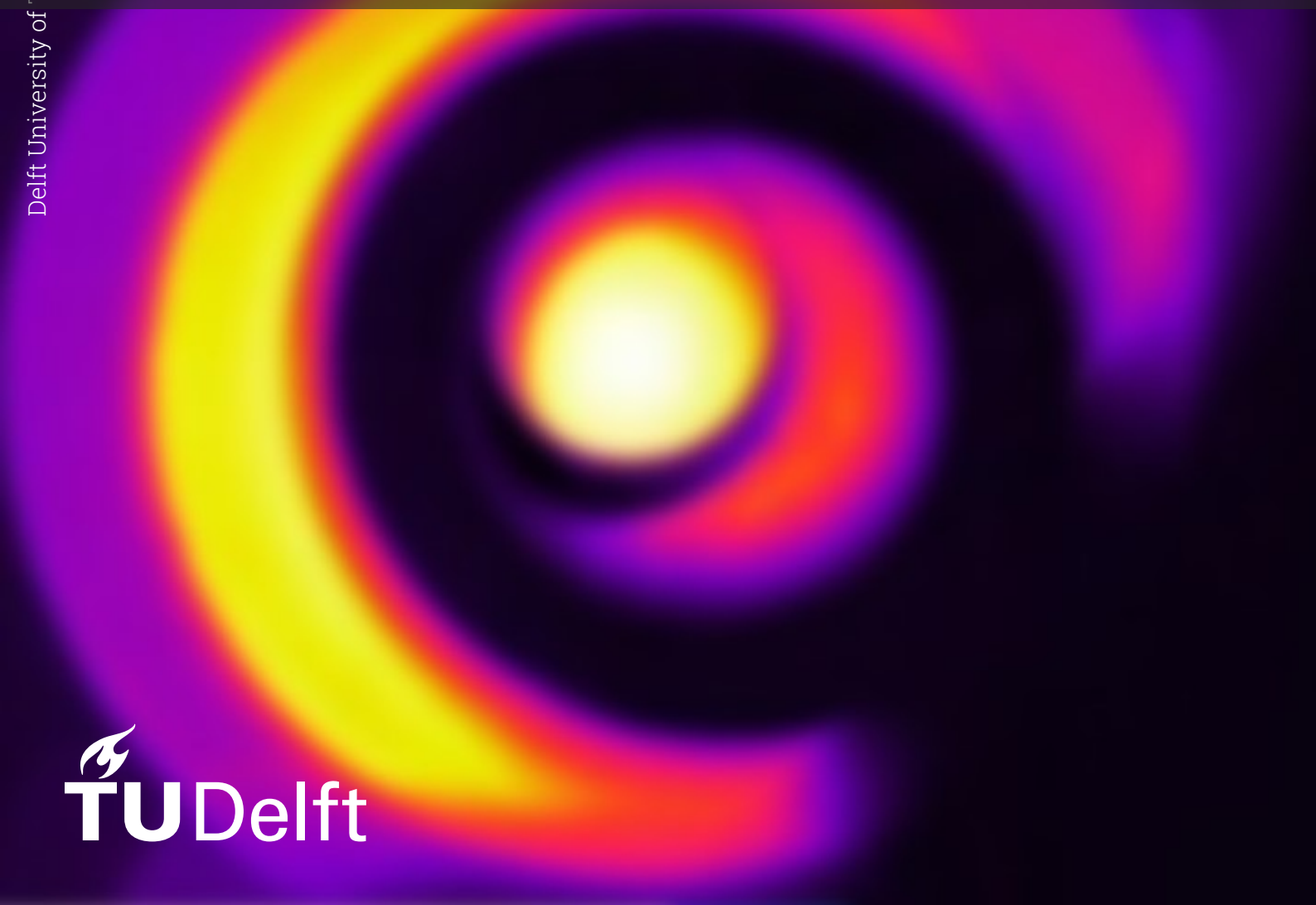

TU Delft

Preliminary study of the heating mechanism of magnetic nanoparticles for induction welding

by

Emma Chiavelli

Student Name	Student Number
Emma Chiavelli	5829941

Thesis committee:	Prof. Clemens Dransfeld, Supervisor
	Dr. Laura Rossi, Co-supervisor
	Dr. Baris Kumru, Chair
	Dr. Rinze Benedictus, External examiner
Project Duration:	June, 2024 - March, 2025
Public defense:	March 3rd, 2025
Faculty:	Faculty of Aerospace Engineering, Delft

Cover: Thermal camera image from induction heating experiment of magnetite suspension (blurred)

TU Delft

Acknowledgements

I would like to express my sincere gratitude to my supervisors, Clemens Dransfeld and Laura Rossi, for their incredible support and guidance during this project. Their experience and kind advice have been an invaluable asset while completing this work. They motivated me when I felt lost and celebrated with me when good results were achieved. I believe the bond we created over these months transcends the thesis itself and I could not be more grateful for this.

Besides my supervisors, I am sincerely thankful to my committee members, Baris Kumru and Rinze Benedictus, for accepting to be there for my defense.

My deepest gratitude goes out to my family, and especially my parents. They have always been my greatest supporters and this master would have not been possible without them. I love you and owe you everything. I will never thank you enough.

I would like to acknowledge and thank Aleksandra Kondakova, Roy Awater, Sharon Chu and Caitlin van den Hondel for their help and support in the lab during testing.

Finally, a special thanks to some people I met during my experience in Delft: my friends from the Study Group, who shed a light upon this rainy country, Dnyandevi, for her advice and help (and uncountable coffees) and finally my friends from BEST Delft. You all have contributed to make these years unforgettable.

Emma Chiavelli
Delft, February 2025

Abstract

The aerospace industry has increasingly prioritized sustainability by adopting lightweight materials, shifting from metal alloys to polymers and polymer composites. Thermoplastic polymers, in particular, are gaining attention due to their recyclability and ease of reshaping. As the demand for high-performance structures grows, advanced joining techniques are becoming essential. Traditional joining methods are expected to be replaced by fusion bonding, with induction welding standing out for its non-contact nature and continuous processing capability. This technique typically relies on susceptors (e.g., metal meshes) to convert electromagnetic energy into heat. However, these materials can cause uneven heating and weaken mechanical properties. Magnetic nanoparticles present a promising alternative as minimally invasive conductive susceptors.
Originally studied for biomedical applications, magnetic nanoparticles generate heat under an alternating magnetic field through hysteresis losses. Researchers have demonstrated their ability to heat polymers above their melting points for induction welding. However, a major challenge is preventing excessive heating, which can degrade thermoplastics. To address this,it was proposed to select ferromagnetic susceptors with Curie temperatures that match thermoplastic processing temperatures. This ensures effective heating while preventing overheating, offering a self-regulating thermal solution for induction welding.

This thesis aimed to gain knowledge on thermal and magnetic capabilities of selected nanoparticles: magnetite (Fe_3O_4), Nickel (Ni), Nickel-Zinc ferrite ($NiZnFe_4O_4$) and Chromium Dioxide (CrO_2). These materials were tested via MagneTherm equipment to identify the optimal induction heating parameters, in terms of strength and frequency of the applied magnetic field. Magnetite showed the best heating capabilities among all particle types, however due to the high detected Curie temperature it does not represent a good candidate for further research. A good alternative was found while testing Nickel and Ni-Zn ferrite nanoparticles. These materials have shown slightly lower heat generation, compensated by Curie temperatures within the range of processing temperatures of multiple thermoplastics, and consequent good potentiality for this application. Further characterization of the particles was performed to gain better understanding on their magnetic and morphological properties and to find correlations with their heating capabilities. In this second part, more traditional techniques such as SQUID, XRD, and TGA were employed.

This study confirms that MNPs are viable candidates for non-contact induction welding in aerospace applications, presenting an efficient alternative to conventional heating methods. Induction heating experiments confirmed the correlation between alternating magnetic field parameters (amplitude, frequency) and power generation. However, further optimization of nanoparticle dispersion, morphology, composition and scalability is required for industrial implementation. Future research should explore alternative nanoparticle compositions, embedding techniques, and evaluate their performance in thermoplastic induction welding prototypes.

Contents

List of Figures

List of Tables

Nomenclature

Abbreviations

Abbreviation	Definition
AMF	Alternating magnetic field
CT	Computed Tomography
DLS	Dynamic Light Scattering
DSC	Differential Scanning Calorimetry
FTIR	Fourier Transform Infrared
HDPE	High Density Polyethylene
ILP	Intrinsic Loss Power
log	natural logarithm
LRT	Linear Response Theory
MNP	Magnetic Nanoparticle
MRI	Magnetic Resonance Imaging
PC	Polycarbonate
PE	Polyethylene
PEEK	Polyetheretherketon
PEI	Polyetherimide
PP	Polypropilene
PPS	Polyphenylene sulfide
PVC	Polyvinyl chloride
SAR	Specific Absorption Rate
SLP	Specific Loss Power
SQUID	Superconducting Quantum Interference Device
TEM	Transmission Electron Microscope
TGA	Thermogravimetric Analysis
TP	Thermoplastic
TS	Thermoset
XRD	X-Ray Diffraction/Diffractometry

Symbols

Symbol	Definition
B	Magnetic induction
C_p	Heat capacity
f	Frequency
H	Field
k_B	Boltzmann constant

Symbol	Definition
K	Anisotropy constant
L	Linear loss parameter
M	Magnetization
M_S	Saturation magnetization
P	Power
T	Temperature
t	Time
V	Volume
V_h	Hydrodynamic volume
η	Viscosity
μ	Magnetic moment
μ_0	Permeability of free space (vacuum)
ρ	Density
τ	Relaxation time
τ_B	Brown relaxation time
τ_N	Neel relaxation time
χ	Susceptibility
χ_0	Initial susceptibility
χ'	Susceptibility (real part)
χ''	Susceptibility (imaginary part)
ω	Cyclic frequency

1 Introduction

1.1. Motivation

Over the last century, the aerospace industry has been increasingly shifting towards sustainability, with a key focus on reducing weight in aircraft components. The production of structural parts, previously relying heavily on metal alloys, is now increasingly favoring polymers and polymer composites to maintain lightweight structures. Particular interest was drawn towards thermoplastic polymers, as they posses recyclability, reshaping, and remolding capabilities. In addition to this, the need for lightweight, high-performance structures in aerospace has driven the development of advanced joining techniques for thermoplastic composites.

The process of joining parts comes with a plethora of complications in terms of weight, design, processing, risks and cost-effectiveness. Because of these reasons, traditional joining techniques, such as mechanical fastening and adhesive bonding, are expected to be fully replaced by fusion bonding (also known as fusion welding) in the next few years [3]. In this context, induction welding is especially promising due to its non-contact nature and potential for continuous processing.
Traditionally, induction welding of thermoplastic parts relies on the presence of a susceptor (a metal mesh or carbon fibres themselves) able to convert electromagnetic energy into heat via Eddy currents. However, additional conductive susceptors may result in non-uniform heating and reduce mechanical properties. A solution to these obstacles may be provided by the introduction of minimally invasive conductive particulate media in the form of magnetic nanoparticles, previously investigated as medical treatment media.

For over fifty years, researchers in the biomedical field have investigated and confirmed the capabilities of magnetic nanoparticles as effective cancer treatment methodologies via heat generation and thermal ablation. The use of these materials for targeted hyperthermia procedures has contributed to the formation of a vast body of knowledge on the topic of magnetic nanoparticles, including the effects of their composition and morphology on heating capabilities.
The functioning principle is straightforward: upon external application of an alternating magnetic field (AMF), magnetic nanoparticles have the capability to generate heat via hysteresis losses, with results depending on their magnetic properties.

Magnetic particles susceptors have been proven to have the ability to heat polymers above their respective melting temperatures [91] when subjected to an external magnetic field. However, one of the key challenges in induction welding is the risk of thermoplastic degradation due to

excessive heating of the susceptor material. Therefore, precise temperature control throughout the welding process is critical. An interesting knowledge gap emerges from these considerations: how can innovative particulate susceptors be designed to thermally self-regulate?
In 2022, Martin et Al. [58] proposed a selection criterion for ferromagnetic particles as susceptor materials in induction welding. This criterion emphasizes the choice of susceptors with Curie temperatures compatible with the processing temperatures of thermoplastic polymers to minimize overheating risks. This allows the material to reach the desired temperature window for processing purposes, while overheating is avoided and limited by the ultimate reachable temperature, i.e. Curie temperature.

This research is aimed at exploring the heating capabilities of various magnetic nanoparticles and their suitability as self-regulating susceptors for induction welding of thermoplastic materials.

1.2. Outline

A short outline of the structure of this thesis report is now given.
After this introductive chapter, an extensive literature review is reported in chapter 2, which is used to provide necessary background information to the reader. An overview of the scope of this research, accompanied by a breakdown of thesis subgoals, is discussed in chapter 3. This part is then followed by chapter 4 and chapter 5, where materials and methodologies used in this research project are clarified. In chapter 6 all relevant thesis outcomes originating from MagneTherm experiments are presented and discussed, while chapter 7 delves into results obtained from other characterization techniques. Discussion of these outcomes is included in the final concluding chapter, chapter 8, in addition to recommendations for future research.
Several appendices with supporting materials and data are provided at the end of this document.

2

Theory and background

This chapter has the main goal of providing a solid and clear background on the topic covered by this study. Comprehension of this research and its findings strongly depends on preliminary knowledge of relevant information and necessary definitions.
An introduction to the topic of magnetic nanoparticles is given from the point of view of their biomedical applications, which serves as inspiration for this research.
After this section, some background on polymers and their properties is provided, followed by a section regarding joining techniques applied to composite/polymeric parts, and focused specifically on the topic of fusion bonding (or fusion welding), particularly relevant for the scope of this thesis. Then, some available literature regarding tests with magnetic nanoparticles susceptors is introduced.
After this, some general information regarding magnetism and magnetic materials is provided, followed by a description of heat generation mechanisms of nanoparticles and of Curie temperature. Finally, methods of tuning the properties of MNPs are discussed.

2.1. The inspiration: application of magnetic nanoparticles in biomedicine

In recent decades, the biomedical applications of MNPs have emerged as effective treatment methodologies, as can be seen summarized in the graphics in Figure 2.1. More specifically, targeted drug delivery, hyperthermia, diagnostic imaging, immunotherapy and tissue regeneration were possible due to the high surface to volume ratio and functionalization capabilities of the nanoparticles. However, to this day, research is still ongoing in order to optimise delivery and functionality of particles for medical treatment.

Magnetic hyperthermia is defined as the capability of MNPs to dissipate heat when exposed to an externally applied alternating magnetic field [106]. The hyperthermia effect of magnetic nanoparticles is used to target diseased areas of the patient's body. In particular, it has been proven as an effective treatment method to to deliver, focus, and destroy cancerous cells via heat application. Considering their higher thermal sensitivity compared to healthy tissues, diseased areas will be more affected by the applied thermal effect. As a result, cancer cells will suffer from precocious apoptosis (or necrosis) under hyperthermia at 42-46 °C [50].
In the 1950s, Gilchrist et al. approached this new cancer treatment technique for the first time: MNPs were injected and heated via application of an alternating field, resulting in the death of cancerous cells present in lymphonodes [59].
This type of medical treatment can be classified based on the area of distribution of the particles of interest. Local, regional, or whole body hyperthermia are all possible methods of application

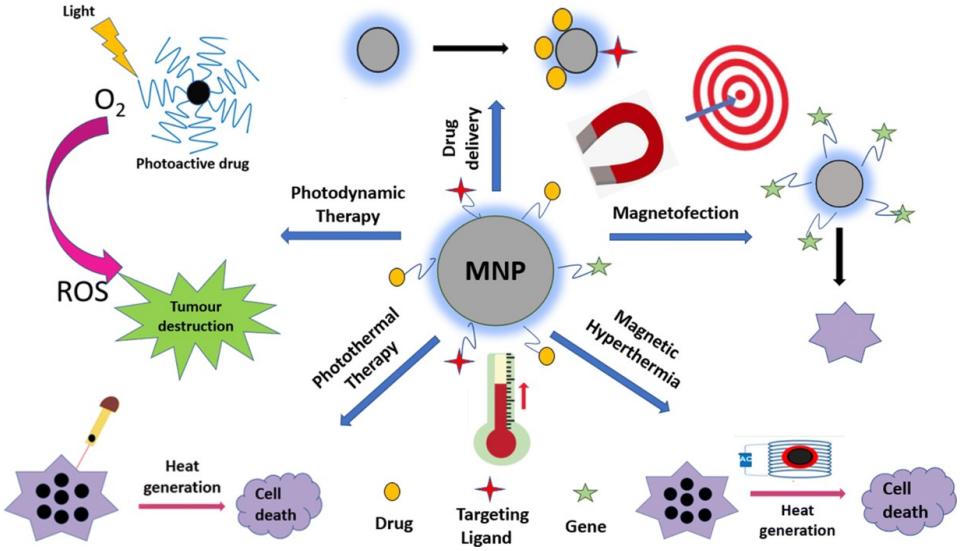

Figure 2.1: Examples of therapeutic applications of magnetic nanoparticles. From Kritika et Al. [65]

of this medical treatment to intervene on diseased cells [61].

In this context, in-vivo testing is particularly relevant, contrary to other applications of MNPs, in the field of medical applications. These experiments investigate not only the functionality of the method, but also any possible side effect or discomfort perceived by the treated patient. This type of tests culminated in the formulation of a medical safety limit value for the applied magnetic field and frequency of $H \cdot f \leq 5 \cdot 10^9$ A/ms [50].

Other possible applications of magnetic nanoparticles include targeted drug delivery and bioimaging. Multiple researchers have used MNPs to perform cancer imaging diagnoses using magnetic resonance imaging (MRI) and computed tomography scans (CT). MNPs are particularly useful as they enhance visibility and allow to capture precise images in-vivo.
As previously mentioned, another relevant aspect of MNPs is their ability to be functionalized in order to be used for specific purposes. For example, Polyethylene Glycol [106] is commonly used to avoid rections by the immune system. Other biocompatible polymers (polysaccharides, linoleic acid etc.) and genes can be used as well.
Moreover, a vast variety of synthesis techniques have been developed to tune properties and composition of magnetic nanoparticles. These techniques include hydrothermal, solvothermal, sol-gel, co-precipitation, flow injection syntheses, electrochemical, and laser pyrolysis techniques [106].

Overall, the proven functionality of magnetic nanoparticles in the biomedical field suggested the possibility of adapting them for other scopes. Specifically, magnetic hyperthermia inspired the possibility of studying the heat generation of MNPs for other purposes, such as performing polymer welding, in the way it was explored in this research.

2.2. Polymers

Over the last century, there has been a revolutionary change in the aerospace sector with respect to materials utilized to build aircrafts and spacecrafts. The production of structural parts, previously relying heavily on metals like aluminum and steel alloys is now increasingly favoring polymers and polymer composites [93]. This shift was promoted by the advantages provided by polymers, which include substantial weight reduction, improved fuel efficiency [4], and better resistance to corrosion and extreme environmental conditions, thereby meeting the industry's growing requirements for efficiency, performance, and cost-effectiveness.

2.2.1. Types of polymer matrices

The term "polymer" identifies a category of materials made out of long chain molecules, consisting of a large number of repeating units.
An initial distinction can be made between different types of polymers that can eventually act as matrices in composite materials. All types of polymers can be classified into two major groups: **thermosets** and **thermoplastics** [26]. These two categories constitute the most significant and widely used classes of polymers within the aerospace field. The presented classification follows both chemical and thermal processing criteria [26], [29].

Thermosets

This class of polymers comprises materials made out of long, crosslinked molecules. Thermosetting materials undergo chemical reactions (commonly called "curing reactions") that cannot be reversed through thermal processing, making them unsuitable for recycling and reprocessing [26]. They offer high thermal and chemical resistance, but degrade at high temperature without softening.
Thermosets have low viscosity during processes at room temperature and solidify as a consequence of curing cycles at specific temperatures and pressures (comparably low to the ones used for thermoplastics). Moreover, they are usually cheap.

Thermoplastics

Thermoplastic polymers, on the other hand, consist of long polymeric chains that exhibit physical entanglements [57]. Linear polymers can undergo consolidation and softening when sufficient heat is applied, making them suitable for repair and recycling.
TPs offer optimal environmental and chemical resistance, combined with good fatigue and corrosion resistance.
They are comparably tougher and less brittle than thermosets. However, TP parts usually require more complicated manufacturing processes, including higher temperatures and pressures needed for forming.

Table 2.1: Mechanical properties of thermoplastic materials used in the aerospace industry [26], [102]

Material	Processing T[°C]	Density [g/cm^3]	Modulus [GPa]	Strength [MPa]
HDPE [79]	180-280	1	1.4	28
PEEK	370-390	1.3	4.1	105
PEI	310-330	1.3	3.6	110
PEKK	360-380	1.3	4.5	102
PP	200-280	0.9	1.3	36
PPS	310-330	1.4	3.8	90
PVC	170-210	1.4	3.3	48

Amorphous and semi-crystalline
An additional subdivision among thermoplastic materials can be made between amorphous and semi-crystalline termoplastics.

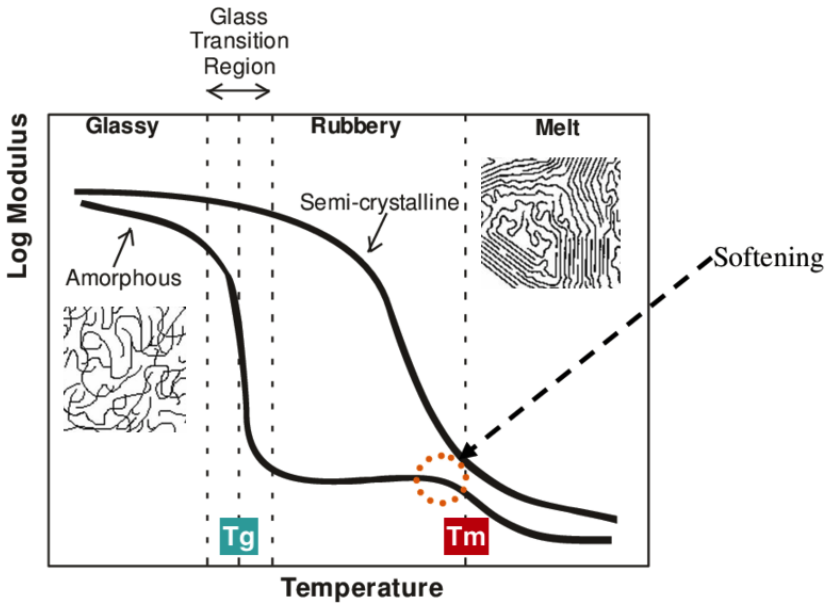

Figure 2.2: Graph showing changes in elastic modulus (log) with temperature of an amorphous and semi-crystalline. From [12], inserts [39]

Amorphous thermoplastics show a random orientation of polymeric chains and a typical glass transition temperature (Tg), corresponding to the transition from solid to rubbery state of the polymer.
Polycarbonate (PC), Polyetherimide (PEI), Polystyrene (PS), Polysulfone (PSU) and Polyvinyl chloride (PVC) are examples of amorphous polymers employed in the aerospace sector.

In contrast, semi-crystalline thermoplastics show various degrees of crystallinity, i.e. they possess partially ordered (folded) polymeric chains [57]. They show two characteristic thermal transitions: Tg and a sharp melting temperature, Tm, corresponding to the melting point of the cystalline phase. These thermal features are shown in Figure 2.2.
Due to their superior chemical resistance, semi-crystalline materials are preferred to amorphous ones for structural applications [57]. Examples of semi-crystalline polymers include Polyethylene (PE), Polyetheretherketone (PEEK), Polyetherketoneketone (PEKK) and Polypropylene (PP).

2.2.2. Joining of thermoplastic parts

The realization of complex aerospace structures requires the assembly of multiple parts. This step comes with a multitude of challenges from the design, processing, and economic perspective.
Asssembly is carried out by employing joining techniques that fall under three broad categories (summarized in Figure 2.3): mechanical fastening, welding and bonding.

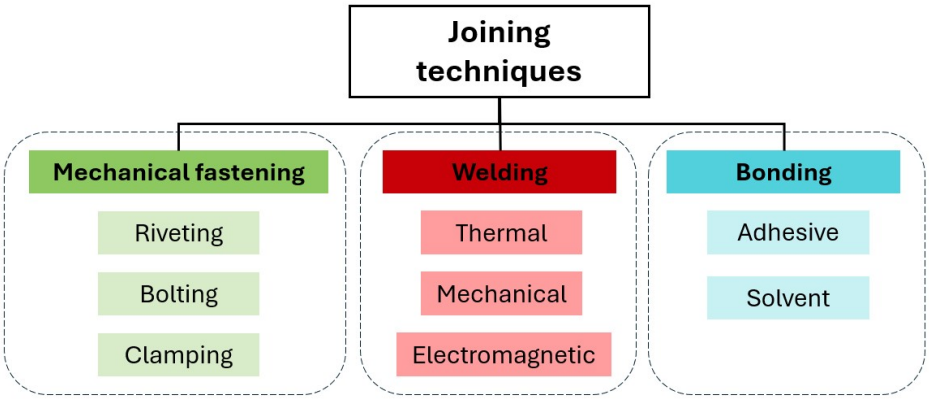

Figure 2.3: Graph summarizing common joining techniques for thermoplastics

Mechanical fastening

This route involves the use of additional elements, such as rivets, bolts, clamps, or screws, to join mechanical parts. Mechanical fastening has been widely applied in the aerospace field since its beginning, being a simple joining technique that allows for disassembly and therefore, reparations.
However, some major disadvantages come with the use of additional mechanical fasteners:

- Weight increase
- Possible galvanic corrosion
- Damages to fibres structures in composites after drilling
- Risk of cracking due to different coefficients of thermal expansion in fasteners and parts
- Stress concentrations due to the presence of holes and fasteners

Overall, integration and assembly of parts is a cumbersome task in terms of complexity, manual labour and costs. In the case of mechanical fastening, for example, it has been reported that assembly costs can account for up to 19-42% of the final cost of the aircraft [107].

Bonding

Bonding techniques (via solvents or adhesives) are historically well known within the aerospace industry and they were already extensively studied by the 1990s [89]. These procedures were initially developed for thermoset composites and metal parts; therefore, they poorly adapted to new thermoplastic parts.
The main challenges of bonding include:

- Surface preparation of adherends
- Difficulties in controlling the bond line
- Long and very specific curing cycles, especially for adhesives

2.2.3. Fusion welding

Unlike thermoset matrices, thermoplastics can be reshaped by heating them to their softening or melting point. This makes them ideal candidates for producing parts that can be repaired and recycled via reprocessing and shaping when end-of-life is reached [26].
Fusion welding takes advantage of these properties of thermoplastics. This joining method can be implemented using various approaches; nonetheless, the procedure involves some common steps:

1. Surface preparation of adherends
2. Heating of interfaces to a suitable temperature (Tg for amorphous TPs and Tm for semi-crystalline TPs)
3. Inter-diffusion of polymerics chains across the weld line (also known as reptation)
4. Cooling down under pressure
5. Consolidation

Overall, fusion welding is considered the ideal joining technique [3]. The main outcome is the disappearance of a recognizable weld line and, as a consequence, the ability to transfer loads through the weld zone and potentially recovering the same mechanical properties as the original TP bulk material. Because of these reasons, multiple researchers believe that fusion bonding is expected to substitute traditional joining methods in the future [3].

Fusion bonding can be carried out by employing various techniques that fall under three broad categories (summarized in Table 2.2): thermal, mechanical and electromagnetic techniques.

Table 2.2: Overview of existing fusion bonding/welding techniques [107]

Thermal	Mechanical	Electromagnetic
Hot gas	Vibration	Resistance
Hot plate	Spin	Induction
Extrusion	Ultrasonic	Dielectric
Infrared	Friction stir	Microwave
Laser		

2.2.4. Induction welding of thermoplastics

Induction welding is particularly promising joining technique for future work, and for this project, as it is a rapid, clean, and non contact joining technique for polymers and composites [9]. It involves the generation of Eddy currents due to the presence of alternating magnetic field provided by an induction coil (as can be seen in Figure 2.4).

This method is traditionally used when the material acts as a susceptor itself, as in the case of composites that incorporate woven textiles of carbon fibers [3]. However, this is not always the case, for example when non-conductive glass fibres are employed. In these cases, conductive inserts need to be introduced to generate Eddy currents and heat dissipation at the weld line. Traditional susceptors for induction heating exist in the form of powder or mesh [3]. Both forms of insert are required to satisfy some basic requirements: being susceptible to the presence of an external magnetic field, having sufficient electrical resistance, and being able to provide a closed circuit to generate Eddy currents [3]. Traditional metal mesh susceptors are efficient media to generate and concentrate heat in the area; nonetheless, they are quite extended and may result in reduced mechanical properties. A solution to these issues may be provided by particulate susceptors, in the form of micro- and nanoparticles.

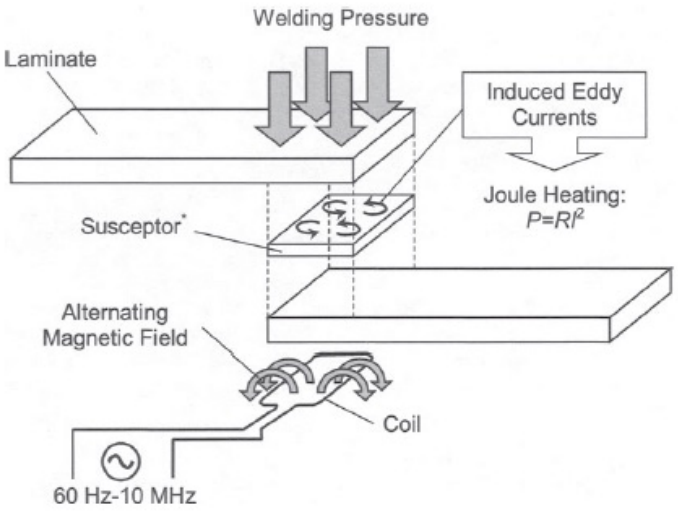

Figure 2.4: Induction welding setup for induction welding via induced Eddy currents. From [3]

Particulate susceptors

A novel approach to fusion bonding offers the possibility to disperse magnetic particles at the interface to be bonded, acting as a substitute for traditional susceptors. In this case, because of the ferromagnetic character of the particles, the main heat generation mechanism comes from hysteresis losses rather than Eddy currents and Joule losses.

The primary benefit of this technique lies in the size of the particles used. Moreover, in this case, the shaping of the material is not hindered by macroscopic metallic susceptors. The flowability and rheology of the polymer matrix are minimally altered, allowing processing through molding, extrusion, and compounding [101].

More recently, researchers have also been trying to fabricate TP adhesive films that incorporate magnetic particles that have inductive heating behavior. In the experiments conducted by Bayerl et al. [11], HDPE and PA6 were compounded with the addition of iron and iron oxide microparticles to produce films.

An overview of available experimental studies involving particulate susceptors for induction welding of TP matrices is provided on the following page in Table 2.3.

Influence of particles concentration
Inductive behavior of magnetic nanoparticles has been studied in relation to the concentration of particles. In the vast majority of available literature, it has been proven that a higher concentration of particles correlates with improved heating efficiency.
Lm et al. [53] found that, for Ni particles embedded in a TPU matrix, the highest final temperature is achieved for the highest used Ni concentration (20 phr in this case). Similar results were obtained by Suwanwatana et al. [91], [90] for Ni particles incorporated in PSU specimens.
In the case of magnetite (Fe_3O_4) particles Bae et al. [8], [7] and Bayerl et al. [11] highlighted a similar behavior, showing higher temperatures and increased generation for increased particle contents.

Influence of particles size
Size of nanoparticles has been reported to dramatically affect the heating behavior at the weld line.
Bae et al. [8], [7] found that heating rate and final temperature were much higher for both Fe and Fe_3O_4 microparticles with higher particle dimensions.
However, when particles in the nm range were compared to microparticles, the trend appeared to be reversed. Final temperatures of specimens, reached at the Curie temperature of the particles, were reached much faster when smaller particles were employed. This was proven for Ni particles in PSU resin [91], [90] as well for Ni, Fe and Fe_3O_4 nanoparticles in TPU [47].

Influence of frequency
Bayerl et al. [11] investigated the effects of frequency on heat generation for an HDPE film containing iron particles at 5% wt. The tests were conducted between 290 and 565 kHz, and found an optimal heating efficiency in the 430-450 kHz range.
Differently, Suwanwatana et al. [91] found a linear correlation between frequency and heating rates and final temperature. Nickel particles in a PSU matrix were subjected to 2.25, 3.45, 4.48 and 7.05 MHz frequencies and their heating profiles were recorded, revealing the highest heating rate and final temperature (350°C) in response to the highest applied frequency.

Table 2.3: Table summarizing available literature on magnetic particles used for induction heating of thermoplastics

Particles type	Particles size	Concentration	Polymer matrix	Frequency [kHz]	Power [kW]	Max T [°C]	Source
Ag	10-25 nm	-	PPS	150-450		400	[28]
Co ferrite	2.52 μm	-	-	5850	-	316	[108]
Fe	8, 43, 74 μm	5, 10, 15, 20 phr	PU	750	2, 3.5, 5	153	[8]
Fe	100 nm and 8, 43, 74 μm	10, 20 phr	PU	750	2, 3.5, 5	254	[47]
Fe	125-300 μm	5, 10, 20 %	HDPE	430, 2500	7	280	[11]
Fe	125-300 μm	5, 10, 20 %	PA6	430, 2500	7	250	[11]
Fe_3O_4	25-125 μm	5, 10, 20 %	HDPE	430, 2500	7	160	[11]
Fe_3O_4	25-125 μm	5, 10, 20 %	PA6	430, 2500	7	220	[11]
Fe_3O_4	200 nm	50, 67, 75, 80 %	PA6 + CF	100	3.4	350	[9]
Fe_3O_4	270 nm and 2, 9 μm	10, 20 phr	PU	750	5	263	[47], [7]
Fe_2O_3 silica matrix	20-26 nm	5, 7.5, 10 %	PU copolymer	258	-	90	[62]
Ni	79, 700 nm	0.1, 0.2 vf	PSU	2-7 MHz	20	350	[91]
Ni	3, 22 μm	0.1, 0.2 vf	PSU	2-7 MHz	20	338	[90]
Ni	70 nm and 1, 20, 70 μm	10, 20 phr	PU	750	5	226	[47]
$NiFe_2O_4$	2.85 μm	-	-	5850	-	335	[108]

2.3. Principles of magnetism

Human interest in magnetism and its correlated phenomena has been shown since 2500 BC, when it is speculated that the Chinese used some primordial type of compass for navigation. In ancient Greece, philosophers such as Thales and Socrates have reportedly explored permanent and induced magnets [63]. This shows how magnetism has been intrinsically part of human history since its discovery.
More recently, in the past two centuries, extensive research and exploration of this subject has been performed, generating a consistent body of knowledge regarding magnetism and its applications. In order to orient the reader, this section is dedicated to providing a solid background on the topic, introducing existing classes of magnetic materials and the necessary properties used to define the phenomenon.

2.3.1. General properties of magnetic materials

Some basic, but relevant, definitions used in magnetism are worth mentioning for future use. The concepts of magnetisation, magnetic induction, applied field, permeability, saturation magnetisation, retentivity, coercivity, and susceptibility are introduced and defined here [40]. In order to obtain these properties, magnetisation loops, like the one in Figure 2.5, are realised by recording the magnetization behaviour of a (ferromagnetic) material when exposed to an external field of strength H.

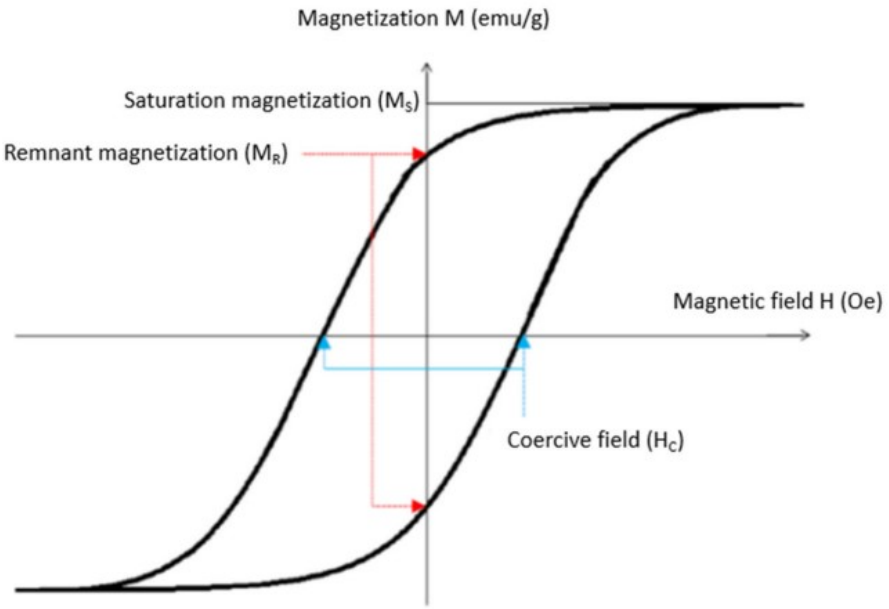

Figure 2.5: Diagrams of hysteresis loops with magnetic properties. From [30]

Magnetization and magnetic induction

Whenever a material having intrinsic magnetization M (A/m) is exposed to a magnetic field of strength H (expressed in A/m or Oe), the resulting magnetic induction B (in Tesla, T) can be calculated as follows:

$$\mathbf{B} = \mu_0(\mathbf{H} + \mathbf{M}) \tag{2.1}$$

The net magnetization vector **M** represents the density of magnetization within the bulk material and it is calculated by averaging the magnetic moment over the bulk volume:

$$M = \frac{\mu}{V} \tag{2.2}$$

Permeability
Permeability quantifies the measure of the material's ability to conduct a magnetic field. It is represented by the Greek letter μ and is defined as the ratio of the magnetic flux density (B) to the magnetic field strength (H):

$$\mu = \frac{B}{H} \tag{2.3}$$

Saturation magnetization
The upper limit in terms of magnetization is defined by saturation magnetization, commonly identified by M_s or M_0. When a magnetic field of strength H is applied to a material, saturation is reached when all the magnetic moments within a material are oriented parallely to the externally applied field.

Retentivity or remnant magnetization
Upon removal of the applied magnetic field, ferromagnetic materials have the ability to partially retain part of the magnetization. After reaching saturation, ferromagnets show a remanence, or a residual magnetization (M_R) and its corresponding remaining induction (B_R):

$$B_R = \mu_0 M_R \tag{2.4}$$

Coercivity
The coercive field or magnetic coercivity parameter (H_c) identifies the strength of an externally applied magnetic field to reduce magnetic induction and/or magnetization to zero.
Moreover, coercivity is used to distinguish "soft" (low coercivity) from "hard" ferromagnets.

Susceptibility
An additional parameter related to magnetism is susceptibility. It is used to identify the response of a material when exposed to a magnetic field in terms of attraction or repulsion [64]. It is calculated as the dimensionless ratio of material magnetisation (M) to the applied magnetising field intensity (H):

$$\chi = \frac{M}{H} \tag{2.5}$$

As magnetization cannot be directly measured, susceptibility constitutes an important parameter to evaluate the average bulk magnetic moment of materials [77]. A negative susceptibility is typical of diamagnetic materials, which are weakly repelled by the field. Both paramagnetic and ferromagnetic (high χ) materials show positive values for susceptibility.

2.3.2. Classes of magnetic materials

The origin of magnetism lies in the existence of atoms with unpaired electrons. The presence of an incomplete electronic configuration allows each unpaired electron to generate a magnetic field due to two phenomena [72]:

- Intrinsic spin: each electron has an intrinsic angular momentum called spin (of value $\pm 1/2$), which generates a magnetic moment and acts as an indipendent magnet
- Orbital motion: electrons revolving around the nucleus set up circular currents that generate magnetic fields

Materials are generally classified according to their magnetic properties. Paramagnetic, antiferromagnetic, and diamagnetic materials, or "weak" magnetic materials, show no spontaneous magnetization in a zero field. In contrast, classes of materials showing spontaneous magnetisation ("strong" magnetism) include ferromagnetic, ferrimagnetic, and superparamagnetic

materials [22].
Graphics showing electronic spin configurations and hysteresis loops of the analyzed classes of materials can be examined below in Figure 2.6 and Figure 2.7.

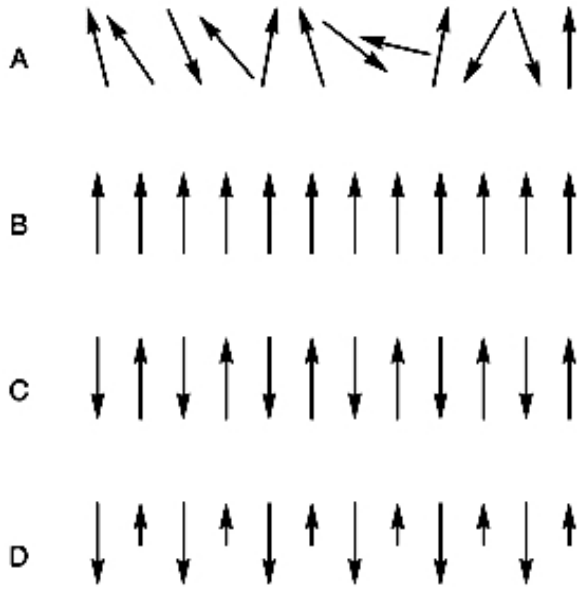

Figure 2.6: Orientation of electronic spins for different types of magnetism: A) Paramagnets, B) Ferromagnets, C) Antiferromagnets, D) Ferrimagnets. From [55]

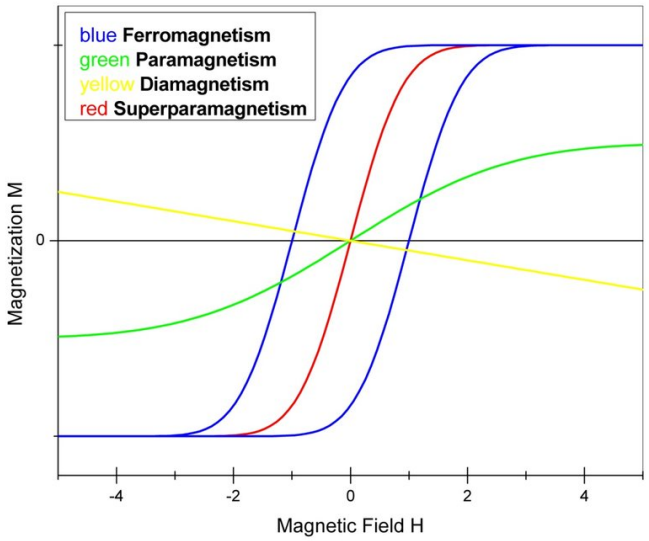

Figure 2.7: Diagrams of hysteresis loops for differents of magnetic materials. From [96]

Paramagnetism

Paramagnetism is observable for materials that possess uncoupled electrons in their external orbitals, and therefore a very weak permanent magnetic momentum [63], [80]. Overall, magnetic moments are disordered in zero field and their orientation is randomized among magnetic domains. Once an external field is applied, high order magnetization temporarily

appears and the overall magnetic moment of the material is aligned with the applied field. They possess a very small positive susceptibility [87].

Ferromagnetism
Ferromagnetism is recognizable in solid materials showing high alignment of their magnetic moments within magnetic domains. This class of materials shows high susceptibility and a characteristic temperature (named the Curie temperature), at which they suddenly switch their behavior to paramagnetism. Below Curie temperature, ferromagnets show homogeneous magnetization within a single domain and an inhomogeneous magnetization from domain to domain in the absence of external magnetic field. Upon application of a field, long range alignment becomes observable and all magnetic moments within all domains flip parallel to the field. Ultimately, ferromagnets possess a net magnetization in zero field (from this comes the expression "permanent magnets").
Ferromagnetic behavior is typical of Cobalt, Iron, Nickel, some rare earth elements, and their alloys.

Diamagnetism
Diamagnetism can be observed when repulsion of a material results upon application of an external magnetic field [1]. In this case, all atoms have coupled electrons (i.e., no net magnetic moment); therefore, no magnetic moment of the particle is naturally present, and an opposing field originates when an external field is applied (consequently, a negative susceptibility is measured [1]). Overall, no long or short order magnetization is observable after removal of the field.

Antiferromagnetism
Materials consisting of two magnetic sublattices, having equal magnetic moment but opposite direction and resulting in zero net magnetization [1]. In this case, negative exchange interactions between neighboring atoms appear [63]. Moreover, antiferrromagnetic materials follow Curie-Weiss law for susceptibility above their critical Néel temperature [1].

Ferrimagnetism
Ferrimagnets, similarly to anitferromagnets, consist of two sublattices that provide opposite magnetic moments of different intensities. Hence, a net magnetic moment is present.
Additionally, ferrimagnets present all characteristic features of ferromagnets, such as spontaneous magnetization, Curie temperatures, hysteresis, positive susceptibility, and remanence. Magnetite is the most well-known ferrimagnet.

Table 2.4: Summary of characteristics of magnetic materials classes

	Net M	**Field response**	**Spin arrangement**	χ	**Curie temperature**	**Néel temperature**
Paramagnetic	weak	weak	random	small >0	no	no
Ferromagnetic	strong	strong	parallel	>0	yes	no
Diamagnetic	none	weak	none	<0	no	no
Antiferromagnetic	none	weak	anti-parallel	small >0	no	yes
Ferrimagnetic	yes, varies	strong	anti-parallel	>0	yes	no

2.4. Heat generation

As introduced by Vallejo-Fernandez et al. [97] various types of heat generation mechanisms are possible when dealing with colloidal magnetic nanoparticles, depending on their size and parameters of the applied magnetic field.

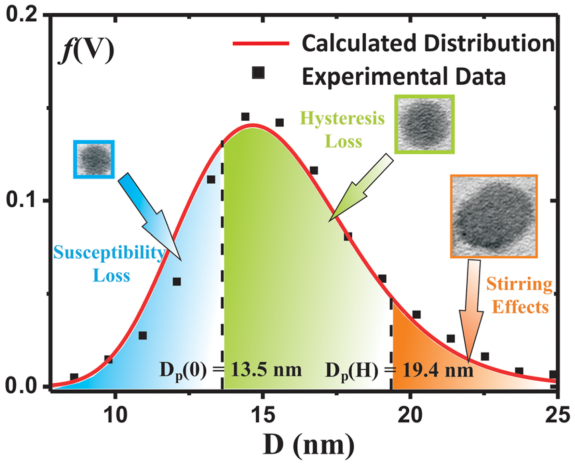

Figure 2.8: Distribution of heating contribution vs. critical diameters for magnetite nanoparticles tested at a frequency of 111.5 kHz and an applied field of 250 Oe [98]

The conversion of magnetic field energy into heat as a result of magnetization reversal, commonly known as magnetic losses, is caused by processes occurring in the particle system [36]. As can be seen from Figure 2.8 three possible heating mechanisms exist, depending on the diameter of the considered nanoparticle: susceptibility loss (comprising Neel and Brown relaxations), hysteresis loss, and viscous heating (or stirring effect).

Susceptibility losses are commonly identified as the heat generation mechanism developed by magnetic nanoparticles in the superparamagnetic size range, whose maximum diameter was identified by Vallejo-Fernandez et al. [97] by the following equation:

$$D_p(0) = \left(\frac{6k_B T \ln(t f_0)}{\pi K} \right)^{1/3} \tag{2.6}$$

Where k_B is the Boltzmann constant, T the temperature, t the measuring time, f_0 the characteristic frequency of the order of $10^9 - 10^{13}$ Hz and K the effective anisotropy density constant.

Hysteresis loss, on the other hand, is predominant for bigger particles with ferromagnetic behaviour, falling within the single domain category, up to their limit with the multidomain size range, defined by the critical size:

$$D_p(H) = \left[1 - \frac{HM_s}{0.96K} \right]^{-2/3} D_p(0) \tag{2.7}$$

Where H indicates the applied field and M_S the saturation magnetization.

2.4.1. Magnetic domains and critical sizes of magnetic nanoparticles

As it was just introduced, magnetic nanoparticles can be classified according to their size and magnetic behaviour as superparamagnetic, mono-domain and multi-domain nanoparticles. This can be seen summarized below in Figure 2.9.

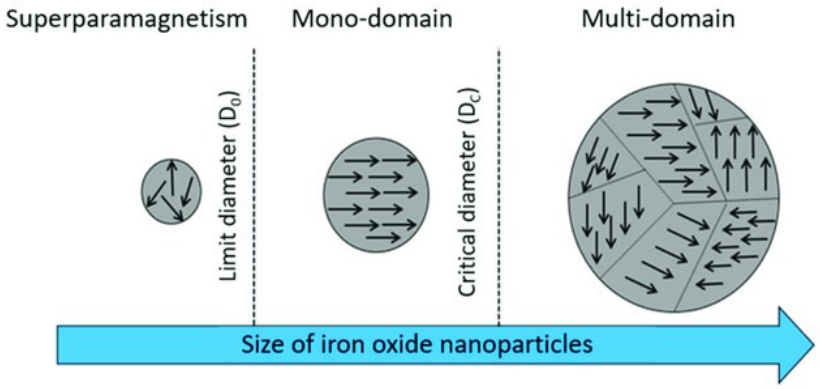

Figure 2.9: Magnetic distribution of magnetic domains according to their particle size. From [30]

The dimensionless parameter σ can be used to better describe the features of the three type of magnetic behaviours [2]:

$$\sigma = \frac{KV_{MNP}}{k_B T} \tag{2.8}$$

Where K identifies the anisotropy constant, V_{MNP} the volume of nanoparticles, k_B the Boltzmann constant and T the temperature.

The parameter σ allows us to efficiently describe when the formation of domain walls in nanoparticles is favourable. Regions where magnetic dipoles are aligned in the same direction are identified as magnetic domains and are delimited by domain walls (Neel and Bloch walls). The formation of domains is a complex phenomenon and is influenced by multiple factors, including composition, size and shape of the particles.

In the case of large nanoparticles ($\sigma >> 1$), the formation of domain walls is more favourable because it minimises the magnetostatic energy of the particle, originating multi-domain nanoparticles. Below a critical size, the formation of multiple domains does not minimize the magnetostatic energy of the material, therefore single domain nanoparticles will be originated. The critical size of transition between these two behaviours is commonly identified to be in the 2-100 nm size range [21], however, this property is material-dependent (some examples are given in Figure 2.10) and no universal law to identify the critical diameter can be established. In the case of mono-domain, the entire particle acts as one large magnetic dipole and a strong ferromagnetic behaviour is exhibited (high coercivity and remanence).

For even smaller diameters, σ is below 1, indicating a superparamagnetic behaviour. In this size range the atomic vibrational (thermal) energy is sufficient to overcome the anisotropy energy (KV_{MNP}) and the magnetic spins are free to rotate, originating magnetic nanoparticles that do not show any hysteresis or coercivity (also identified as "unblocked" nanoparticles).

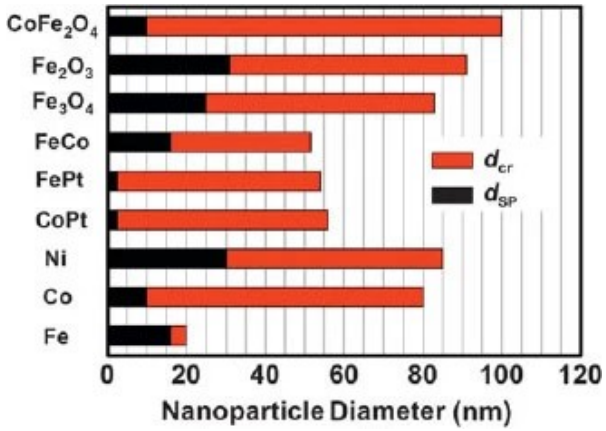

Figure 2.10: Critical diameters for superparamagnetic and mono-domain behaviours for various materials. From [56]

According to the previously identified categorization of nanoparticles as superparamagnetic, single-domain and multi-domain, empirical methods have been identified to model their heat generation capabilities. Through previous literature, Cobianchi et Al. [16] identified three main models (summarized in Figure 2.11): the Linear Response Theory (LRT), the Stohner-Wohlfarth model and Rayleigh's model.

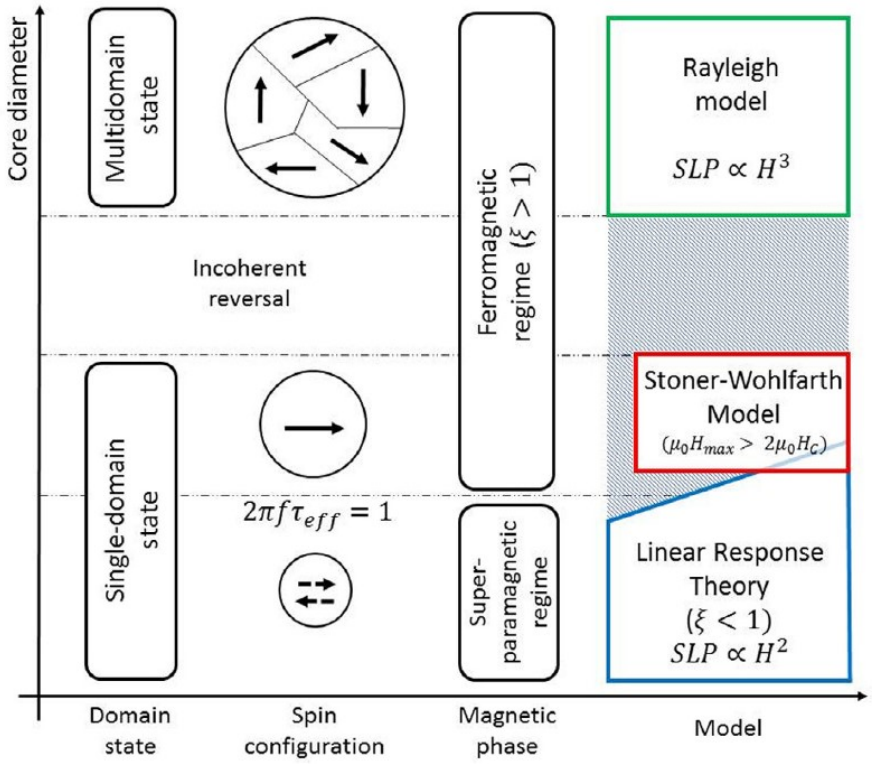

Figure 2.11: Summary of empirical models identified in literature to describe heating mechanisms of various sizes of magnetic nanoparticles. From [16]

The Linear Response Theory is vastly applied in literature regarding hyperthermia and magnetic nanoparticles. As a consequence, a parameter was established to limit and identify

its applicability:

$$\xi = \frac{\mu_0 M_s V H}{k_B T} < 1 \tag{2.9}$$

Where M_s indicates magnetic saturation, V the volume of nanoparticles, H the applied field, k_B the Boltzmann constant and T the temperature. The ξ parameter identifies the boundaries of linear dependence of magnetization M from the applied field H, and, as a consequence, the square proportionality ($SLP \propto H^2$) of power generation from H [16].

The heat generation of a dispersion of magnetic nanoparticles in the susperparamagnetic regime is correlated to the evolution of the imaginary part of its susceptibility ($\chi = \chi' - i\chi''$). The imaginary part identifies the out-of-phase response of the magnetic moments in a material and it is expressed as [82]:

$$\chi'' = \chi_0 \frac{\omega\tau}{1 + (\omega\tau)^2} \tag{2.10}$$

Where χ_0 is the initial susceptibility, τ the relaxation time of MNPs and $\omega = 2\pi f$ is the cyclic frequency of rotation of nanoparticles. χ'' is also often identified as loss susceptibility. The evolution of both in-phase and out-of-phase susceptibility can be observed below in Figure 2.12.

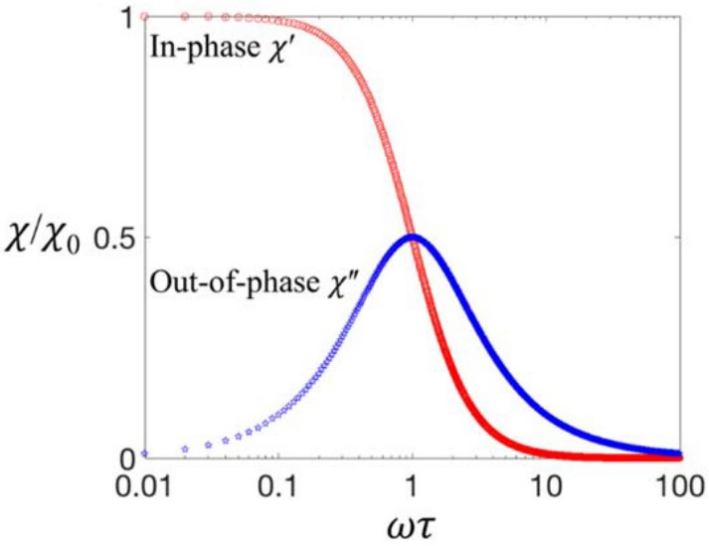

Figure 2.12: Normalized in-phase and out-of-phase components of susceptibility as a function of $\omega\tau$. From [104]

Consequently, the out-of-phase component χ'' can be used to compute the volumetric power dissipation of the ferrofluid:

$$P = \pi \mu_0 H^2 \chi'' f \tag{2.11}$$

Where μ_0 identifies the permeability of vacuum, H the strength of the applied magnetic field, χ'' the loss susceptibility and f the frequency.

2.4.2. Neel and Brown relaxation mechanisms

Under the assumption of superparamagnetism, single domain and noninteracting particles, heat dissipation happens due to two possible phenomena: Neel or Brown relaxation (identified below in Figure 2.13).

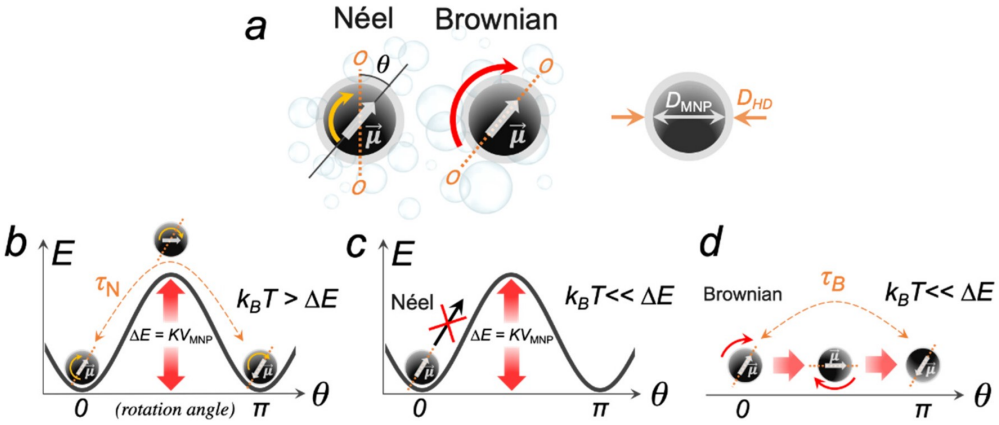

Figure 2.13: a) Neel and Brown relaxation, b) Neel relaxation aided by thermal energy, c) Neel relaxation in zero field, d) Brownian relaxation in a fluid. From [70]

All magnetic particles show magnetic anisotropy and, as a result, preferential orientations of their magnetic moments. When subjected to an external magnetic field, MNPs tend to orient accordingly to it, aligning their magnetic moments parallel to the field lines. In the case of an alternating magnetic field, generated by AC field, magnetic nanoparticles have an intrinsic tendency to realign. However, Neel relaxation occurs whenever the magnetic moment of a nanoparticle flips to accommodate the externally applied field and can be expressed as [104]:

$$\tau_N = \tau_0 \exp\left(\frac{KV_{MNP}}{k_B T}\right) \tag{2.12}$$

Where τ_0 is a preexponential time factor of the order of $10^{-9} - 10^{-13}$ s, the exponential numerator $\Delta E = KV_{MNP}$ is the anisotropy energy barrier, comprising the effective anisotropy density constant (K) and the volume of the particles (V_{MNP}), the denumenator represents the thermal contribution and is obtained by multiplying the Boltzmann constant by the testing temperature.

Anisotropy

The anisotropy energy barrier expression was reworked by Bødker et al. [14] in order to obtain a clear relation with surface anisotropy for (assumed) spherical nanoparticles of size d:

$$\Delta E = KV_{MNP} = K_V V + K_S S = K_V + \frac{6}{d} K_S \tag{2.13}$$

Where K_V identifies the anisotropy density constant correlated to the volume of the particle, while K_S the one connected to surface effects.

Magnetic anisotropy in magnetic nanoparticles refers to the directional dependence of a material's magnetic properties. This means that the magnetic characteristics of the nanoparticles, such as their magnetization and hysteresis behavior, vary based on the direction in which they are measured. There are several types of magnetic anisotropy. Magnetocrystalline

anisotropy is due to the intrinsic properties of the crystal structure of the material, where the magnetization tends to align along specific crystallographic directions, known as "easy axes". Shape anisotropy arises from the physical shape of the nanoparticles. Elongated or irregularly shaped particles can have a preferred direction of magnetization due to their geometric configuration. Lastly, surface anisotropy is particularly significant in nanoparticles due to their high surface-to-volume ratio, where surface effects can contribute to the overall magnetic anisotropy. Considering the small diameters of magnetic nanoparticles, the surface anisotropy term becomes particularly relevant in this context.

In the presence of an applied magnetic field H, Equation 2.12 can be modified to include this contribution, as follows:

$$\tau_N = \tau_0 \exp\left(\frac{KV_{MNP} - MH}{k_B T}\right) \tag{2.14}$$

Finally, the effective Neel relaxation time for magnetic nanoparticles dispersed in a fluid, while taking into consideration the presence of polidispersity, can be expressed by the integral:

$$\tau_N^{\text{eff}} = \int_0^{V_p^{(0)}} \tau_N(V) f(V)\, dV \tag{2.15}$$

Where $V_p^{(0)}$ is the particle volume at the critical diameter $D_p(0)$ and $f(V)$ is a statistical distribution function representing the volume distribution of particles in the ferrofluid.

The other relaxation phenomenon is commonly known as 'Brown relaxation'. It is typically observed when ferrofluids are analysed, as it describes the type of physical rotation exhibited by a magnetic nanoparticle while suspended in a fluid. In this case, the effective magnetic moment realigns, according to the applied magnetic field, by physically rotating the whole particle. This type of re-orientation spontaneously occurs with frequency τ_B, as follows [104]:

$$\tau_B = \frac{3\eta V_h}{k_B T} \tag{2.16}$$

Where τ_B is the Brown relaxation time, η the fluid viscosity, V_h the hydrodynamic volume of each particle, k_B the Boltzmann constant and T the absolute temperature.

The effective Brownian relaxation time for magnetic nanoparticles dispersed in a fluid, when polidispersity is present, is expressed by the integral:

$$\tau_B^{\text{eff}} = \int_0^{V_h(0)} \tau_B(V_h) f(V_h)\, \mathrm{d}V_h \tag{2.17}$$

Where $V_h(0)$ is the hydrodynamic volume at the critical diameter $D_p(0)$ and $f(V_h)$ is a statistical distribution function representing the hydrodinamic volume distribution of particles in the ferrofluid.

Overall, the effective relaxation time when both effects are present (for example, in the case of a suspension of MNPs) is shown in Figure 2.14 and can be calculated as follows:

$$\frac{1}{\tau_{\text{eff}}} = \frac{1}{\tau_{\text{B}}} + \frac{1}{\tau_{\text{N}}} \tag{2.18}$$

$$\tau_{\text{eff}} = \frac{\tau_B \tau_N}{\tau_B + \tau_N} \tag{2.19}$$

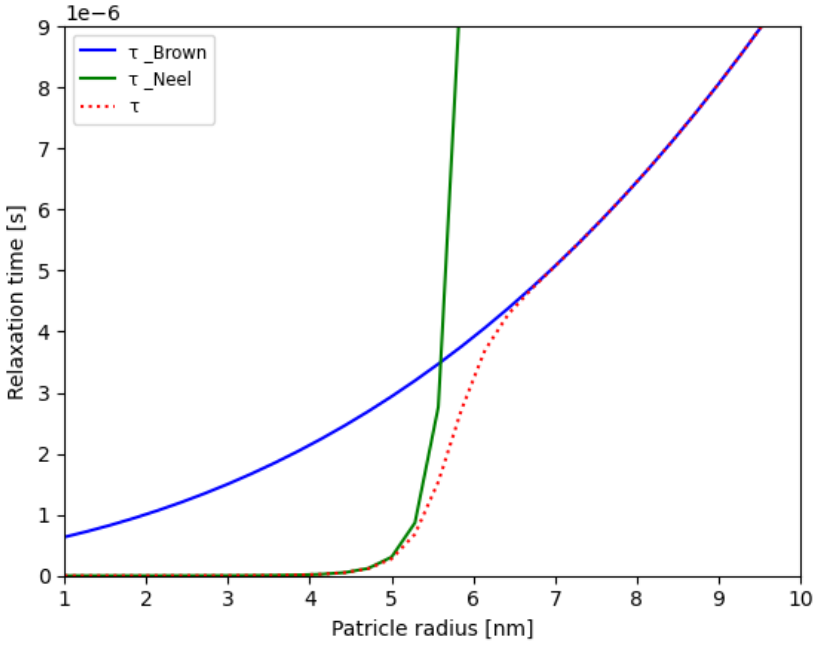

Figure 2.14: Plot of relaxation simulation including Neel, Brown relaxation and resulting effective relaxation times for magnetic nanoparticles in water

2.4.3. Hysteresis Losses

When subjected to an external magnetic field, the magnetic domains within the nanoparticles align with the direction of the field. Upon removal or reversal of the field, single domains do not instantly revert to their initial configuration. This delay in reaction forms a hysteresis loop on the magnetization graph, with the enclosed area indicating the amount of energy dissipated as heat during each magnetization and demagnetization cycle [36]. This specific mechanism is typical of magnetic nanoparticles in the single-domain range that exhibit a ferromagnetic behaviour and high values of coercivity.
The overall work produced by magnetic domain reorientations is converted into heat and expressed by the integral:

$$W_{\text{heat}} = \oint \mathbf{H} \cdot d\mathbf{M} \tag{2.20}$$

2.4.4. Viscous heating

Stirring effect or viscous heating is the third and last possible heating mechanism to be considered when dealing with nanoparticles. This affect is particularly hard to predict and model, and, as a consequence, to control. In literature, some attempts of evaluation of the drag coefficient between nanoparticles surfaces and fluids can be found. However, experimental evaluations are complex. Considering the turbulent flow mechanisms originated by immersion of large nanoparticles in a fluid, hydrodynamics approximations of the problem cannot be formulated [97].

2.5. Measurements of magnetic nanoparticles heating

The assessment of heating properties of magnetic nanoparticles, as introduced in section 2.1, has historically been performed to evaluate magnetic fluids for hyperthermia applications. However, inconsistencies in measurements, equipment, data analysis and testing conditions do not allow to easily perform comparisons among work performed by different researchers.
Another relevant aspect should be taken into consideration. The vast majority of commercially available setups used to measure heating capabilities of MNPs in a fluid (via application of an AMF) are inherently non-adiabatic setups, despite the presence of insulation materials. A fundamental distinction has to be made between ideally adiabatic, optimally insulated setups where no heat exchanges with the environment happen, and non-adiabatic setups.
When a non-adiabatic setup is used, the temperature vs. time plot produced by testing of MNPs shows three main regions: time-rise (linear region), Box-Lucas region (thermal exponential growth) and finally steady-state, when a stable maximum temperature is reached. The various regions can be seen below in Figure 2.15.

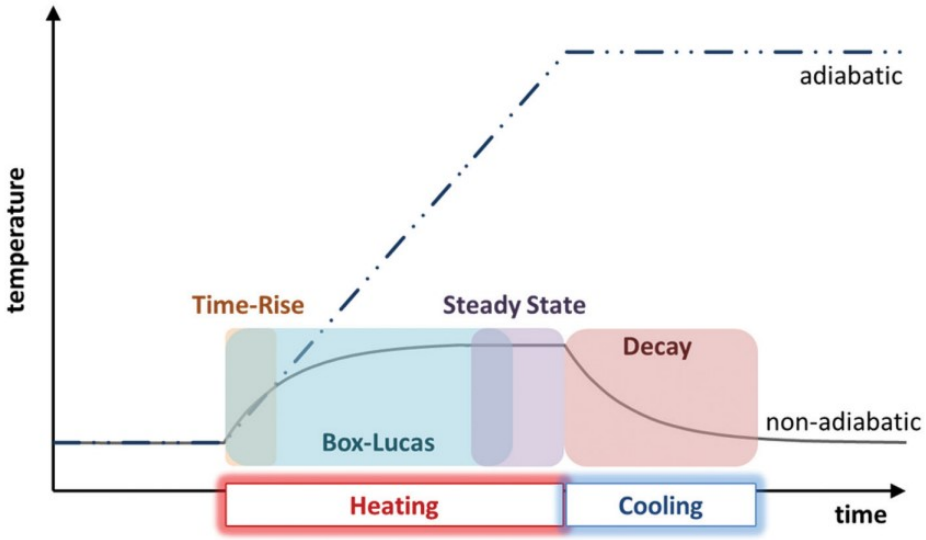

Figure 2.15: Scheme of idealized adiabatic and non-adiabatic heating conditions for MNPs, including the reference models used for fitting of each region. From [34]

Measure of induction magnetic heating capabilities can be obtained by finding the generated power per MNP mass unit [103]:

$$SLP = \frac{P}{m_{MNP}} \tag{2.21}$$

In the initial seconds of exposure to an AMF, the testing conditions can be considered adiabatic in the time-rise region. Therefore, the slope of the curve can be used to estimate the SLP, as it was done in this thesis:

$$SLP = C_p \cdot \frac{m_S}{m_{MNP}} \cdot \frac{\Delta T}{\Delta t} \tag{2.22}$$

Where C_p indicates the heat capacity of the sample, m_s the mass of the sample, m_{MNP} the mass of MNPs contained in the sample.

By fitting data points up to the the steady-state regime, the exponential Box-Lucas model can be used [81], where a and b are fitting parameters:

$$T = T_0 + a(1 - e^{-t/b}) \tag{2.23}$$

An additional method that can be applied is the corrected slope method, which takes into consideration any possible linear heat losses:

$$SLP = (C_p \frac{dT}{dt} + L\Delta T) \cdot \frac{m_S}{m_{MNP}} \tag{2.24}$$

Where ΔT identifies the difference at a certain instant between the sample and its baseline temperature, while L is the linear loss parameter.

Lastly, SLP can be calculated via steady state method. This model is calculated from the steady-state temperature (plateau) found from the curve:

$$SLP = T_{ss} L \cdot \frac{m_S}{m_{MNP}} \tag{2.25}$$

Where T_{ss} identifies the steady-state temperature, while L is the linear loss parameter.

2.6. Curie temperature

As mentioned in the introduction, interest in ferromagnetic nanoparticles rises from their potential ability to thermally autoregulate: reaching desired temperatures for processing, while being able to interrupt their heating at an appropriate temperature in order to ensure preservation of surrounding materials. Hence, the employment of materials' intrinsic characteristics such as their Curie temperature (or Curie point) is very promising when the goal is to fabricate self-controlling materials. This property entails a sharp transition from ferromagnetic to paramagnetic behaviour once the Curie temperature is reached (as can be seen from the saturation magnetization graph reported in Figure 2.16), ensuring no heat generation from hysteresis losses above this point.

The Curie point of bulk materials, as previously mentioned, is an intrinsic property. However, when fabricating magnetic nanoparticles this property can be engineered by tuning particles sizes, shapes and composition.

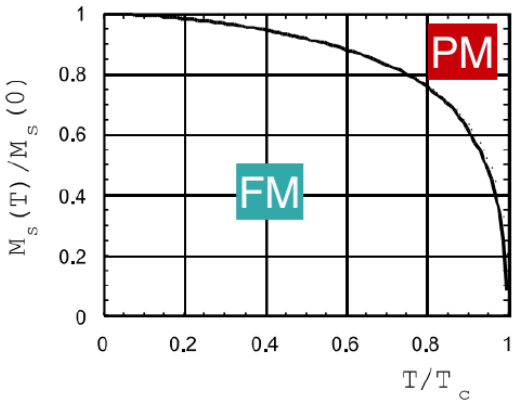

Figure 2.16: Saturation magnetization curve with respect to normalized temperature for pure Iron, FM and PM indicate the ferromagnetic and paramagnetic regions [17]

In this realm, a proper definition of the Curie point should be provided for better understanding of the next chapters.
According to the Handbook of Magnetism and Magnetic Materials [18], the Curie point can be defined as the critical temperature above which a material loses its ferromagnetism.
An externally applied magnetic field induces dipoles re-orientation within nanoparticles as long as they behave as a ferromagnetic material. In literature, Fabian et al. [27] identify the Curie temperature as an order-disorder phase transition (or second order transition) from a magnetically ordered low-temperature state to a thermally disordered high-temperature state. Other sources, such as Mugiraneza et el. [64] define the Curie point as a symmetry breaking point, where magnetic materials undergo a transition from magnetically ordered to a "magnetically disordered (gas-like) state", commonly known as paramagnetism. Once the Curie point is reached, thermal interactions become predominant, while ionic interactions among atoms become relatively weak [64]. Once the ferromagnetic Curie point is reached, spontaneous magnetization (M) within the material in zero applied field equals zero (Figure 2.16). This behaviour was described by Cochran and Heinrich [17].

Some examples of Curie points for materials commonly used in engineering applications are reported below in Table 2.5:

Table 2.5: Examples of Curie tmperatures for materials used in engineering [20]

Material	Curie temperature [°C]
Fe	770
Co	1127
Ni	356
Gd	19
Fe_2O_3	675
Fe_3O_4	585

The Curie point (T_C) was accurately measured for the first time in 1895 by Pierre Curie [5]. He was able to formulate the widely known Curie's Law, under the hypothesis of non-interacting magnetic moments and considering materials at high temperature and low magnetic fields [42]:

$$\chi = \frac{C}{T} \tag{2.26}$$

Here, χ is the material susceptibility, C is the Curie constant, specific for each material, and T is the temperature. This equation is widely known as it describes the behaviour of paramagnetic materials, highlighting the inverse proportionality occurring between susceptibility and temperature.

Curie's Law was later expanded by Pierre-Ernest Weiss to include his work on the molecular field theory [64]. Under the hypotheses of interacting magnetic spins and at higher temperatures, he included a factor θ to the initial model. Above Curie temperature, the Curie-Weiss law is used to define the susceptibility of ferromagnets in their paramagnetic region [76]:

$$\chi = \frac{C}{T - \theta} \tag{2.27}$$

In this equation a new term is introduced: θ is the magnetic ordering temperature (also named Weiss point or Weiss temperature in literature). This equation is particularly relevant as it reflects how thermal fluctuations become more significant with increasing temperature, while susceptibility rapidly decreases. The use of susceptibility measurements to evaluate

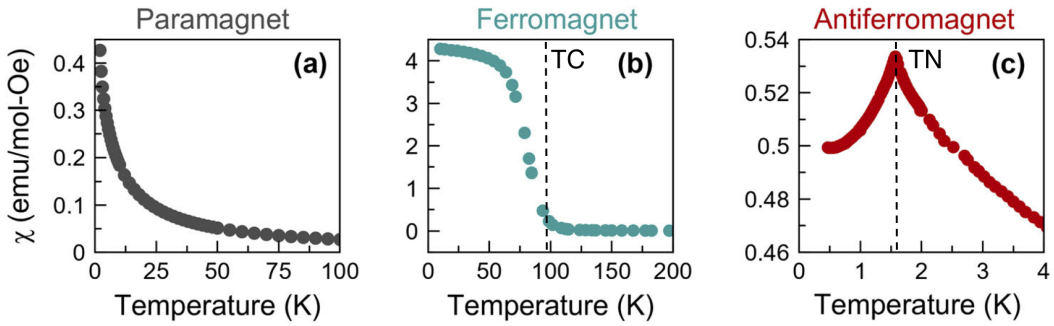

Figure 2.17: Experimental magnetic susceptibility measurements vs. temperature for: (a) Paramagnetic material ($SrMn_{0.5}Te_{1.5}O_6$), (b) Ferromagnetic material ($Ni_{0.68}Rh_{0.32}$), (c) Antiferromagnetic material ($Gd_2Pt_2O_7$) [64]

order-disorder phase transition (such as the Curie transition) is usually advantageous, as transitions are highlighted by marked discontinuities in the susceptibility vs. temperature curves, as can be seen from Figure 2.17.

Plots of the inverse susceptibility of materials, on the other hand, are useful when the goal is to underline the linear relation occurring between $1/\chi$ and T. Following the Curie-Weiss law, $1/\chi$ has a linear behaviour of slope C. However, its intercept (θ_{CW}) can be positive, null or negative, depending on the type of material taken into consideration (as can be seen in Figure 2.18). A positive θ_{CW} value indicates ferromagnetic interactions, negative values indicate antiferromagnetism, while values of θ_{CW} close to zero suggest negligible magnetic interactions, hence paramagnetism [64].

In contrast, diamagnetic materials do not show any dependence of their susceptibility on temperature. Typical materials known to be diamagnetic are calcite, quartz, and water [74].

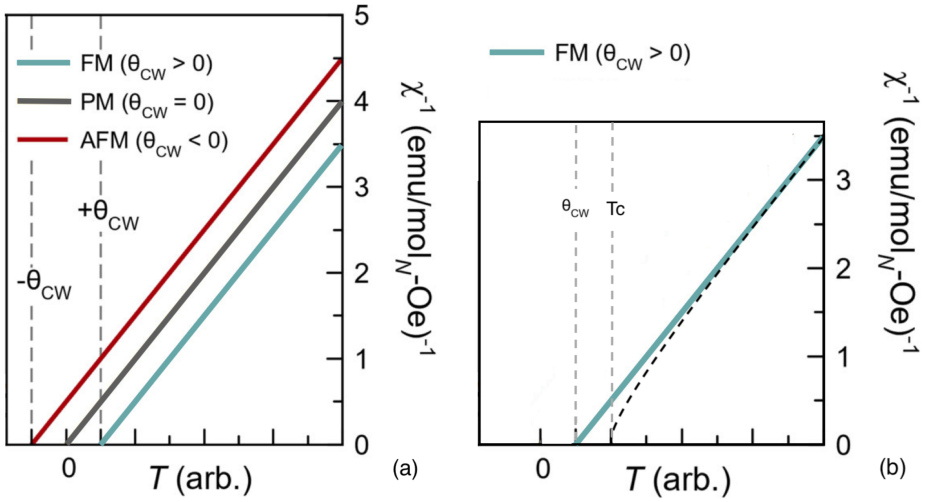

Figure 2.18: (a) Inverse susceptibility vs. temperature for materials following the Curie-Weiss law [64] (b) Inverse susceptibility (experimental and modelled via Curie-Weisss model) vs. temperature for ferromagnetic materials, highlighting both Weiss point (θ_{CW}) and Curie point (T_C) [64]

3

Research area and scope

To convey a better understanding of the research project, section 3.1 provides additional information regarding the motivation, background, and people involved in the study.

Moreover, in the following section 3.2, the reader is introduced to the research scope of this thesis. The specific focus of the study is stated by formulating the main research question. Finally, some additional sub-questions are reported, in order to guide the reader along the investigation of specific aspects of interest.

3.1. Research group and background

Genesis of this thesis can be found in the work performed within the ENLIGHTEN (Enabling Integrated Lightweight Structures In High Volumes) programme. This €6 million, seven-year project was launched by the University of Twente (The Netherlands) in 2021. The main purpose of the initiative is to promote the use of recyclable thermoplastic materials for the manufacturing of aerospace parts. TU Delft is involved in the technology development of Work Package 3, specifically with regard to ultrasonic and induction welding. The goal in this area is to develop efficient, lightweight solutions to be applied in the realm of thermoplastic fusion bonding, all taking into consideration their suitability for materials recycling.

Following this, Professor Laura Rossi and Professor Clemens Dransfeld took up the challenge of this project and funded a combined research group between the TU Delft faculties of Chemical and Aerospace Engineering. The background of Dr. Rossi in soft matter and synthesis of magnetic nanoparticles, combined with Prof. Dransfeld's experience in composites manufacturing, inspired the idea of developing MNPs suitable for the induction welding of thermoplastics. This objective was then explored by breaking down the main research ideas into sub-topics: design and characterization of nanoparticles, polymer embedding, and finally testing of their suitability for welding (as can be seen from the summary map of Figure 3.1, following page).

Preliminary tests on MNPs functionalized epoxy composites were performed by Gouri Nayanar during her 2021 master thesis project at the Chemical Engineering faculty. Maghemite, hematite, and neodymium were embedded in epoxy resin and the influence of magnetization and size of the nanoparticles was studied [68].

In 2022, master student Allan Barbosa completed his study titled "Superparamagnetic Fe3O4 Nanoparticle Based Susceptors For Induction Heating" [10]. In this work, magnetite (Fe_3O_4) nanoparticles were mixed with LM-PAEK powder, then compounded, and finally thermo-pressed to produce circular susceptors. The samples were tested by heating via an induction coil, and temperature was monitored via thermocouples. The heating behaviour was then simulated on ANSYS, showing good accordance with experimental values.

During her PhD, between July 2022 and July 2023, Giovanna Bruscia furtherly contributed to the research. The project, named "Magnetic particle susceptors for temperature-controlled induction welding of thermoplastics", focused on the study of magnetite nanoparticles as filler for an LM-PAEK polymeric matrix. The distribution of MNPs after compounding was tested via backscattering SEM/EDS and preliminary studies for induction heating were performed, as well.

Between 2023 and 2024 Agneta Meiksane, as a researcher at the Faculty of Aerospace Engineering, took up the project mentioned above. In her study named "Embedding magnetic particles into LM-PAEK polymer using micro-compounder" microcompounded LM-PAEK samples were prepared. Using the same extrusion parameters previously tested by Giovanna, Agneta produced samples with various weight particle concentrations of magnetite and maghemite. The material was then tested with induction heating equipment at the Fiber Institute of Bremen University. The process was monitored via thermal camera and values as high as 350° C.

Starting February 2024 Dnyandevi Dileep Deorukhkar studied manganese ferrite ($MnFe_2O_4$) in her master thesis research "Synthesis of magnetic nanoparticles for magnetic induction welding" [23]. In this study, nanoparticles were synthesized via a co-precipitation method by ion substitution, producing MNPs with composition ranging from $MnFe_2O_4$ to Fe_3O_4. This type of nanoparticles showed promising magnetic properties after characterization and a Curie temperature around 300° C, suitable for the fusion bonding of high-performance polymers. Specifically, this work gave a good explanation of the relation between ion distribution and composition to nanoparticles morphology and Curie temperature, proving that a tunable transition temperature can be achieved.

Finally, Andrey Kuznetsov joined the group in summer 2024 as a postdoctoral researcher. His previous experience in modelling the self-assembly phenomena of magnetic nanoparticles, magnetization and heat transfer provided great contribution to understanding heating phenomena of MNPs studied in this thesis.

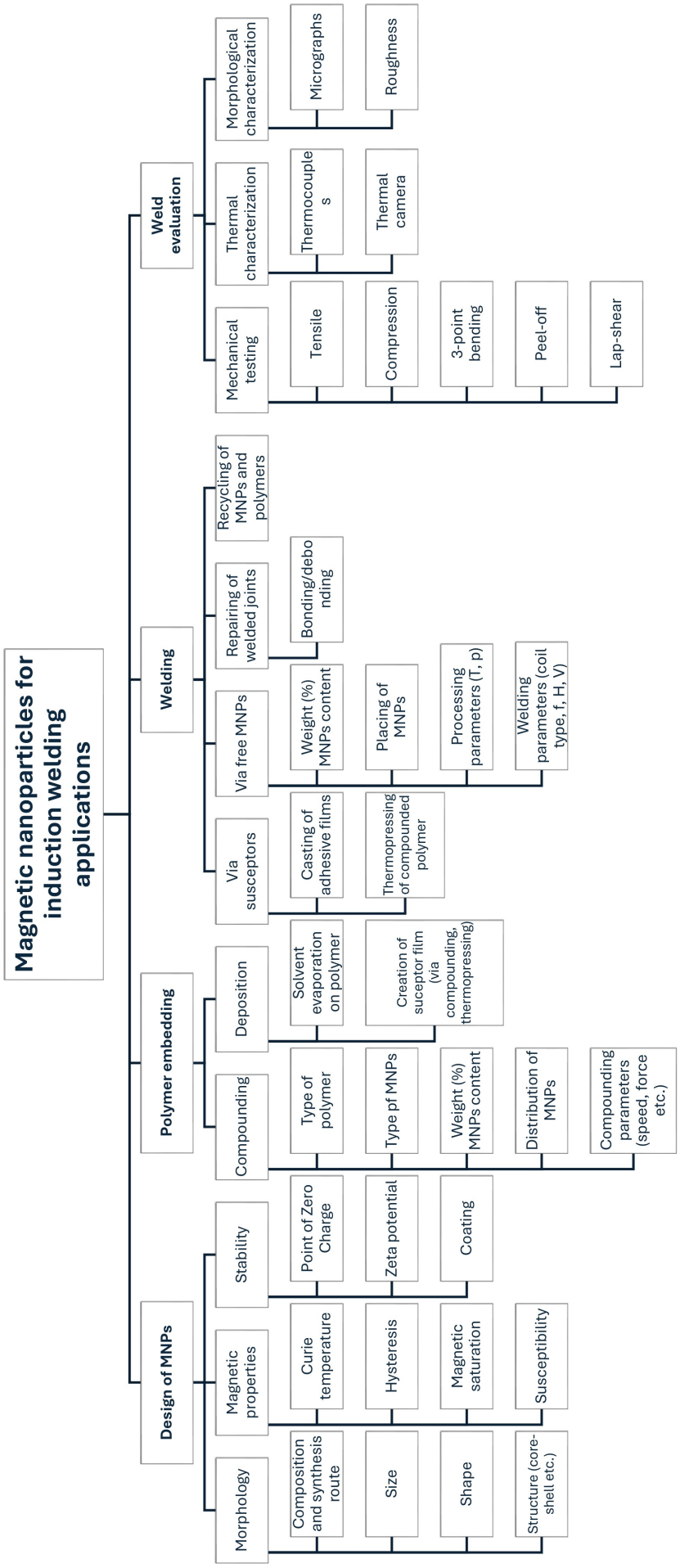

Figure 3.1: Map describing the considered research area

3.2. Research questions and objectives

As seen in the previous section, the foundations of this thesis can be found within the work of the research groups led by Professor Clemens Dransfeld and Professor Laura Rossi.

Motivation for this research can be expressed as the need to perform a preliminary selection of suitable nanoparticles and evaluate their thermal behaviour and suitability for future applications in polymer welding. In order to do this, it is particularly relevant to collect induction heating results, along morphological and magnetic data coming from particles characterization. Therefore, the primary goal is to establish the link between heating behaviour and magnetic nanoparticles features, which can be formulated into the following research question:

How are heating efficiency and temperature control of magnetic nanoparticles affected by their morphological and magnetic properties during induction heating?

Following the main question, some additional sub-questions have been formulated to further break down the central goal of the research:

- How do alternating magnetic field parameters (such as coil type, field intensity and frequency), affect the heating behaviour of magnetic nanoparticles?
- How does the concentration of magnetic nanoparticles affect their heating behaviour?
- How can the heating capabilities of different magnetic nanoparticles be efficiently measured and compared?
- How can the induction heating behaviour of specific magnetic nanoparticles be justified by available theoretical models, most importantly by Linear Response Theory (LRT)?
- What are the morphological characteristics of considered nanoparticles, in terms of shape, size and cristallinity?
- What are the magnetic characteristics of tested nanoparticles?
- What experimental procedure can consistently and accurately predict the Curie temperature of magnetic materials?

Undertsanding the physical and thermal behaviour of MNPs is an essential step in the development of novel induction heating procedures for thermoplastic parts. To do this, experimental investigation and characterization of chosen MNPs will help draw meaningful conclusions and find answers to the formulated questions, helping correlate their features with their heating capabilities (summary of the investigated aspects can be found in Figure 3.2).

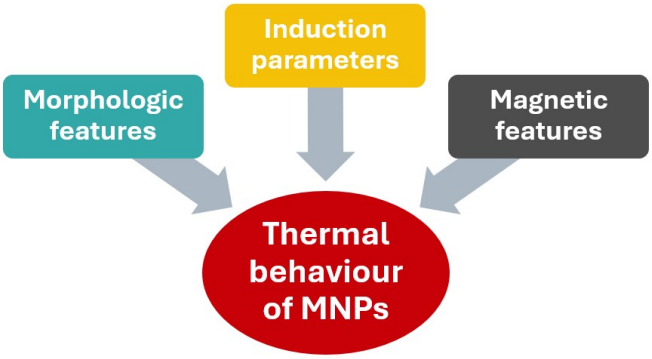

Figure 3.2: Graphic summary of factors influencing the heating behaviour of nanoparticles studied in this research

4

Materials

This chapter briefly describes the materials used to investigate the heating mechanisms of magnetic nanoparticles. This materials chapter is divided into two main sections: the first one describing properties and providing the reader with relevant information regarding the chosen samples, and a second one describing the preparation of MNPs suspensions for Magnetherm investigations.

The materials used in this study were chosen on the basis of availability from previous studies conducted by the research group and on the suitability of MNPs in terms of their magnetic properties, specifically their Curie temperature. The following magnetic nanoparticles were employed for this study:

- Magnetite
- Chromium Dioxide
- Nickel
- Nickel-Zinc Iron Oxide

4.1. Magnetite

Magnetite (and iron oxides in general) nanoparticles are a well-established material synthesized for ferrofluid and hyperthermia studies. The magnetite nanoparticles (Fe_3O_4) used in this thesis were purchased from U.S. Research Nanomaterials, Inc. in 2021, in the 8 and 20-30 nm size ranges. It is relevant to make the reader aware that proper conditions could not be ensured throughout the whole storage time. As magnetite is known to be less stable in oxygen environment than other iron oxides, such as hematite, partial oxidation (to maghemite) and change in properties are to be expected.

Table 4.1: Summary of properties of magnetite nanoparticles

Material property	Value
Specific gravity [g/mL]	5.18
Molecular weight [g/mol]	231.54
Melting point [°C]	1589-1599
Size [nm]	8 and 20-30

It is worth mentioning that magnetite nanoparticles were used in this thesis for the vast majority of tests performed via Magnetherm. This choice was taken because of the large amount of literature available regarding the study of ferrofluids produced with this material. However, tabulated Curie temperature of magnetite (585° C, [35]) is too high to be reached with Magnetherm induction heating.

4.2. Nickel nanopowder

A pure Nickel nanopowder (99.9 %) from Sigma-Aldrich (St. Louis, USA) was considered in this study, as well. Due to Nickel's strong ferromagnetic behaviour, its tabulated Curie temperature of 627 K (353.85° C, [35]) is well-established as calibration temperature for thermogravimetric analysis. This provided inspiration to apply TGA to the exploration of Curie transitions.

Table 4.2: Summary of properties of Nickel nanopowder

Material property	Value
Specific gravity [g/mL]	8.90
Molecular weight [g/mol]	58.69
Melting point [°C]	1453
Size [nm]	<100

4.3. Nickel-Zinc ferrite nanopowder

An additional nanopowder of Nickel-Zinc iron oxide ($NiZnFe_4O_4$) from Sigma-Aldrich (St. Louis, USA) was investigated. A tabulated 375°C Curie temperature [35], suitable for reaching processing temperatures of high-performance thermoplastics, suggested a possible future application of this material, and therefore interest in its investigation.

Table 4.3: Summary of properties of Nickel-Zinc ferrite nanopowder

Material property	Value
Specific gravity [g/mL]	2.81
Molecular weight [g/mol]	411.46
Size [nm]	<100

4.4. CrO2 nanopowder

Finally, a Chromium Dioxide nanopowder, sold under the commercial name Magtrieve, was acquired from Sigma-Aldrich (St. Louis, USA). This specific ferromagnetic material was used in the past for the production of magnetic tapes, disks, spin-polarized scanning tunneling microscopy [19], and as a by-product of Cr2O3 (green dye). This specific compound was chosen due to its availability and low tabulated Curie temperature of 286 K (112.85° C, [35]). This temperature falls within the operational limits of Magnetherm equipment and was particularly useful in observing the heating behaviour when the Curie transition is approached.

Table 4.4: Summary of properties of Chromium Dioxide nanopowder

Material property	Value
Specific gravity [g/mL]	4.85
Molecular weight [g/mol]	83.99
Melting point [°C]	>375
Size [nm]	<100

4.5. Preparation of MNPs suspensions for Magnetherm

This section describes the preparation of magnetic nanoparticles suspensions to be used for magnetic induction heating simulation. For this set of experiments, aimed at highlighting the importance of particle concentrations in magnetic fluids, magnetite nanoparticles in the 8 and 20-30 nm size ranges were combined with high temperature silicone oil from Sigma-Aldrich (St. Louis, USA).
Ten different batches of magnetite were dispersed in silicone oil, with concentrations varying from 5 to 100 mg/mL, following these steps: the needed mass of magnetite nanoparticles and silicone oil were weighed and combined, the mixture was then agitated with an IKA Vortex 3 for at least five minutes, finally, the fluid was placed in a sonicator for 30 minutes to dissolve any possible agglomeration of nanoparticles. Results were uniformly colored fluids with even distributions of magnetic nanoparticles as the one shown below in Figure 4.1.

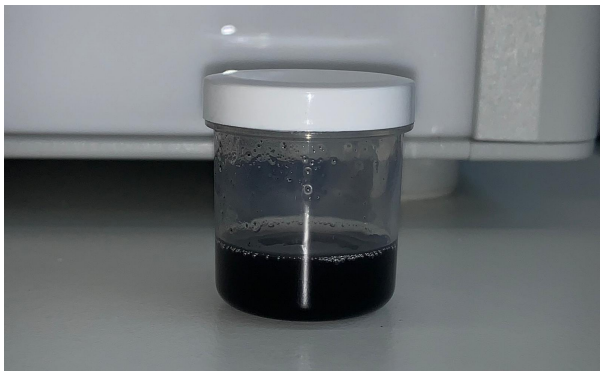

Figure 4.1: Example of the appearance of a suspension containing magnetic nanoparticles and silicone oil

Details regarding concentrations and physical properties of the suspension batches are reported below in Table 4.5 and Table 4.6.

Table 4.5: Summary of properties of Fe_3O_4 (8 nm) and silicone oil suspensions: concentrations, densities and heat capacities

		Real concentration				
Batch ID	**Nominal concentration (m/V) [mg/mL]**	**m/V [mg/mL]**	**m/m [%]**	**V/V [%]**	ρ **[g/mL]**	C_p **[J/(mLK)]**
A	5	5.14	0.49	0.10	1.07	1.79
B	10	10.06	0.95	0.19	1.09	1.80
C	15	15.16	1.42	0.29	1.11	1.81
D	20	20.11	1.88	0.39	1.13	1.82
E	50	50.03	4.55	0.96	1.24	1.88
F	100	99.99	8.70	1.90	1.41	1.96

Table 4.6: Summary of properties of Fe_3O_4 (20-30 nm) and silicone oil suspensions: concentrations, densities and heat capacities

		Real concentration				
Batch ID	**Nominal concentration (m/V) [mg/mL]**	**m/V [mg/mL]**	**m/m [%]**	**V/V [%]**	ρ **[g/mL]**	C_p **[J/(mLK)]**
G	5	5.30	0.50	0.10	1.07	1.79
H	10	10.04	0.95	0.19	1.09	1.80
I	15	14.94	1.40	0.29	1.11	1.81
J	20	20.08	1.88	0.39	1.13	1.82
K	50	49.95	4.54	0.96	1.24	1.88
L	100	100.35	8.72	1.90	1.41	1.96

The density of magnetic fluids was calculated with a rule of mixture, using the volumetric concentration (ϕ) of nanoparticles in the suspension, as follows [85]:

$$\rho = (1 - \phi) \cdot \rho_f + \phi \cdot \rho_{MNP} \tag{4.1}$$

Where ϕ indicates the volumetric concentration, ρ_f the density of silicone oil, and ρ_{MNP} the density of magnetite nanoparticles.

The total heat capacity of the fluid was then obtained in a similar fashion as the volume average of heat capacities from magnetic nanoparticles and silicone oil [85]:

$$C_p = \frac{(1 - \phi) \cdot \rho_f \cdot C_{p,f} + \phi \cdot \rho_{MNP} \cdot C_{p,MNP}}{\rho} \tag{4.2}$$

Where $C_{p,f}$ indicates the volumetric heat capacity of the fluid (silicone oil, in this case) and $C_{p,MNP}$ the volumetric heat capacity of magnetite MNPs.

The following values were assumed for the calculations:

	Magnetite MNPs	**Silicone oil**
Density [g/cm^3]	5.17	1.05
Heat capacity [J/(gK)]	0.73	1.7

5

Experimental procedures

The unique features of magnetic nanoparticles, such as their size, morphology, structure, and stability, can be tuned to influence magnetic anisotropy and ultimately achieve desired magnetic properties. This can be done through synthesis, heat treatments and/or surface modifications of MNPs.
However, achieving an in-depth comprehension of their characteristics is crucial to fully leverage these properties and validate the behaviour and suitability of nanoparticles for various uses. Therefore, a critical step in magnetic nanoparticle research for induction welding is the employment of characterization techniques to achieve this goal.

The following section explores the most relevant techniques used for this research: Differential Scanning Calorimetry (DSC), Fourier Transform Infrared (FTIR) spectroscopy, MagneTherm, Scanning Electron Microscopy (SEM) and Transmission Electron Microscopy (TEM), Thermo-Gravimetric Analysis (TGA), Superconducting Quantum Interference Device (SQUID), X-ray Diffractometry (XRD). These methods are summarized below in Figure 5.1.

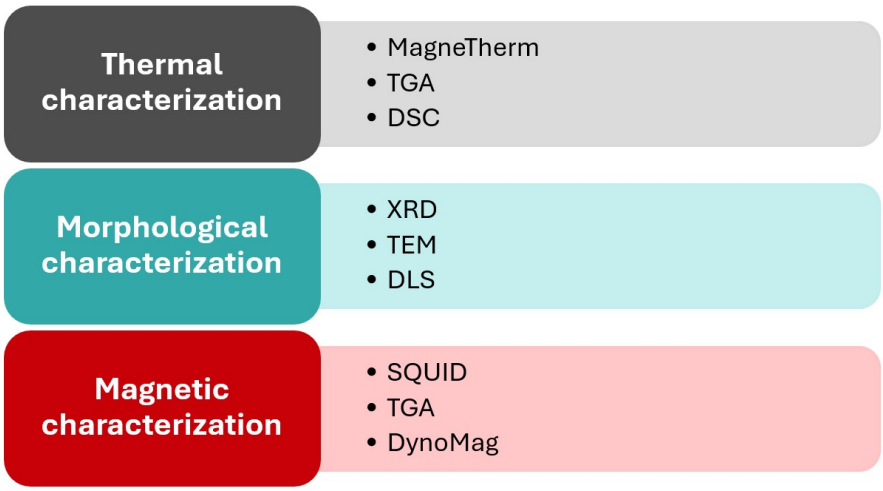

Figure 5.1: Summary of characterization techniques used in this research, grouped in thermal, morphological and magnetic characterization techniques

5.1. Induction heating simulation (MagneTherm)

Figure 5.2: MagneTherm equipment from nanoTherics

MagneTherm was used to perform induction heating experiments on nanoparticles. This specific type of equipment assembled by nanoTherics (Warrington, UK) is employed to simulate induction heating conditions and evaluate the thermal response of magnetic colloids. A TG2000 function generator (50-1000 kHz) is employed to control a power supply unit, generating a magnetic field (up to 50 mT) through a coil. The induction setup can be seen in Figure 5.2, while a block diagram of its parts can be seen below in Figure 5.3. The software provided with the system allows to control not only the applied field strength and frequency, but also the number of exposure cycles and the length of exposures (identified as "coil on").

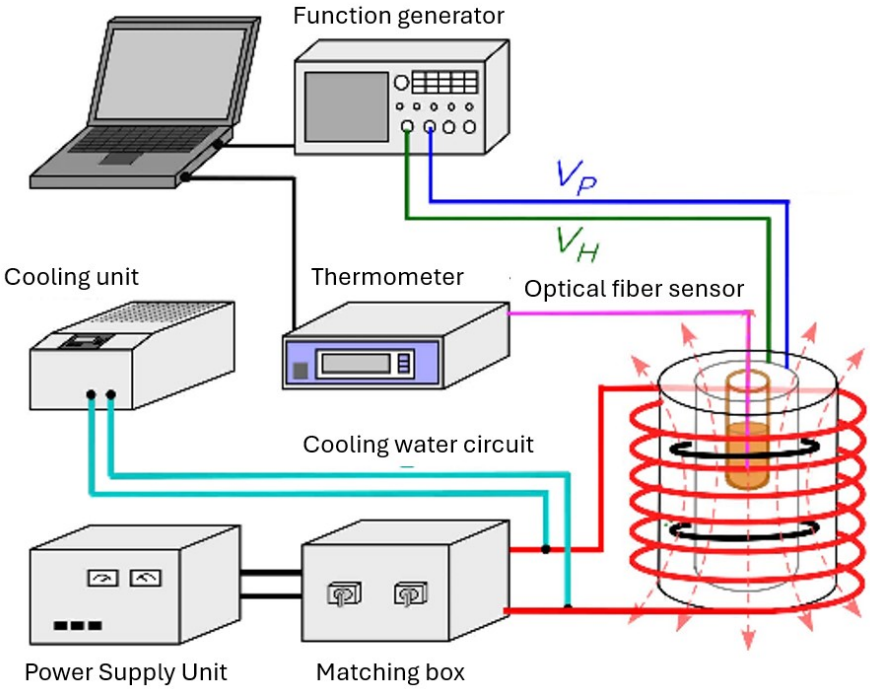

Figure 5.3: Diagram of MagneTherm equipment: experimental setup for induction heating tests. Adapted from [94]

The magnetic fluid is placed in a glass vial (Avantor VWR 1.5 mL screw neck vial) and kept at the centre of the coil during the test by the system, as shown in Figure 5.4. Insulation

is provided to the sample by external layers of polystyrene and polymethyl methacrylate (PMMA).

(a) Placing of the insulation tube within the MagneTherm

(b) Vial holder and insulation tube

Figure 5.4: Insulation system and placing of sample vial within MagneTherm system

The frequency is set by selecting the system capacitor and by tuning the system to the optimal discrete frequency value, which is the resonant frequency of the coil in use. In this specific research, five capacitors and two type of coils (high field and 9 turns) were used. A complete breakdown of the capacitor types, corresponding discrete frequencies and possible field ranges for the two coil types can be found below in Table 5.1 and Table 5.2.

Table 5.1: MagneTherm system capabilities for high field coil setup

High field coil		
Capacitor [nF]	**Frequency [kHz]**	**Field range [mT]**
6.2	992	0-16
15	624.4	0-22
30	441.5	0-30
88	258.5	0-40
200	172.3	0-50

Table 5.2: MagneTherm system capabilities for 9 turn coil setup

9 turn coil		
Capacitor [nF]	**Frequency [kHz]**	**Field range [mT]**
6.2	978.5	0-12
15	616.3	0-12
30	436	0-22
88	255.4	0-25
200	170.3	0-26

Temperature measurements in this study were conducted in two possible ways: by immersion with a fibre optic temperature probe PRB-G40 by OSENSA Innovations (Burnaby, BC, Canada) and externally using a FLIR A655sc from Teledyne FLIR LLC (Wilsonville, Oregon, USA), specifically in the case of experiments regarding MNPs concentrations reported in section 6.4.

It is relevant to highlight that due to temperature limitations of the fibre optic probe and not to damage the tube insulation system, heat generation during tests was closely monitored to maintain the vials below a 130° C temperature limit.

While the alternating magnetic field is applied to the colloid suspension, an optical fibre thermometer (or the thermal camera) measures the temperature change as a function of time due to MNPs heating [71]. At the same time, the cooling unit circulates water at 15° C to avoid excessive heat generation from the coil when turned on.

Calculation of heating efficiency parameters

After obtaining the temperature-time graphs showing heat evolution of a specific sample, some additional parameters are calculated.
The heating efficiency of a set of magnetic nanoparticles in a fluid can then be calculated through the following equation expressing the Specific Loss Power (SLP) [34]:

$$SLP = C_p \cdot \frac{m_S}{m_{MNP}} \cdot \frac{\Delta T}{\Delta t} \tag{5.1}$$

where C_p is the specific heat of the samples, m_S is the mass of the sample, m_{MNP} the mass of nanoparticles, and $\frac{\Delta T}{\Delta t}$ the initial heating rate. This parameter takes into account the initial linear heating of the sample, when heat losses are not yet prevalent and a simple linear fitting of the temperature vs. time curve can reflect the behaviour of magnetic nanoparticles.

The SLP value can then be converted into its volumetric expression [34], named Volumetric Specific Absorption Rate (SAR_V), which shows the power generation normalized by volume (in W/mL):

$$SAR_V = SLP \cdot c_{MNP} \tag{5.2}$$

Where SLP is the Specific Loss Power mentioned above (in W/g) and c_{MNP} is the volumetric concentration of MNPs in the fluid (g/mL).

An additional parameter has been developed to evaluate the magnetic heating efficiency of ferrofluids in low field and frequency conditions. The Intrinsic Loss Power (ILP) allows to express power generation while excluding extrinsic values of frequency and strength of the AMF, and is calculated as follows [103]:

$$ILP = \frac{SLP}{fH^2} \tag{5.3}$$

Where SLP is the Specific Loss Power mentioned above (in W/kg), f the frequency used for testing (kHz) and H the used field strength (kA/m). The Intrinsic Loss Power is expressed in $\frac{nHm^2}{kg}$.

5.2. Characterization techniques

5.2.1. FTIR

Fourier Transform Infrared or FTIR, is a chemical characterization techniques used to identify chemical bonds within the tested compounds. FTIR equipment has the capability to identify and confirm the presence of specific functional groups, coatings, and chemical bonds on nanoparticles' surfaces [37]. This technique is particularly useful for assessing the efficiency of surface functionalization processes and for detecting any changes in the nanoparticle composition during synthesis or post-synthesis treatments.
The working principle of FTIR consists in the identification of vibration modes of molecular bonds. A source produces an infrared wavelength signal, which passes through an interferometer and then generates an interference pattern. This modulated beam passes through the sample, where specific wavelength are absorbed. Finally a detector captures the IR beam and the computer converts the interferogram into a spectrum through a Fourier transform. The output is a wavelength absorption spectrum, acting as a "fingerprint" of the analyzed compound. More specifically, the resulting spectrum shows specific infrared absorption peaks corresponding to bond vibrations [60]. The overall composition of the sample is evaluated by comparing the obtained spectrum to a known library [37].

5.2.2. Microscopy: TEM

Morphological features of particles, such as shape, surface morphology, size, distribution, aggregation, and (eventual) core-shell structures, have been shown to be fundamental aspects influencing their properties and applications. Due to this reason, high quality images are necessary media to inspect the results of MNPs synthesis processes. Therefore, Transmission Electron Microscopy (TEM) constitutes a particularly relevant step for the characterization process of magnetic nanoparticles. TEM is employed for observation of small nanoparticles, in the size range below 50 nm, whereas SEM can be used when larger entities are expected [25].
Samples for transmission electron microscopy were prepared by dispersion of MNPs in isopropanol, sonication for 10 minutes to dissolve any aggregate, and then by deposition and drying of one drop on a carbon coated grid.
Images were acquired with a JEOL 1400 plus Electron Microscope (Akishima, Tokyo, Japan) and then analyzed via ImageJ (Java) visual software. The measurement scale was set and the particles were measured manually. The data was then converted to a frequency histogram and fitted with the following log-normal modified size distribution function to obtain the median and standard deviation of particle dimensions:

$$f(r) = \frac{1}{r\sigma\sqrt{2\pi}} exp\left[-\frac{(lnr - ln\theta)^2}{2\sigma^2}\right] \tag{5.4}$$

$$\int_0^\infty f(r)\, dr = 1 \tag{5.5}$$

Where r indicates the radius (size) of particles, $ln(\theta)$ the median and σ the standard deviation of $ln(r)$.

5.2.3. TGA

Thermo-Gravimetric Analysis, commonly known as TGA, is a well-known technique used to monitor the mass loss of samples when exposed to specific heating cycles. The test is typically performed to monitor thermal degradation (also known as charring or combustion), phase transitions, absorption or desorption of chemicals and/or oxidation phenomena happening within the studied sample [92]. Moreover, this technique is particularly relevant and frequently used in the field of material characterization to obtain information regarding thermal degradation of polymers.
During the test, the sample is placed in a ceramic pan and placed in a heating furnace which incorporates a high precision balance. Throughout the heating cycle, a purge gas is used to control chamber conditions and the sample mass is accurately monitored by the balance and plotted against time or temperature [92].

In this project, TGA 8000 equipment from PerkinElmer (Waltham, Massachusetts, USA) was used to carry out measurements. A picture of the used equipment and a breakdown of all parts are reported below in Figure 5.5.

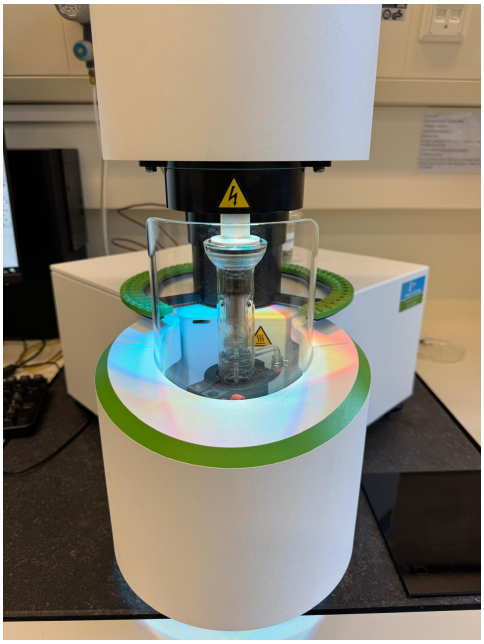

(a) PerkinElmer TGA 8000

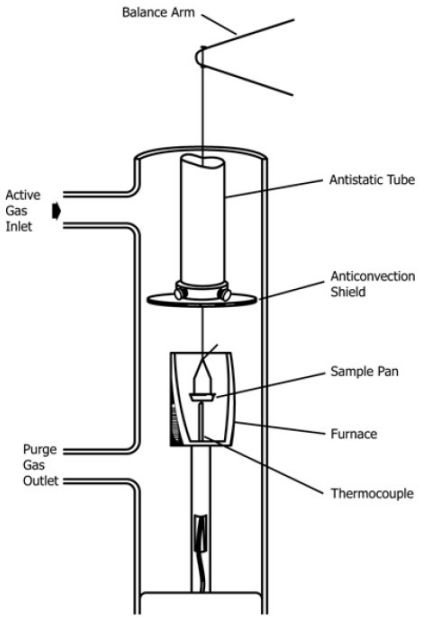

(b) Diagram of verticsl TGA system, including part names

Figure 5.5: Picture and diagram of TGA 8000 used in this thesis

Procedure to establish Curie temperature via Thermogravimetric Analysis

Within the scope of this thesis, thermogravimetric analysis was used to identify the Curie temperature of tested samples, a fundamental property of magnetic nanoparticles. In contrast to the mentioned more widely diffused uses of TGA (thermal degradation, phase transitions, absorption or desorption of chemicals and/or oxidation), a procedure normally applied to perform calibration of TGA was applied instead.
Melting and magnetic transitions of materials are currently recognized as the most reliable calibrating techniques for TGA. ASTM E158221 (Standard Test Method for Temperature Calibration of Thermogravimetric Analyzers) describes the aforementioned calibration practices. An example of TGA calibration curve for a Nickel rod is shown in Figure 5.6.

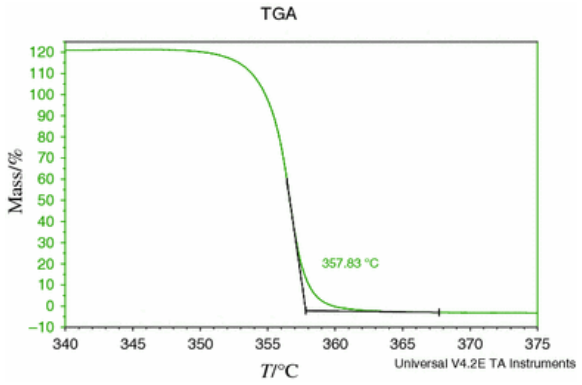

Figure 5.6: Curie temperature of Nickel calculated via TGA measurement. From [49]

In this section, a precise description of the procedure used to perform Curie temperature measurements via TGA is given. The needed steps are reported below:

1. Proceed to weigh the empty sample pan and tare TGA
2. Load the sample material
3. Place the magnet underneath the furnace
4. Perform measurement of the initial sample weight (theoretical 100%) under applied magnetic field
5. Initiate data recording for TGA measurement
6. Hold at an initial temperature (30° C) for at least 5 minutes in order to minimize
7. Heat the sample at the needed heating rate until a visible magnetic transition weight drop is observable
8. Hold at a final temperature for at least 5 minutes
9. Interrupt data acquisition
10. Generate the derivative plot (DTGA) for the measurement and identify the maximum peak
11. Via Origin or TGA software, identify the magnetic transition temperature by manually generating the curve offset, starting from the DTGA peak (as shown in Figure 5.7)
12. Repeat and perform the Curie temperature measurement multiple times for statistical accuracy

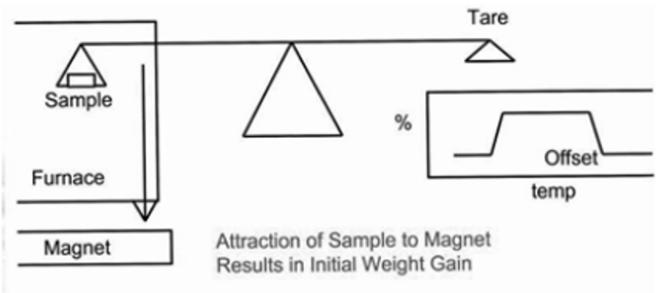

Figure 5.7: Vertical setup of TGA for Curie temperature evaluation and corresponding mass vs. temperature curve. From [75]

5.2.4. SQUID

A Superconducting Quantum Interference Device (SQUID) is an extremely sensitive magnetometer used to measure minute magnetic fields. It operates based on the principles of superconductivity and quantum interference, relying on a superconducting loop that contains one or more Josephson junctions—weak links made of thin insulating or normal-conducting layers sandwiched between superconductors. These junctions play a critical role in enabling the device to detect variations in magnetic flux. The underlying principle of SQUIDs is flux quantization, which states that the magnetic flux enclosed by a superconducting loop can only exist in discrete integer multiples of the magnetic flux quantum. When an external magnetic field is applied, the total flux inside the superconducting loop changes, causing variations in the quantum state of the system. This, in turn, affects the phase difference across the Josephson junctions, altering the supercurrent flowing through the device. By leveraging this quantum mechanical effect, a SQUID produces an oscillating voltage response that depends on the applied magnetic field. These oscillations create a periodic signal, which can be detected and analyzed with extreme precision, allowing scientists to measure even the smallest changes in magnetic flux. The result is an incredibly sensitive tool that can detect magnetic fields far weaker than those generated by the human brain or subtle geological variations in Earth's crust. The SQUID equipment is capable of providing information on the susceptibility (χ) and magnetization (M) of materials when exposed to an external field (H), in addition to the saturation magnetization (M_S), coercivity (H_C) and remanence (M_R) [105]. The equipment used for this project is a Quantum Design (CA, USA) MPMS XL SQUID Magnetometer.

5.2.5. XRD

In x-ray diffractometry, electromagnetic radiation is applied to the sample of interest to evaluate its crystalline properties. D8 ADVANCE x-ray powder diffractometry equipment from Bruker (Billerica, U.S.A.), using a Cu $K\alpha$ radiation source at 40 kV and 25 mA, was used to perform measurements reported in this thesis.

Functioning mechanism of XRD equipment can be described as follows: a dry sample is prepared and placed on the sample stand, then the x-ray once the x-rays hit the sample, they are scattered by the atoms in the crystal lattice and captured by a moving detector. For certain angles (2θ), the scattered X-rays creates constructive interference according to Bragg's Law [31]:

$$n\lambda = 2dsin\theta \tag{5.6}$$

where n is an integer, λ is the wavelength, d is the spacing between crystal planes, and θ is the angle of incidence.

Then, the crystallite size can be calculated using Scherrer equation [24]:

$$D = \frac{K\lambda}{Bcos\theta} \tag{5.7}$$

where K is a dimensionless factor (typically $K = 0.9$ [44]), D is the crystalline size (nm), λ is the wavelength of the X-ray source, B is the width at half height of the peak accounting for instrumental broadening, and θ is the wavelength of the peak.

Finally, the lattice constant a can be evaluated by using the wavelength and Miller indices (h, k, l) provided by the XRD equipment [31]:

$$a = \frac{\lambda \left(h^2 + k^2 + l^2\right)^{1/2}}{2\sin\theta} \tag{5.8}$$

Overall, this analysis provides details about the crystal structure and orientation, lattice spacing, strain, and core particle size [83].

6

MagneTherm measurements

This chapter report the outcomes of induction heating experiments performed with MagneTherm equipment.
In the first section, section 6.1, results obtained from heating tests performed on dry nanopowders are shown and discussed, followed by section 6.2 and section 6.3 where heat generation is correlated to parameters of the externally applied alternating magnetic field. Finally, in section 6.4, data regarding MagneTherm experiments performed on samples of magnetite suspensions at different particles concentration are shown and analyzed.

6.1. Heating mechanisms of dry nanopowders

In this first section, test data resulting from tests conducted on dry nanoparticles are reported. All the materials listed in chapter 4 were tested. Induction heating simulations were performed on 50 mg samples placed in glass vials and exposed to alternating magnetic fields of frequency 992 kHz, with a strength of 6.37, 9.55 and 12.73 kA/m. For this set of experiments the high-field coil setup was used.
Test conditions were monitored to be kept as close as possible between the tests, and sufficient time was given to each sample to reach thermal equilibrium before exposure. Each measurement ("coil on") was run for 30 minutes, after an initial 10 seconds recording before exposure. Tests were interrupted once the limit temperature of 130° C was reached.

The data output of conducted tests were manipulated and results are reported in the following pages.
Heat generation graphs of temperature plotted against time evolution are depicted, for each nanopowder material, in Figure 6.1.
The same data points were then reorganized to highlight the effect of field strength and directly compare the different materials, resulting in the plots shown in the following page in Figure 6.2.

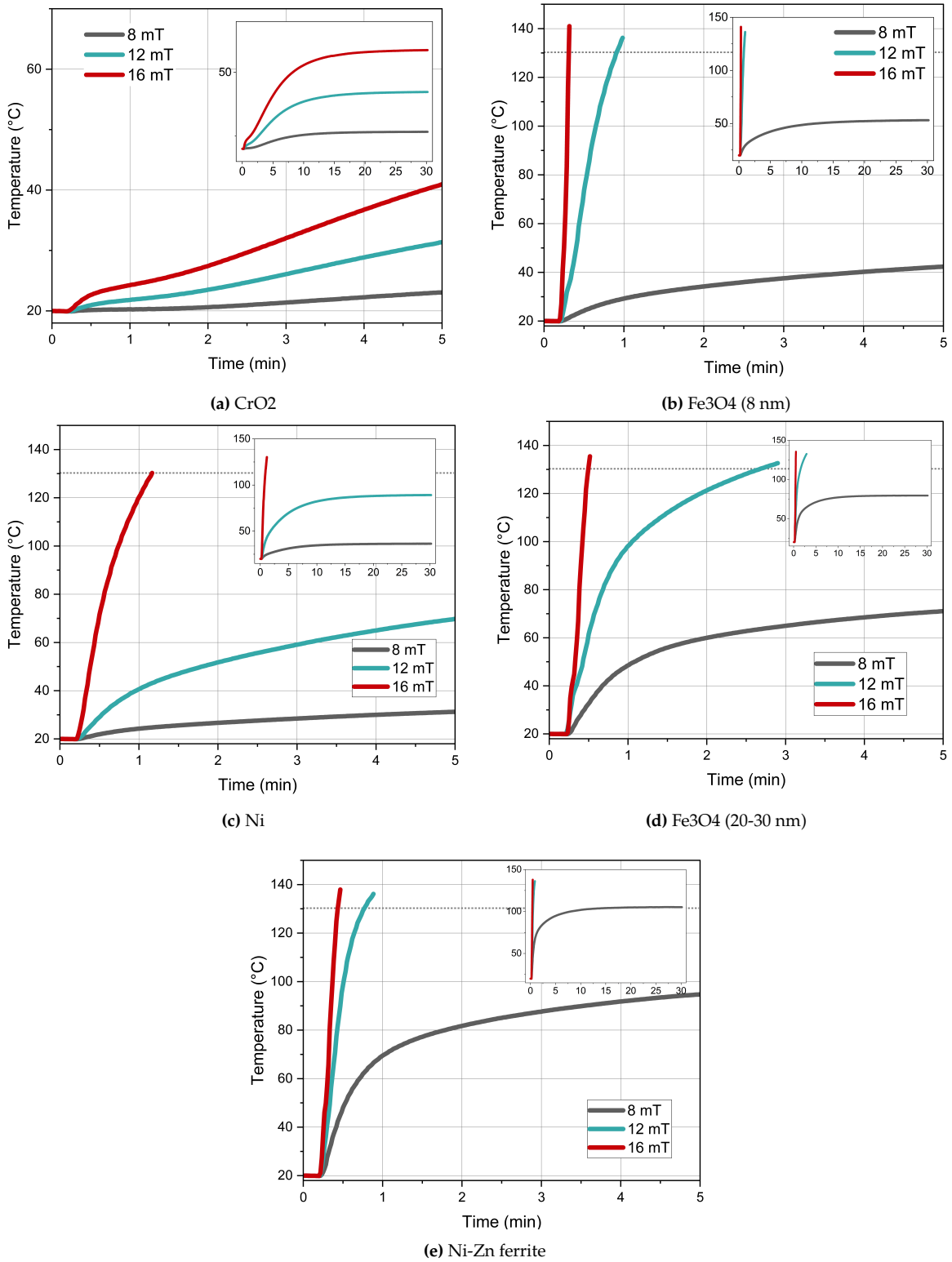

(a) CrO2

(b) Fe3O4 (8 nm)

(c) Ni

(d) Fe3O4 (20-30 nm)

(e) Ni-Zn ferrite

Figure 6.1: Temperature vs. time plots of MagneTherm tests performed on 50 mg of various nanoparticles types, 8-16 mT, 992 kHz. The graphs show a 10 seconds recording before exposure to AMF, followed by a 5 minute exposure. The inserts show the full 30 minutes runs.

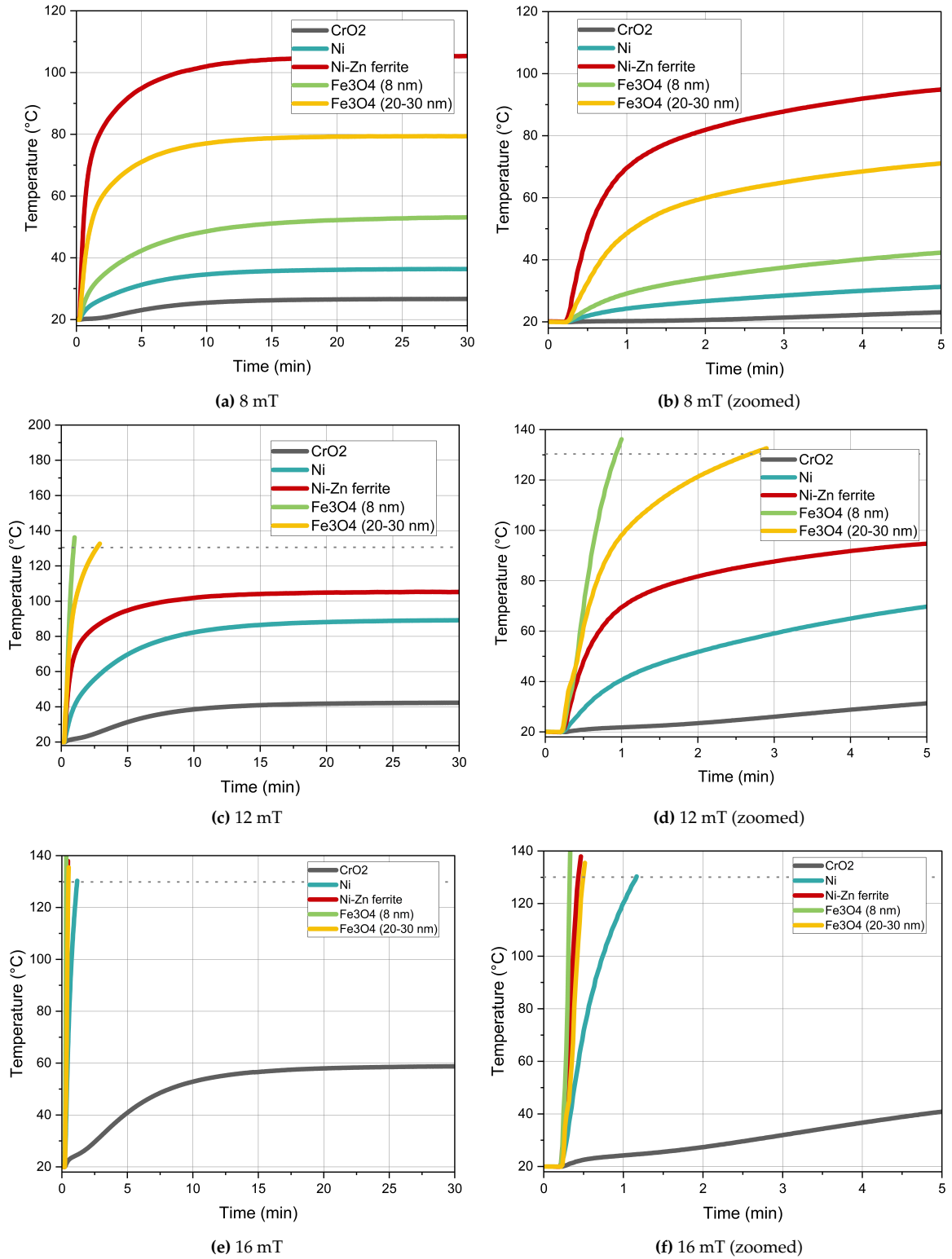

(a) 8 mT

(b) 8 mT (zoomed)

(c) 12 mT

(d) 12 mT (zoomed)

(e) 16 mT

(f) 16 mT (zoomed)

Figure 6.2: Temperature vs. time plots of MagneTherm tests performed on 50 mg of various nanoparticles types, 8-16 mT, 992 kHz. The graphs show a 10 seconds recording before exposure to AMF, followed by a 30 minute exposure.

6.1.1. Discussion

Some trends can be highlighted from graphs reported in Figure 6.2. In all tests, Chromium Dioxide showed the lowest heating efficiency. Ni-Zn ferrite showed the highest heat generation at 8 mT, but magnetite in both size ranges showed a predominant heat generation at 12 and 16 mT. It is interesting to observe that magnetite nanoparticles reached the 130°C limiting temperature at 12 mT, indicating a very strong magnetization. They were followed by Nickel nanopowder, which were able to reach the same heat generation only when a 16 mT field was applied.
Chromium Dioxide, on the other hand, showed limited heat generation capabilities and did not reach its theorized Curie temperature of 112.85 °C [35], even at the highest applied field. Moreover, a peculiarity can be observed in all CrO2 induction heating tests from Figure 6.1: all the curves show a bimodal trend in the initial part of the heating. This behaviour has not been previously documented in literature and requires further investigation.

The power generation in this set of tests is to be fully attributed to the Neel relaxation heat dissipation mechanism, due to the absence of a fluid to allow for Brownian motion. In the case of magnetite nanoparticles, experiments were interrupted when a temperature of 130° C was reached, in order to preserve optimal conditions of the equipment.

It is also relevant to inform the reader about a critical aspect of this set of measurements. The tested particles were chosen because of their availability in the nano-size range, however, strong differences in size and morphology At this stage, no specific information regarding size distribution and/or morphology of the particles is known. A large polidispersity of nanoparticles is to be expected, specifically when catalyst nanopowders are employed (as in the case of Ni, $NiZn$ ferrite and CrO_2), when the only information regarding size provided by the manufacturer is the indication of being below 100 nm range.

As was proven in a similar study [43], these specific testing conditions can be regarded as testing a compact sample, where the particles interact with each other. Due to the proximity of MNPs in a dry sample, strong dipole-dipole interactions among particles are present. This behaviour is even more relevant for larger particles and it might limit the freedom of spin re-orientation. As a consequence, this might explain the lower heat produced by larger magnetite nanoparticles.

As can be observed in Figure 6.2, all samples show an initial linear regime, when heat losses constitute a minor phenomenon. The power dissipation of magnetic nanoparticles in the absence of heat losses can be calculated as:

$$P = C_p \cdot \frac{\Delta T}{\Delta t} \tag{6.1}$$

Therefore, a sample in perfectly adiabatic conditions will produce a temperature rise of:

$$\Delta T = \frac{P \cdot \Delta t}{C_p} \tag{6.2}$$

However, when heat losses become more significant, an exponential dependence of temperature on time (Box-Lucas model) is established until the maximum, steady-state temperature is reached:

$$T = T_0 + a(1 - e^{-t/b}) \tag{6.3}$$

It can also be observed from Figure 6.2 that the steady-state was reached for all samples even for the weakest applied magnetic field of 8 mT, in ~ 20 minutes. This temperature can be

identified as the temperature for which the internal magnetic power generation equals the heat dissipation of the system via air convection and irradiation.
Moreover, when the alternating magnetic field has sufficiently high strength and frequency, the ultimately reached temperature plateau is theorized to correspond to the Curie temperature. However, this could not be directly observed due to temperature limitations of MagneTherm equipment.

6.2. Influence of frequency

In this section the effects of frequency applied via magnetic induction equipment are reported. For this specific set of tests, magnetite in the 20-30 nm range dispersed in silicone oil was used. Five 1 mL sample extracted from batch K (Table 4.6), with ideal concentration of 50 mg/mL, were employed for testing with Magnetherm equipment. All the samples were exposed to an alternating magnetic field of 9.55 kA/m strength and a frequency of 170.3, 255.3, 435.8, 616.2 and 978.4 kHz.
The temperature vs. time profiles resulting from these experiments are reported below in Figure 6.3. Graphs showing the temperature rise and the maximum temperature reached during simulations against frequency are depicted in Figure 6.4.

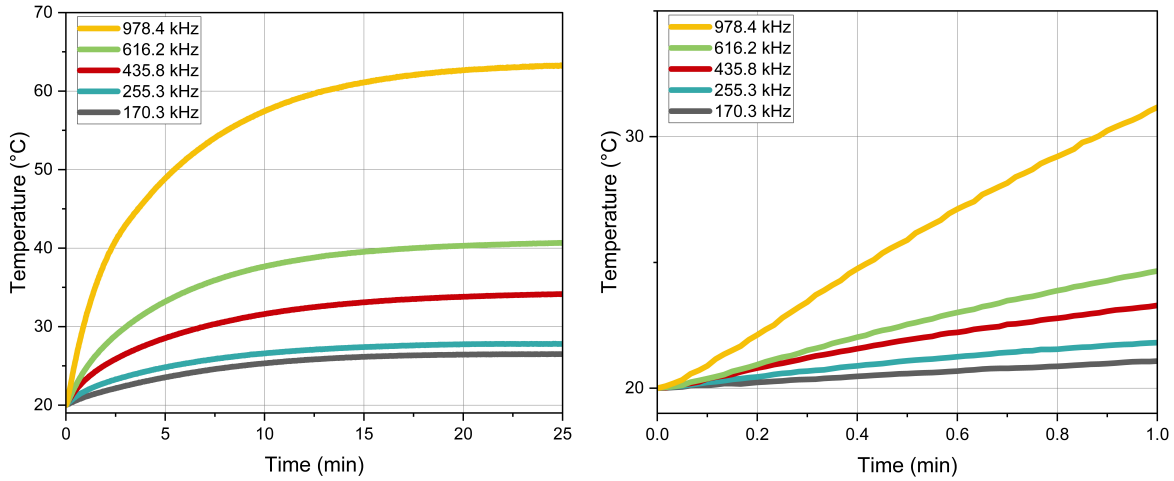

(a) Full temperature profile (0-25 min.)

(b) Temperature profile, zoomed (0-1 min.)

Figure 6.3: Temperature vs. time evolution plots for magnetite concentration of 50 mg/mL, field 9.55 kA/m, frequency 170.3-978.4 kHz

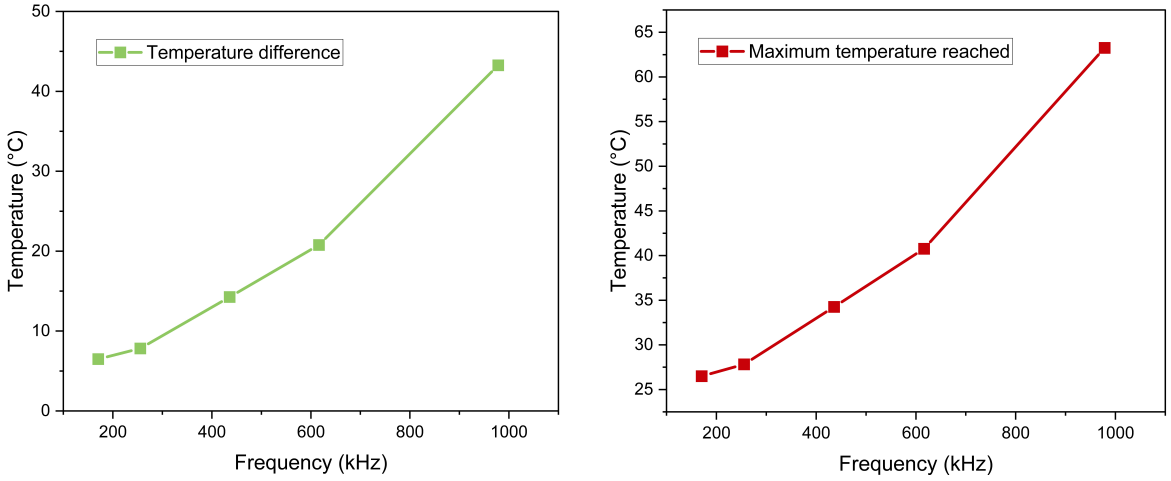

(a) Temperature rise vs. frequency

(b) Max reached temperature vs. frequency

Figure 6.4: Plots of temperature generation vs. frequency for magnetite concentration of 50 mg/mL, field 9.55 kA/m, frequency 170.3-978.4 kHz

Data have been furtherly manipulated to obtain magnetic heating parameters: Specific Loss Power, volumetric Specific Absorption Rate and Intrinsic Loss Power.
Plots of SLP and ILP values correlated to the applied field frequency can be seen below in

Figure 6.5.

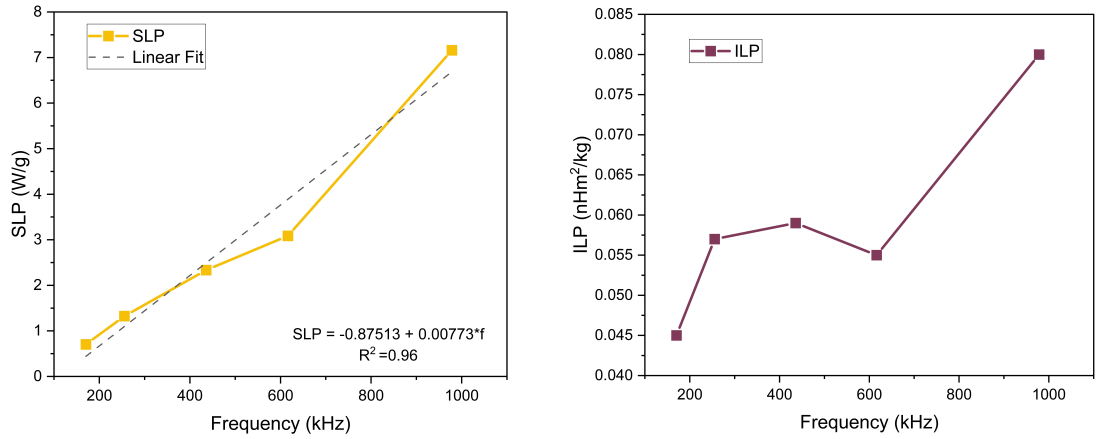

(a) SLP vs. frequency

(b) ILP vs. frequency

Figure 6.5: Plots correlating heat efficiency parameters to frequency for magnetite concentration of 50 mg/mL, field 9.55 kA/m, frequency 170.3-978.4 kHz

6.2.1. Discussion

Magnetite nanoparticles in the 20-30 nm range fall within the superparamagnetic regime, therefore heat generation happens via relaxation mechanism.
Relaxation heating increases directly with higher values of frequency, and this is proven by the experimental results of SLP in this section (Figure 6.5). It has to be noted that Brownian relaxation is not affected by the amplitude and frequency of the applied field, therefore varying this parameters, as done in this set of tests affected only the Neel component of relaxation.

The generated power, expressed via SLP and ILP parameters, can be linearly correlated to the frequency values.
Linear interpolation of SLP experimental points was performed and depicted in Figure 6.5a, showing good agreement with the Linear Response Theory and research performed by Cobianchi et Al. [16].

Moreover, temperature vs. time curves in Figure 6.3 show similar trends to the ones observed in section 6.1. An initial linear regime, followed by an exponential temperature rise, can be observed from this set of tests. This behaviour suggests that similar heat loss mechanisms take place when both dry and fluid samples are tested. It follows that no significant convection phenomena take place within the ferrofluid, and most of the heat losses can be attributed to air convection and radiation mechanisms.

Another observation can be formulated with regards to the frequency range used for this set of experiments.
MagneTherm tests, as performed in this research, are intended as a preliminary step to evaluate the suitability of nanoparticles as heat susceptors for fusion bonding of polymers. Similar tests can be found in literature [91], where preexisting industrial induction equipment was used. In this case, higher frequencies (2-7 MHz) were employed, and Curie temperature was reached for Nickel nanoparticles at 7 MHz. Experiments performed in this section for varying values of frequency reached a steady-state regime at temperatures largely lower than theoretical Curie temperature for magnetite. This behaviour suggests that future applications of nanoparticles for induction heating of polymers might benefit from the use of higher frequency ranges.

6.3. Influence of applied field

Once again, five 1 mL samples extracted from batch K (Table 4.6), with ideal concentration of 50 mg/mL, were employed for testing with Magnetherm equipment. The tests were conducted by placing the vials at the centre of the 9 turn coil and by exposing them to an alternating magnetic field of strength 3.18, 4.77, 6.37, 7.96 and 9.55 kA/m at a frequency of 978.4 kHz.

The full temperature profiles developed during the tests were recorded via fibre optic sensor kept in the middle of the vial and are depicted below in Figure 6.6:

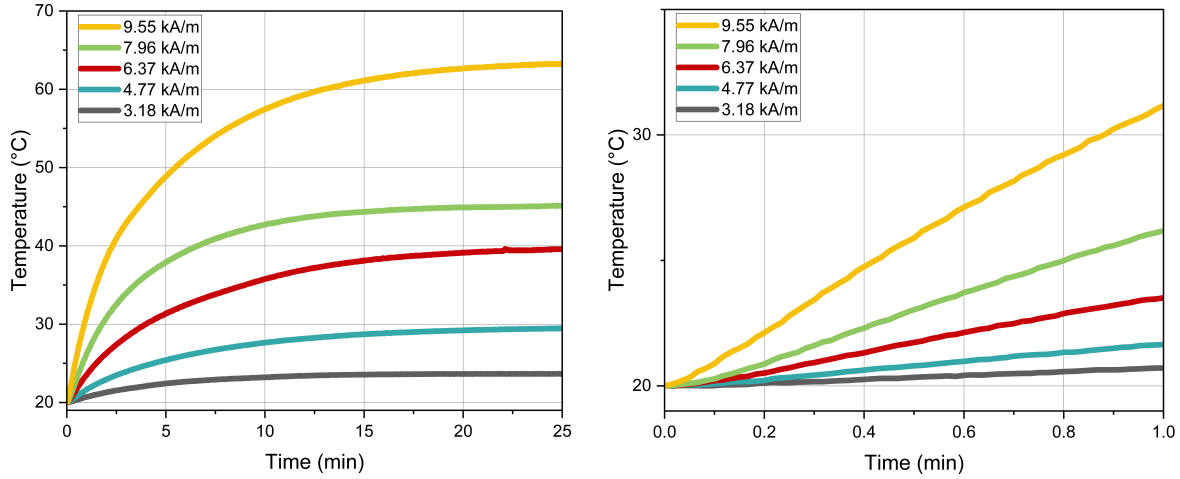

(a) Full temperature profile (0-25 min.)

(b) Temperature profile, zoomed (0-1 min.)

Figure 6.6: Temperature vs. time evolution plots for magnetite concentration of 50 mg/mL, frequency 978.4 kHz, field strength 3.18-9.55 kA/m

Graphs showing the temperature rise and the maximum temperature reached during simulations against frequency are depicted in Figure 6.7:

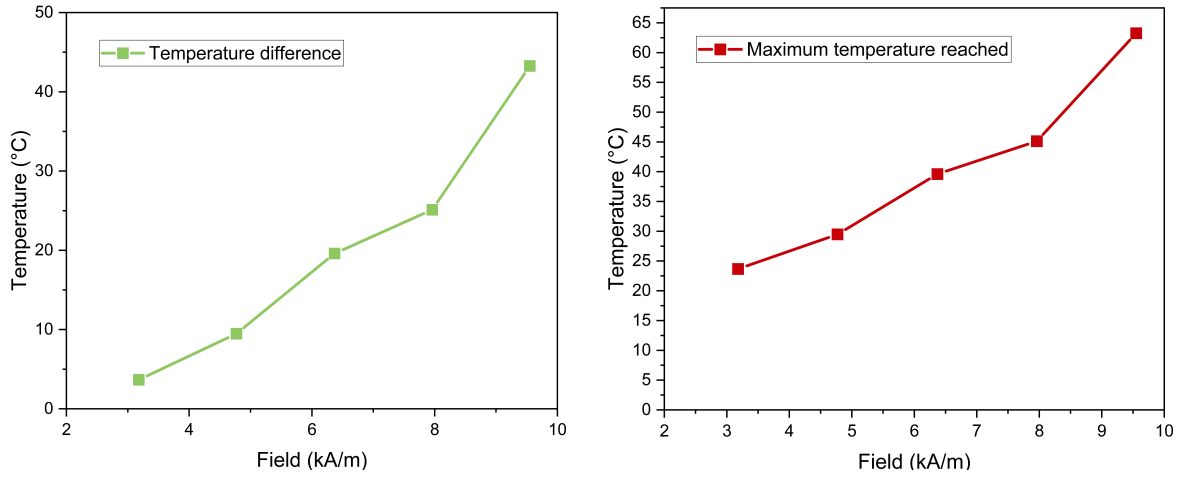

(a) Temperature rise vs. field

(b) Max reached temperature vs. field

Figure 6.7: Plots of temperature generation vs. frequency for magnetite concentration of 50 mg/mL, frequency 978.4 kHz, field strength 3.18-9.55 kA/m

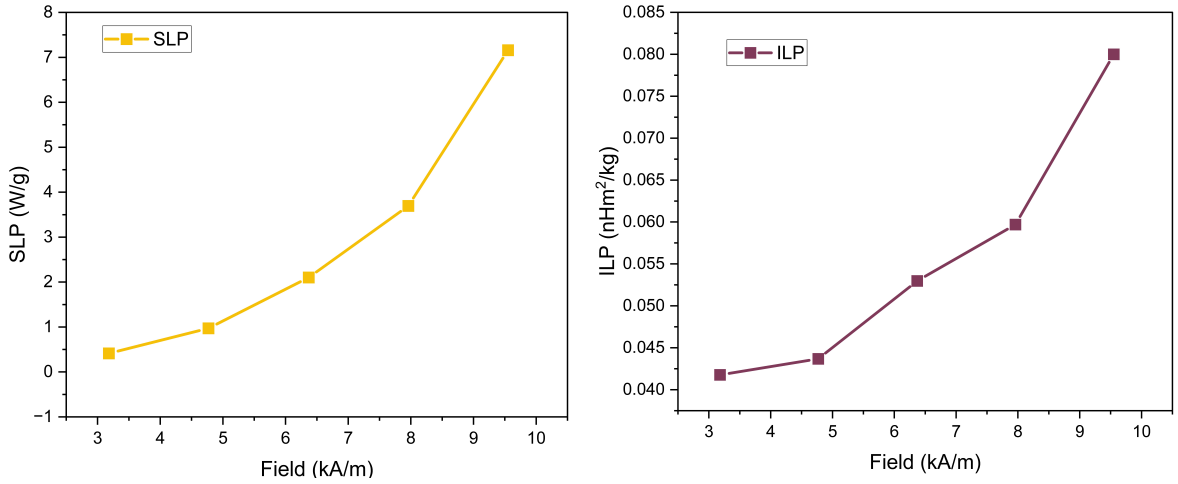

(a) SLP vs. field strength

(b) ILP vs. field strength

Figure 6.8: Plots correlating heat efficiency parameters to frequency for magnetite concentration of 50 mg/mL, frequency 978.4 kHz, field strength 3.18-9.55 kA/m

6.3.1. Discussion

Once again, despite insulation layers, similarly to previous experimental observations from section 6.1 and section 6.2, the non-adiabatic trend of the tests was observed in this set of experiments.

Results emerging from experiments with increasing strength values of alternating magnetic field clearly highlight the existing correlation between this parameter and heating capabilities of the ferrofluids. Greater heat generation is confirmed both by the higher temperature and heating rates developed by samples exposed to increasing field strengths and (Figure 6.6) by their correspondent SLP and ILP values (Figure 6.8).
This behaviour is well reported and described in literature, not only in the case of magnetic hyperthermia [67], but also for particulate polymer films [91].
The applicability of Linear Response Theory to the SLP power generation (as expressed by [16]) was verified. A polynomial fit was performed to test the quadratic dependence of calculated SLP values from the field strength ($SLP \propto H^2$) . The results are reported below in Figure 6.9, showing a good agreement of the experiments with this model.

The coefficient of determination for this fitting of the model was calculated to be $R^2 = 0.965$. This statistical parameter quantifies the goodness-of-fit of the chosen model and should be as close as possible to 1 in order to identify its suitability. Therefore, R^2 identifies the quadratic field model as a proper model for this case.
However, applicability of the Linear Response Theory needs to be better explored. As discussed in section 2.4, the ξ parameter defines the applicability of this model [16]:

$$\xi = \frac{\mu_0 M_s V H}{k_B T} < 1 \tag{6.4}$$

Below, in Figure 6.10, the evolution of the ξ parameter for different particle sizes has been plotted against field values, for room temperature (300 K), with a saturation magnetization of 90 emu/g.
This graph can be useful to identify the limitations of applicability of LRT. As can be seen, magnetite with a 20 nm diameter follows the $\xi < 1$ criterion for very low field values, below 2 kA/m. The tests reported in this section were performed in a 3.18-9.55 kA/m field

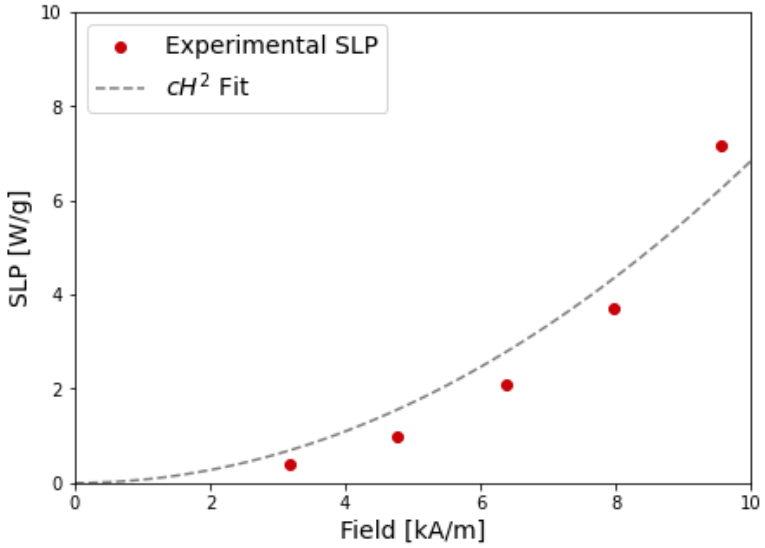

Figure 6.9: Experimental power generation (SLP) dependence from H^2 (c=0.068)

range, indicating the possible need of another empirical model to interpret the results. The introduction of the Rayleigh model, with a cubic dependence of SLP from the field amplitude ($SLP \propto H^3$) might pose a solution to this problem.
However, this observation introduces some additional complexity to the problem, as other types of heat generation phenomena, less known and measurable, might be present in these conditions (such as hysteresis losses or viscous losses).

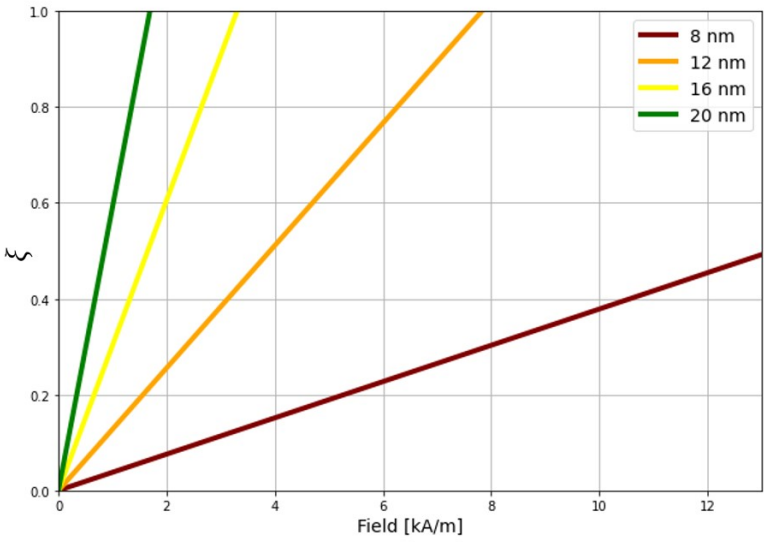

Figure 6.10: Experimental power generation (SLP) dependence from H^2 (c=0.068)

6.4. Influence of magnetic nanoparticles concentration

This section reports the results obtained for MagneTherm induction heating measurements of various suspensions with different magnetite concentrations.
Samples of 1 mL were prepared, with an increase in magnetite concentration from 5 to 100 mg/mL (according to Table 4.5 and Table 4.6). The tests were conducted by placing the vials at the centre of the high-field coil and by exposing them to an alternating magnetic field of strength 6.37, 9.55 and 12.73 kA/m at a frequency of 992 kHz.
Data from tests of suspensions at 15 mg/mL concentration was corrupted during acquisition and therefore is not reported in the graphs.
Data has been manipulated and plotted below. Figure 6.11 depicts SLP values for different applied field strengths plotted against particle concentration for the 8 and 20-30 nm size ranges, while Figure 6.12 shows a comparison of heat generation (SLP and ILP) between the two particle sizes with respect to their concentrations.

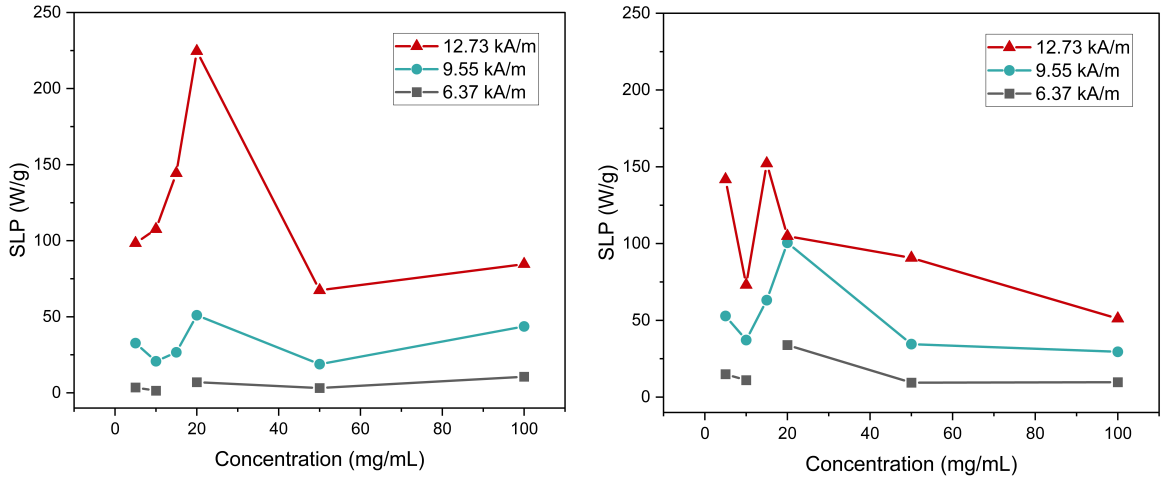

(a) SLP vs. concentration for magnetite (8 nm)

(b) SLP vs. concentration for magnetite (20-30 nm)

Figure 6.11: Plots correlating heat efficiency (SLP) parameter to magnetite concentration, frequency 992 kHz, field strength 6.37-12.73 kA/m

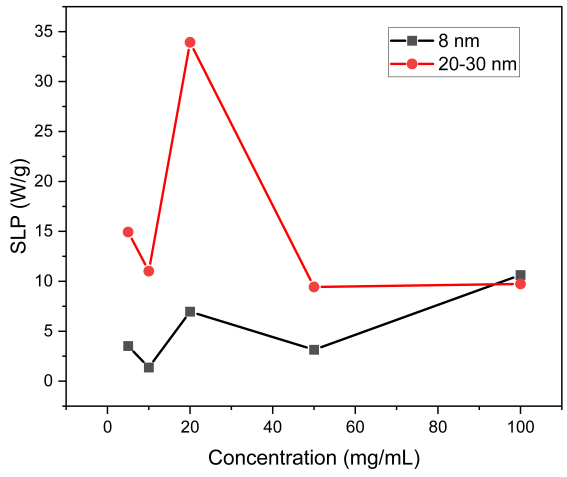

(a) SLP vs. concentration, 6.37 kA/m, 992 kHz

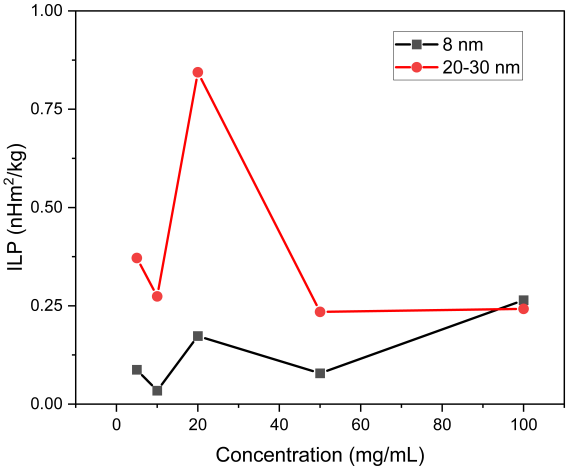

(b) ILP vs. concentration, 6.37 kA/m, 992 kHz

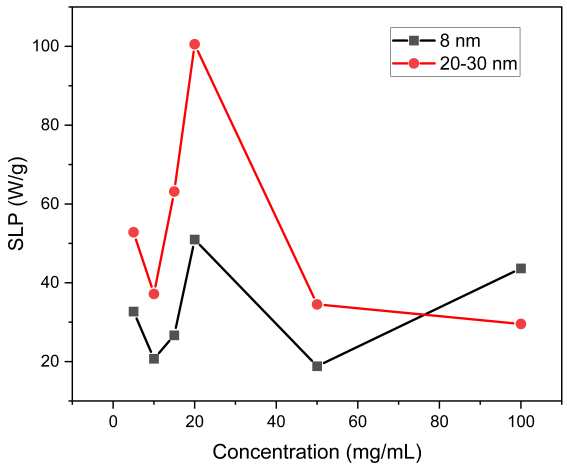

(c) SLP vs. concentration, 9.55 kA/m, 992 kHz

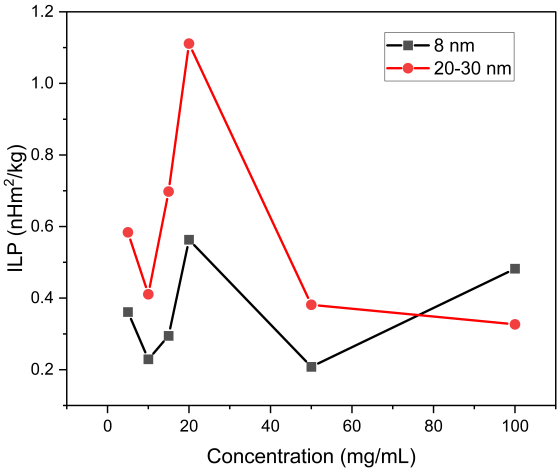

(d) ILP vs. concentration, 9.55 kA/m, 992 kHz

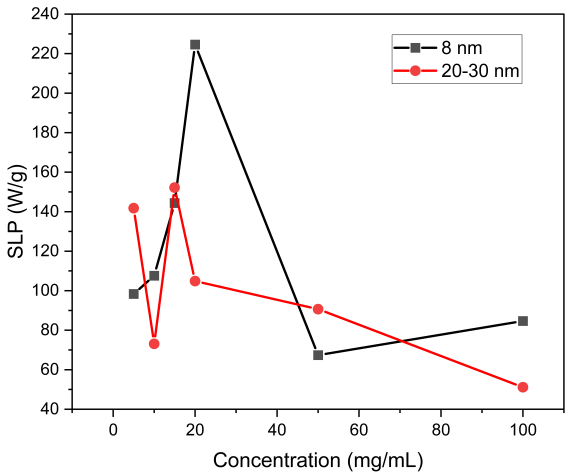

(e) SLP vs. concentration, 12.73 kA/m, 992 kHz

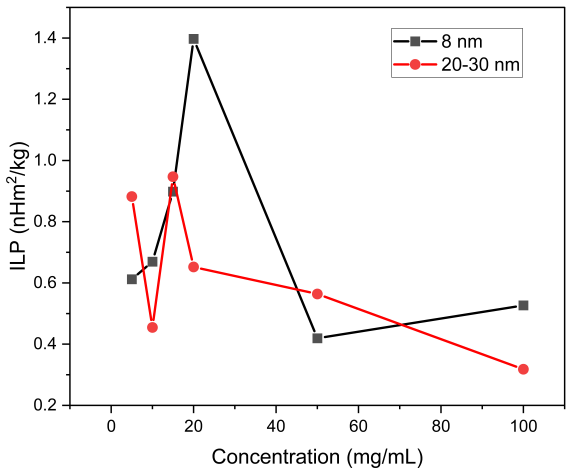

(f) ILP vs. concentration, 12.73 kA/m, 992 kHz

Figure 6.12: Graphs of SLP and ILP vs. magnetite nanoparticles concentrations for 6.37, 9.55, 12.73 kA/m field strength, 992 kHz

6.4.1. Discussion

In this section, the power generation (in the form of SLP) of various suspensions with different magnetite concentrations was measured.

An interesting behaviour emerges from the obtained results. All the SLP and ILP values show optimal heat generation from the tested suspensions between 10 and 20 mg/mL. Heat generation for concentrations outside of this window appears to be lower.
From literature, examples of similar behaviours were found by Lemine et Al. [50]. In their paper, it was attested that SLP values decrease for increasing concentrations of magnetite, even though the maximum reached temperature was higher for higher concentration, similarly to what was verified in this study. This behaviour can be connected, especially in the case of 20-30 nm magnetite, to an increase of particle-particle interactions. When the concentration is increased above a certain limit, interparticle dipolar interactions become intense, reducing the reorientation of magnetic moments and, consequently, the relaxation mechanisms.
The observed SLP trend can be linked to the fact that power generation and SLP evaluated by linear fitting of the initial part of the heating curve depends on a plethora of parameters that add complexity to the problem (viscosity, polydispersity, size, saturation, hydrodinamic size).

Another interesting aspect was derived from these results and requires to be discussed. All the heat generation data collected during experiments were simultaneously collected via fibre optic sensor and thermal camera. A delay was observed between the termination of exposure to the alternating magnetic field (coil OFF) and the heating generation of the suspension. This can indicate an additional phenomenon that requires to be taken into account: the heat generation deriving from the coil. Therefore, the original adiabatic heat generation equation $P = C_p \cdot \frac{\Delta T}{\Delta t}$ should be modified to take this effect into account:

$$P - P_L + P_{coil} = C_p \cdot \frac{\Delta T}{\Delta t} \tag{6.5}$$

Where P_L indicates the power losses due to air convection at each temperature in the form of a non-linear function and P_{coil} the heat generated by the coil. Both of these effects, once again, take place because of the non-adiabatic nature of the testing setup. However, modelling and including this aspect will require more tests and validation.

7

Characterization of magnetic nanoparticles

The detailed characterization of materials is essential to understanding their structure, properties, and induction heating performance. In this chapter, the outcomes of different characterization techniques used to analyze the morphological, chemical, magnetic, and functional properties of the considered materials are reported. These analyses are crucial for assessing their suitability for application as susceptors in induction welding of thermoplastics.
Results from characterization of Nickel nanopowder (section 7.1) are followed by magnetite (section 7.2), Chromium Dioxide (section 7.3) and finally Ni-Zn ferrite (section 7.4).

7.1. Nickel nanopowder

This section presents results and characterization data obtained from further tests performed on Nickel nanopowder.
Thermogravimetric experiments were performed to confirm the reliability of TGA as a method to obtain Curie temperatures of materials.
Furthermore, results from SQUID measurements are reported and explained to interpret the heat generation capabilities of Nickel powder shown previously in section 6.1.

7.1.1. Thermogravimetric Analysis

Transitions involving weight variations in the tested sample have been applied extensively to perform the calibration of thermogravimetric equipment. However, the non-isothermal, irreversible and kinetic nature of weight loss transitions represents a limiting factor in the search for proper calibration points (and suitable materials). Melting and magnetic transitions are currently recognized as the most reliable calibrating techniques for TGA. ASTM E158221 (Standard Test Method for Temperature Calibration of Thermogravimetric Analyzers) describes the aforementioned calibration practices.
Rods of reference materials are often used as standard calibration equipment for TGA. As can be seen in Table 7.1, these calibration points are accurately predicted on the basis of the offset of TGA weight curves, identifying the Curie temperature of the chosen material.

Table 7.1: Reference materials and their Curie temperatures as standard TGA calibration points

Reference material	Expected offset [°C]
Alumel	154.2
Nickel	355.4
Perkalloy	596
Iron	770
Cobalt	1121

Sensitivity study on the influence of heating rate

The sensitivity of gravimetric measurements was tested with respect to the applied heating rate. Multiple TGA runs were performed under applied magnetic field from room temperature up to 460° C at increasing heating rates (from 5° C/min to 100° C/min). The curves resulting from these tests are plotted below in Figure 7.1.

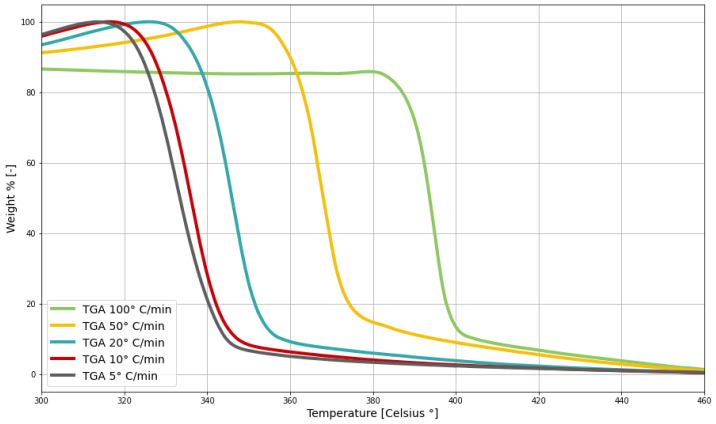

Figure 7.1: Thermogravimetric graphs of TGA runs of Nickel nanoparticles for various heating rates (from 5° C/min to 100° C/min) showing Curie temperature transition

Analysis of gravimetric data is normally performed by calculating how the weight of the sample is affected in relation to the initial sample mass:

$$W_i[\%] = \frac{W_i}{W_0} \cdot 100 \tag{7.1}$$

Where W_0 indicates the initial sample mass (theoretical 100% value) and W_i the mass of the sample measured at a certain temperature T_i at the instant in time t_i of data acquisition.

However, the acquired weight measurements have been normalised to better highlight the effect of the transition from ferromagnetic to paramagnetic state:

$$\Delta W = W_{max} - W_{min} \tag{7.2}$$

$$W_i[\%] = \frac{W_i - W_{min}}{\Delta W} \cdot 100 \tag{7.3}$$

Where W_{min} indicates the minimum sample mass (equivalent to 0% mass, in this case), W_{max} the maximum or initial sample mass (theoretical 100%), ΔW the mass loss and W_i the mass of the sample measured at a certain temperature T_i at the instant in time t_i of data acquisition.

The outcomes of multiple tests were analyzed and Curie temperature of different heating rate tests was found by calculation of curves offsets, as shown below in Figure 7.2. A summary of all the relevant parameters and results from TGA tests can be found in Table 7.2.

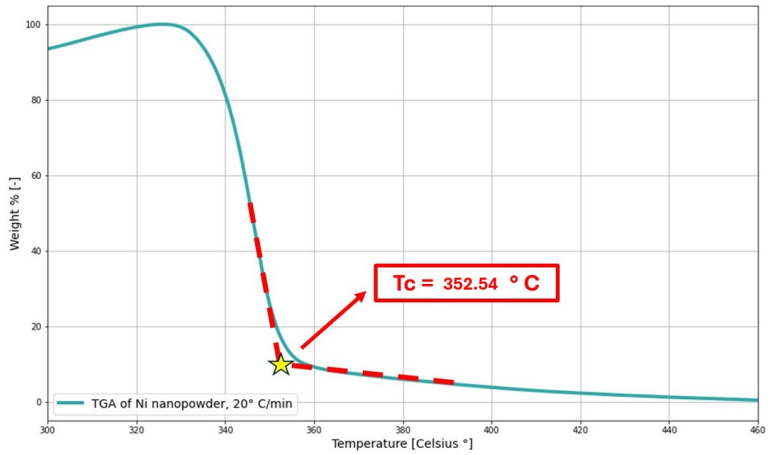

Figure 7.2: Calculation of offset point from TGA curve, 20° C/min heating rate

Table 7.2: Summary of thermomagnetic data from TGA measurements of Ni nanopowder at various heating rates

	Heating rate [° C/min]				
	100	**50**	**20**	**10**	**5**
Initial mass [mg]	9.263	8.955	9.911	8.769	8.186
Delta m [mg]	0.636	0.617	0.859	0.616	0.579
DTGA peak [° C]	395.28	366.54	345.62	336.27	332.47
Tc from offset [° C]	398.70±0.22	373.06±0.12	352.54±0.33	344.28±0.58	342.61±1.69

Literature exploring the use of Curie temperature as a TGA calibration method suggests that lower heating rates can ensure improved accuracy. It was reported that for a heating rate below 20° C/min, measured Curie temperatures fall within 2° C of literature values, dropping to 1° C for a 5° C/min heating rate [78].

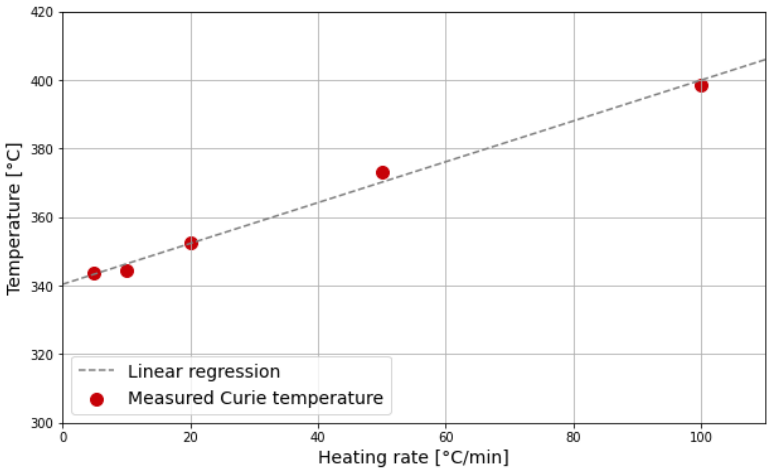

Figure 7.3: Experimental values from TGA of Curie temperature for Ni nanopowder as a function of the used heating rate

Comparison of standard TGA with TGA under applied magnet

Previous thermogravimetric tests showed a sharp drop in apparent weight. However, in order to confirm (and better visualize) how this phenomenon is connected to a magnetic phase transition, another experiment was performed.

Additional themogravimetric experiments were carried out in an inert gas purged furnace, under a 20 mL/min Nitrogen flow. Nickel nanopowder was heated under an applied magnetic field and under standard TGA conditions from room temperature up to 460° C, at a 5° C/min heating rate. The results of both tests are reported in the graph below (Figure 7.4).

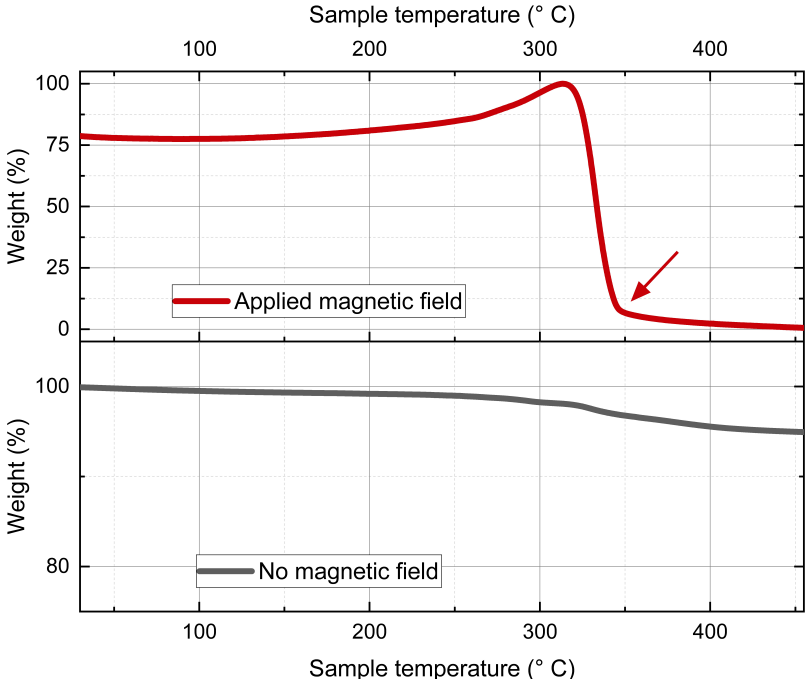

Figure 7.4: TGA of Ni nanopowder with and without applied magnetic field, heating rate 5° C/min

As indicated by the arrow in the top graph (Figure 7.4), a noticeable inflection in the weight curve can be observed when measurement is performed in the presence of a magnet. A decrease in overall mass is observed in both testing conditions. However, the absolute value of this difference is sensibly different when TGA is performed under magnetic field: 0.859 mg compared to a 0.103 mg difference in the normal TGA run.

7.1.2. SQUID

A SQUID magnetometry measurement was performed to gain knowledge regarding the magnetic properties of Nickel nanopowder.

The test was conducted by continuous movement of the sample via the Reciprocating Sample Option (RSO) under an oscillating magnetic field, in a field range between 1 T and -1 T (1 T = 10000 Oe). Temperature control was achieved by helium supercooling of the unit until a stable 300 K temperature was maintained throughout the measurement. Finally, the obtained hysteresis loop for Nickel was reported and is shown in Figure 7.5.

From the magnetization-field curve it was possible to extrapolate the significant magnetic properties of Nickel, reported below in Table 7.3.

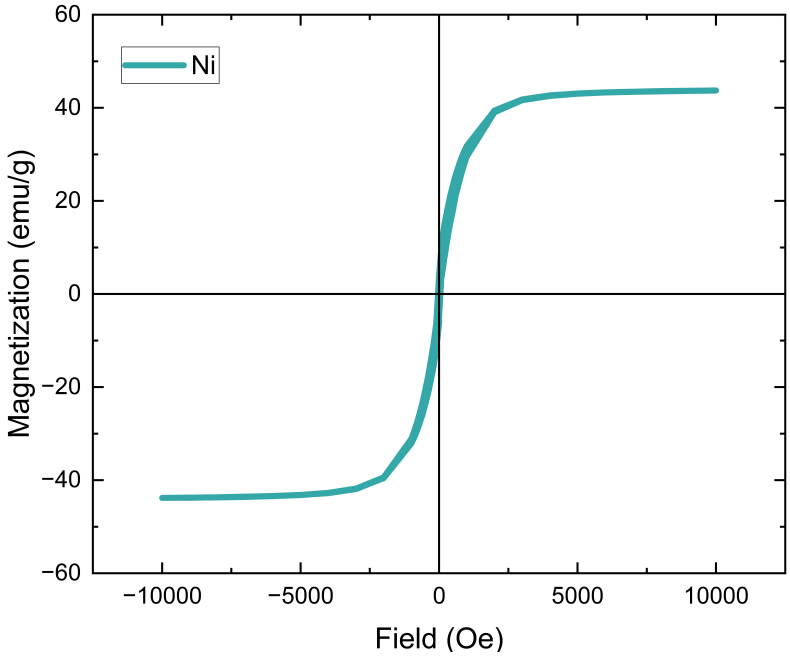

Figure 7.5: Magnetization curve of Nickel nanopowder obtained from SQUID equipment

Table 7.3: Magnetic properties of Ni nanopowder from SQUID measurement

Hysteresis loop parameter	Value
Sample mass [mg]	1.27
Coercivity [Oe]	39.62
Saturation magnetization [emu/g]	43.70
Retentivity [emu/g]	4.10

7.1.3. Discussion

Nickel nanopowder used in this section was used as a standard material to demonstrate the capabilities of TGA in assessing Curie temperature of materials.
The powder showed a 342.61°C Curie temperature for very low heating rates. This is in good agreement for similar TGA tests performed at similar heating rates [73] and is lower than bulk Curie temperature for Nickel, as expected. From this property it is also possible to hypothesize, thanks to the research performed by Nepijko et Al. [69], that the nanopowder is predominantly in the 20-30 nm range. However, this can only be confirmed via TEM exploration.
This Curie temperature also follows withing processing temperature ranges of multiple polymers. It shows potentiality for induction heating, and consequently welding, of thermoplastics such as PEI, PPS and LM-PAEK.

The found magnetic properties are modest. Both values of coercivity and retentivity are low, and saturation magnetization was found to be 43.70 emu/g, lower, as expected, than the bulk saturation magnetization for Nickel (57.50 emu/g, [84]).

7.2. Magnetite nanoparticles

This section presents results and characterization data obtained from further tests performed on magnetite nanoparticles (in the 8 and 20-30 nm size ranges).
Thermogravimetric experiments were performed to confirm the reliability of TGA as a method to obtain Curie temperatures of materials.
Furthermore, results from SQUID measurements are reported and explained to interpret the heat generation capabilities of magnetite nanoparticles shown previously in chapter 6.

7.2.1. Thermogravimetric Analysis

Thermogravimetric analyses of Fe_3O_4 samples was conducted, following the procedure described in section subsection 5.2.3. In this case, a heating rate of 5 ° C / min was chosen, in order to reduce any possible kinetic effect of reactions and transitions.
Data was acquired and manipulated. Analysis of gravimetric points (acquired as absolute mass data) was performed by calculating how the mass of the sample is affected in relation to the initial sample mass via the relation:

$$W_i[\%] = \frac{W_i}{W_0} \cdot 100$$

Where W_0 indicates the initial sample mass (theoretical 100% value) and W_i the mass of the sample measured at a certain temperature T_i at the instant in time t_i of data acquisition.

Graphs of mass (%) plotted against temperature are reported below in Figure 7.6 and Figure 7.7.

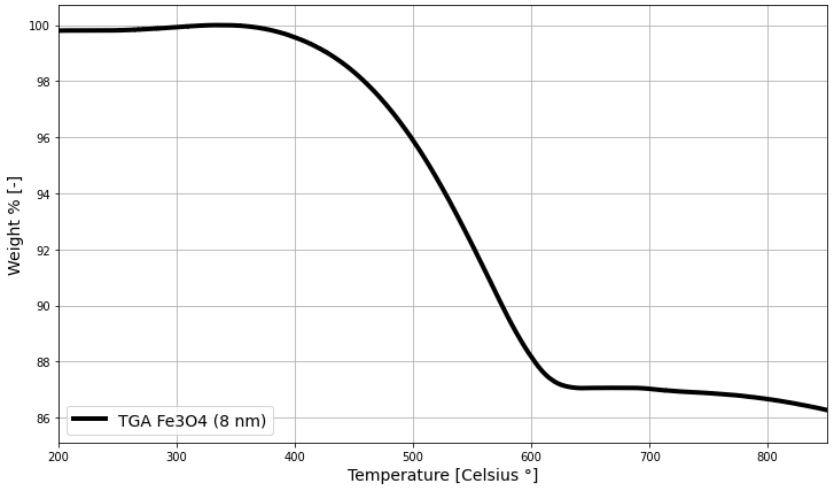

Figure 7.6: Thermogravimetric graph of magnetite (8 nm) nanoparticles

Table 7.4: Summary of thermomagnetic data from TGA measurements of Fe_3O_4 (8 nm)

TGA parameter	Value
Initial mass [mg]	10.80
Δ m [mg]	1.63
DTGA peak [°C]	567.09
Tc from offset [°C]	607.96±0.81

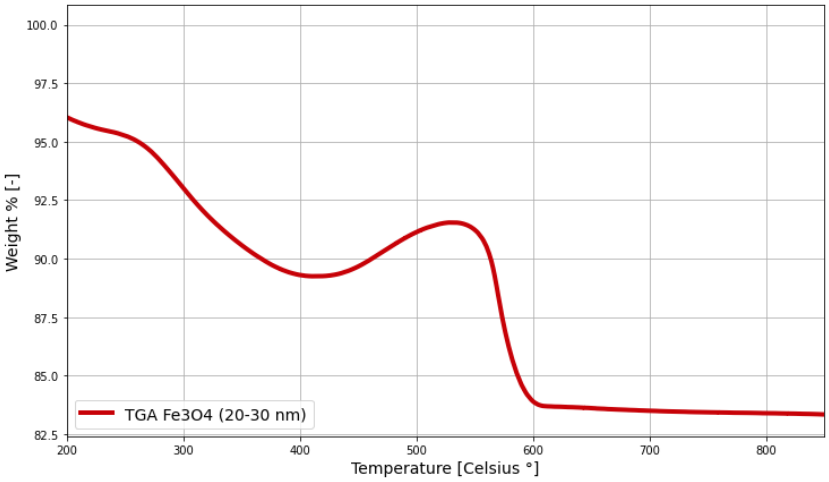

Figure 7.7: Thermogravimetric graph of magnetite (20-30 nm) nanoparticles

Table 7.5: Summary of thermomagnetic data from TGA measurements of Fe_3O4 (20-30 nm)

TGA parameter	Value
Initial mass [mg]	10.27
Δ m [mg]	1.89
DTGA peak [°C]	570.10
Tc from offset [°C]	588.60±0.72

All the relevant values obtained from TGA were reported in Table 7.4 and Table 7.5.
Fe_3O_4 samples showed a relative mass loss of 15% and 18.4% under the application of magnetic field. This indicates a stronger magnetic attraction of the 20-30 nm magnetite nanoparticles with respect to the 8 nm particles.
The Curie temperature of these nanoparticles was found to be higher than bulk magnetite (585° C [35]) in both cases: 607.96 °C for the 8-nm size and 588.60 ° C for the 20-30 nm sample. This behaviour confirms an alteration (at least partial) of the nanoparticles due to oxidation.
Moreover, multiple TGA runs performed for magnetite nanoparticles in the 20-30 nm size range, shoed a relative mass loss around 400 °C, before the proper Curie mass loss is reached. This event cannot be properly justified. A possible explanation could be linked to an additional oxidation of the particles, however, this is not confirmed by literature and requires further investigation.

7.2.2. SQUID

Magnetic properties of magnetite nanoparticles were studied by measurements conducted via SQUID equipment. A SQUID machine (Superconducting Quantum Interference Device), as explained in subsection 5.2.4, was used to perform measurements at room temperature (300 K) in the -1 to 1 T range.
Magnetization curves of magnetite nanoparticles from SQUID are given in Figure 7.8. All relevant parameters are then extrapolated and reported in Table 7.6 and Table 7.7.

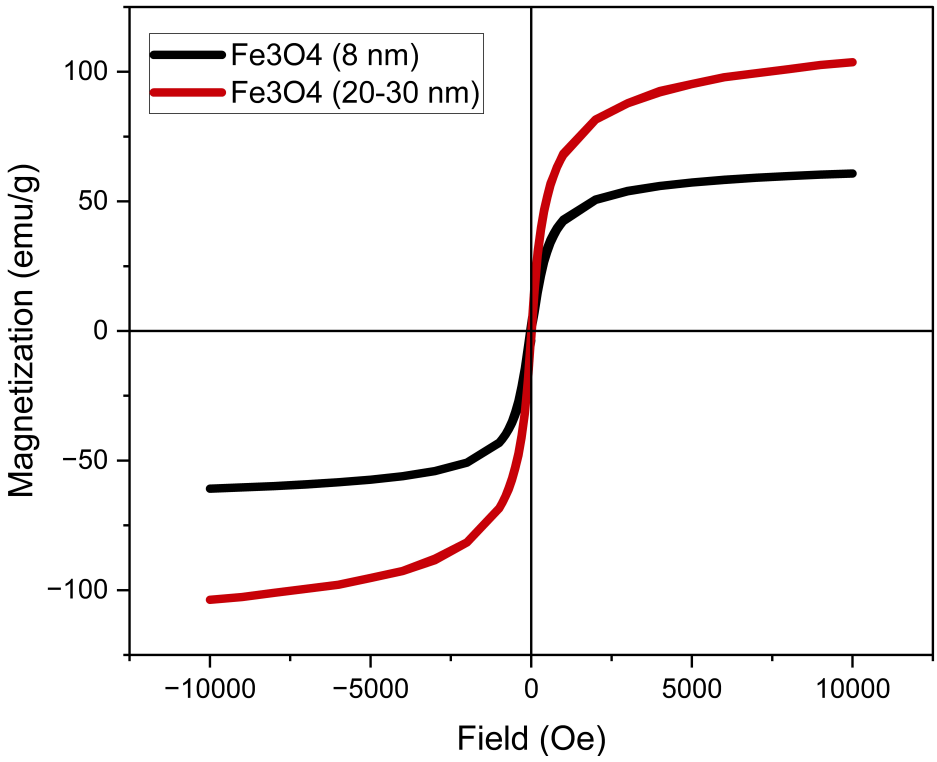

Figure 7.8: Magnetization curve of magnetite nanoparticles (20-30 nm size) obtained from SQUID equipment

Table 7.6: Magnetic properties of Fe_3O_4 (8 nm) nanoparticles from SQUID measurement

Hysteresis loop parameter	Value
Sample mass [mg]	0.54
Coercivity [Oe]	32.42
Saturation magnetization [emu/g]	60.77
Retentivity [emu/g]	2.91

Table 7.7: Magnetic properties of Fe_3O_4 (20-30 nm) nanoparticles from SQUID measurement

Hysteresis loop parameter	Value
Sample mass [mg]	0.19
Coercivity [Oe]	3.75
Saturation magnetization [emu/g]	103.68
Retentivity [emu/g]	0.69

When magnetic parameters of the two magnetite samples are compared, higher coercivity can be observed for the 8 nm magnetite nanoparticles. This In absolute terms, this value is still low enough to confirm that both type of MNPs fall within the superparamagnetic range.

Higher saturation magnetization values were found for the 20-30 nm particle range. This behaviour matches what can be found in literature. It was previously reported that for MNPs up to 100 nm a direct correlation between saturation and particle size can be drawn [51]. However, it is relevant to highlight that magnetite in the 20-30 nm size range showed a saturation value of 103.68 emu/g, higher than the reported value of 92 emu/g for bulk magnetite [51].

7.2.3. X-Ray Diffractometry

D8 ADVANCE x-ray powder diffractometry equipment from Bruker (Billerica, U.S.A.), using a Cu $K\alpha$ radiation source at 40 kV and 25 mA, was used to perform measurements on magnetite nanopowders. The incident X-ray beam used had a wavelength of 1.54060 Å.

X-ray diffraction data of magnetite nanoparticles samples was acquired during a 15 minutes scan. The obtained XRD patterns, as shown in Figure 7.9 showed a 94 % match with JCPDS 75-0078 reference card for Fe_3O_4 (8 nm) nanoparticles and an 88% match for Fe_3O_4 (20-30 nm).

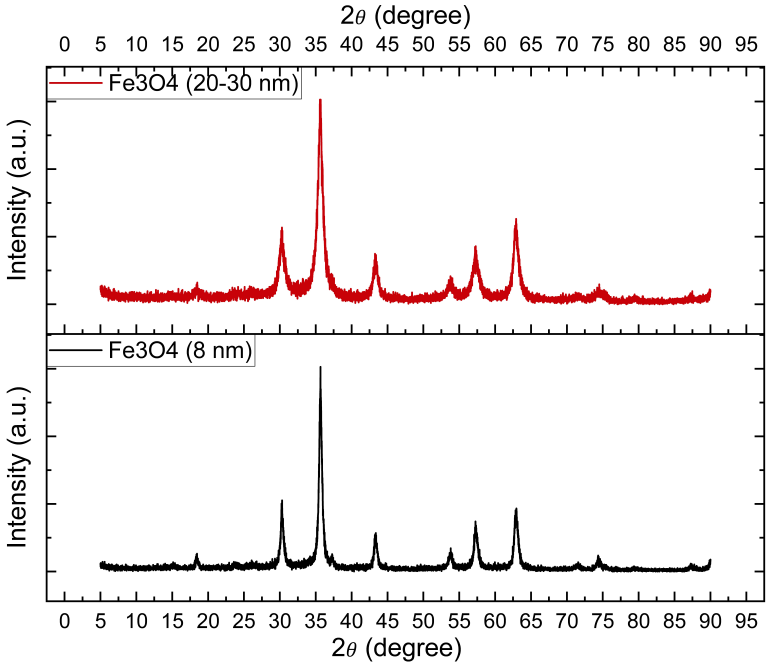

Figure 7.9: XRD graphs obtained for magnetite particles of size 8 nm and 20-30 nm

The crystallite dimensions were found to be 8.8 nm for Fe_3O_4 (8 nm) and 20.59 nm for Fe_3O_4 (20-30 nm), in good agreement with the theoretical expected values. No significant effects deriving from the presence of impurities or high strains in the lattice can be observed.

Moreover, some observations on the intensity of the peaks can be formulated.
High and sharp peaks, as can be seen in Figure 7.9, suggest the presence of a strong diffraction signal. This allows to confirm the presence of a distributed and well defined crystalline structure. Calculations of grain size dimensions identified

Table 7.8: Summary of diffraction peaks from XRD data of Fe_3O_4 (8 nm) nanoparticles: Miller indices, interplanar spacings and scattering angles for standard and measured data

	Standard data (Magnetite)		**Standard data (Maghemite)**		**Measured data**	
hkl	**d (Å)**	**2θ (°)**	**d (Å)**	**2θ (°)**	**d (Å)**	**2θ (°)**
111	4.798	18.478	4.822	18.384	4.807	18.444
220	2.938	30.399	2.953	30.241	2.943	30.343
311	2.506	35.810	2.512	35.631	2.510	35.742
222	2.399	37.460	2.412	37.250	2.403	37.389
400	2.078	43.528	2.089	43.285	2.081	43.445
331	1.906	47.633	1.969	46.072	1.962	46.228
422	1.696	54.016	1.705	53.734	1.699	53.910
511	1.599	57.588	1.607	57.273	1.602	57.473
440	1.469	63.251	1.476	62.927	1.472	63.123
531	1.405	66.514	1.432	65.074	1.428	65.302
620	1.314	71.784	1.320	71.378	1.316	71.633
533	1.267	74.868	1.273	74.473	1.270	74.709
622	1.253	75.885	1.259	75.445	1.255	75.723
444	1.199	79.914	1.205	79.449	1.202	79.740
551	1.164	82.902				
642	1.110	87.843	1.116	87.307	1.112	87.642

Table 7.9: Summary of diffraction peaks from XRD data of Fe_3O_4 (20-30 nm) nanoparticles: Miller indices, interplanar spacings and scattering angles for standard and measured data

	Standard data (Magnetite)		**Standard data (Maghemite)**		**Measured data**	
hkl	**d (Å)**	**2θ (°)**	**d (Å)**	**2θ (°)**	**d (Å)**	**2θ (°)**
111	4.798	18.478	4.822	18.384	4.815	18.410
220	2.938	30.399	2.953	30.241	2.949	30.285
311	2.506	35.810	2.512	35.631	2.515	35.674
222	2.399	37.460	2.412	37.250	2.408	37.318
400	2.078	43.528	2.089	43.285	2.085	43.360
331	1.906	47.633	1.969	46.072	1.966	46.137
422	1.696	54.016	1.705	53.734	1.703	53.802
511	1.599	57.588	1.607	57.273	1.605	57.358
440	1.469	63.251	1.476	62.927	1.474	62.993
531	1.405	66.514	1.432	65.074	1.430	65.167
620	1.314	71.784	1.320	71.378	1.319	71.481
533	1.267	74.868	1.273	74.473	1.272	74.547
622	1.253	75.885	1.259	75.445	1.257	75.559
444	1.199	79.914	1.205	79.449	1.204	79.563
551	1.164	82.902				
642	1.110	87.843	1.116	87.307	1.115	87.440

Locations of crystallinity peaks are found to be in good accordance with standard reported data for magnetite. However a slight shift of all the peaks towards lower peak positions (2θ) can suggest a partial oxidation of the particles.
The oxidation of magnetite (Fe_3O_4) into maghemite (Fe_2O_3) is a spontaneous reaction [52], and proceeds according to the following chemical reaction:

$$Fe_3O_4 + 2H^+ \rightarrow Fe_2O_3(\gamma) + Fe^{2+} + H_2O \tag{7.4}$$

It was also proven that the transformation is favoured by anaerobic conditions [32] such as the ones applied for storage. This information confirms the hypothesis of partial oxidation of the sample.

7.2.4. Discussion

The reported characterization campaign performed on magnetite nanoparticles provided interesting information regarding their morphology and magnetic properties.
First, XRD measurements confirmed the possible, and at least partial, oxidation of both magnetite (8 and 20-30 nm) particle samples to maghemite. At this stage, it is not possible to clearly state wether oxidation involved entire particles or just their outside layer and further investigation is needed. Secondly, crystallite sizes were found to be in good agreement with expected dimensions of nanoparticles.

Magnetic testing via SQUID confirmed the superparamagnetic character of both batches of particles. No hysteresis was observed and high values of saturation magnetization emerged (respectively 60.77 and 103.68 emu/g).
Two interesting points should be made on the basis of these results:

- The saturation magnetization value for 20-30 nm magnetite nanoparticles exceeds even the one for bulk magnetite found in literature. This could be explained by the (at least partial) oxidation of magnetite into maghemite. As reported by the manufacturer, the synthesis route adopted for these nanoparticles is laser pyrolisis. In a similar case reported in literature [15], maghemite nanoparticles of similar size produced by pyrolisis showed a very high saturation magnetization (125.7 emu/g), confirming this theory.
- Considering the superparamagnetic character of these particles and the consequent applicability of Linear Response Theory, a linear dependence of heat generation on saturation magnetization is expected. However, this was not always the case, as Fe_3O_4 in the 8 nm size range showed higher heating efficiencies in the outcomes shown both in section 6.1 and in section 6.4. Once again, this can be explained by dipole-dipole interactions established among particles in a close compact scenario, such as the one of a dry sample or high concentration magnetic fluid.

7.3. Chromium dioxide nanopowder

This section presents results and characterization data obtained from tests performed on Chromium Dioxide nanopowder.
Thermogravimetric experiments were performed to study the Curie temperature of the material. Furthermore, results from SQUID measurements are reported and explained to interpret the heat generation capabilities of Chromium Dioxide powder shown previously in section 6.1. Finally, X-Ray diffractometry data is shown and crystallographic information is retrieved from interpretation of the diffraction pattern.

7.3.1. Thermogravimetric Analysis

Thermogravimetric analysis of Chromium Dioxide samples was conducted, following the procedure described in section subsection 5.2.3. In this case, a heating rate of 5 ° C / min was chosen, in order to reduce any possible kinetic effect of reactions and transitions.
Data was acquired and manipulated. Analysis of gravimetric points (acquired as absolute mass data) was performed by calculating how the mass of the sample is affected in relation to the initial sample mass via the relation:

$$W_i[\%] = \frac{W_i}{W_0} \cdot 100$$

Where W_0 indicates the initial sample mass (theoretical 100% value) and W_i the mass of the sample measured at a certain temperature T_i at the instant in time t_i of data acquisition.

The graph of mass (%) plotted against temperature is reported below in Figure 7.10.
No noticeable changes in color were observed after heating the sample. The gravimetric curve

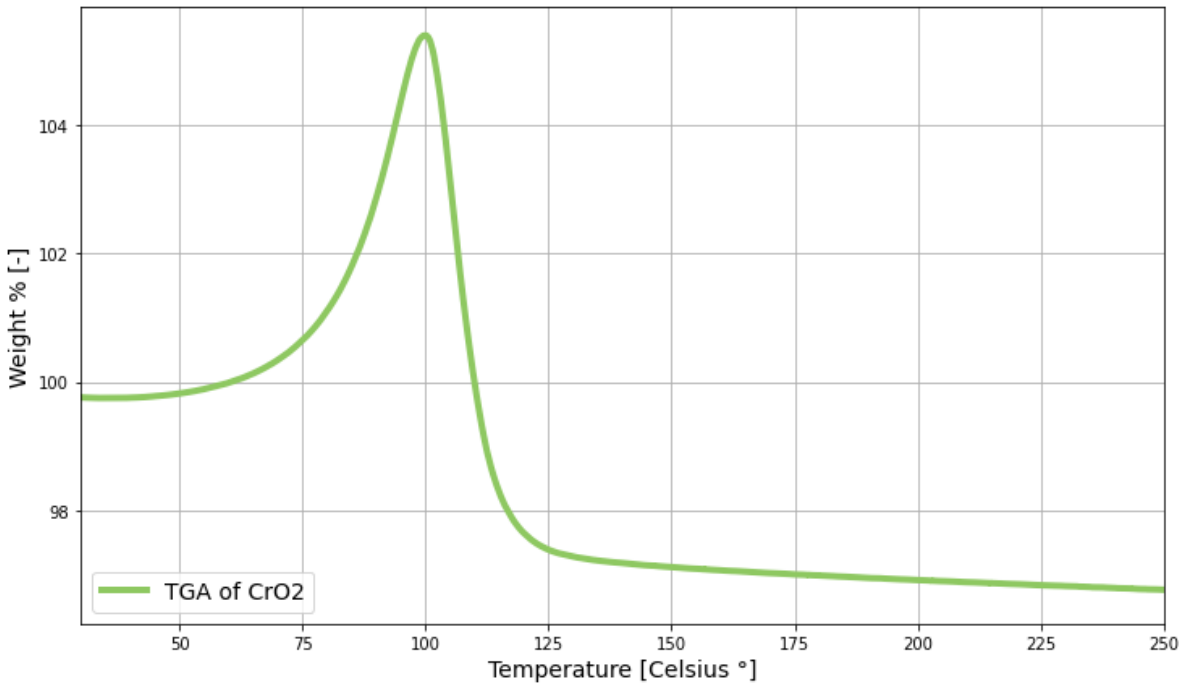

Figure 7.10: Thermogravimetric graph of Chromium Dioxide nanopowder

under applied magnetic field shows two significant events: a peak and an inflection point.

Chromium Dioxide samples showed a mass gain at 99.91° C, with a relative peak of 105.41%. This phenomenon cannot be clearly explained. Proof of CrO2 chemical transitions around this temperature cannot be found in literature. Considering the instability of Chromium Dioxide at room temperature and atmospheric pressure, the peak could be linked to the effect of oxidation of CrO2 to Cr2O3. However, no visible changes in the colour of the sample were shown and no solid proof of this was found.
From significant values of TGA parameters, reported below in Table 7.10, a relative mass loss of 3.3 % was found. The experimental Curie temperature was found to be 113.85°C, showing a 1% difference from literature value (112.85°C, [35]).
An additional comparison of a standard TGA test with this TGA result (under applied magnetic field) can be found in the appendix in Figure B.1.

Table 7.10: Summary of thermomagnetic data from TGA measurements of CrO_2

TGA parameter	Value
Initial mass [mg]	9.92
Δ m [mg]	0.33
DTGA peak [°C]	105.57
Tc from offset [°C]	113.85±0.79

7.3.2. SQUID

A SQUID magnetometry measurement was performed to gain knowledge regarding magnetic properties of Chromium Dioxide.
The test was conducted by continuous movement of the sample via the Reciprocating Sample Option (RSO) under an oscillating magnetic field, in a field range between 1 T and -1 T (1 T = 10000 Oe). Temperature control was achieved by helium supercooling of the unit until a stable 300 K temperature was maintained throughout the measurement. Finally, the obtained hysteresis loop for Chromium Dioxide was reported and is shown in Figure 7.11.

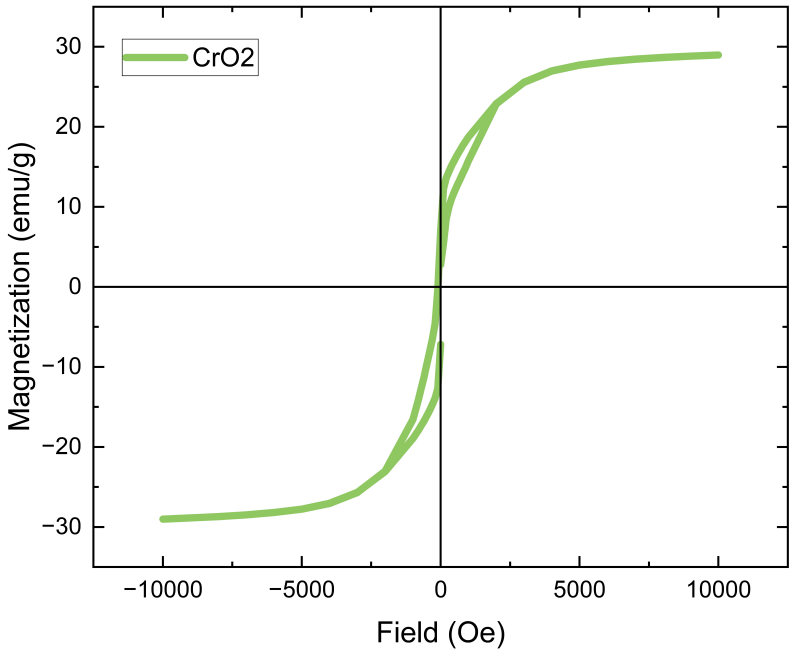

Figure 7.11: Magnetization vs. field loop of CrO_2 nanopowder obtained from SQUID magnetometer

From the magnetization-field curve it was possible to extrapolate the significant magnetic properties of CrO_2, reported below in Table 7.11.

Table 7.11: Magnetic properties of CrO_2 nanopowder from SQUID measurement

Hysteresis loop parameter	Value
Sample mass [mg]	1.16
Coercivity [Oe]	3.88
Saturation magnetization [emu/g]	28.99
Retentivity [emu/g]	7.09

It is particularly relevant to highlight the low measured value for saturation magnetization of the tested material: 28.99 emu/g for CrO_2, compared to 91 emu/g observed for bulk magnetite. This parameter is strongly influenced by morphology, synthesis route and size of considered nanoparticles, therefore, it is necessary to correlate it with information obtained from TEM data.

7.3.3. X-Ray Diffractometry

X-ray diffraction data of chemical-grade chromium dioxide nanoparticles (<100 nm) were acquired using the same scanning conditions applied for magnetite nanoparticles. The obtained XRD pattern, as shown in Figure 7.12 showed a 94 % match with JCPDS 75-0078 reference card. The sample showed a=b=4.41 Å c=2.91 Å unit cell parameters, corresponding to a tetragonal system. The space group of the sample was found to be P42/mnm (136), confirming its rutile form crystallization structure. In this configuration, at room temperature, Cr occupies the 2a positions and oxygen the 4f, building an octahedral coordination geometry. Moreover, the expected and measured density of the sample are respectively 4.928 and 4.8 g/cm^3.

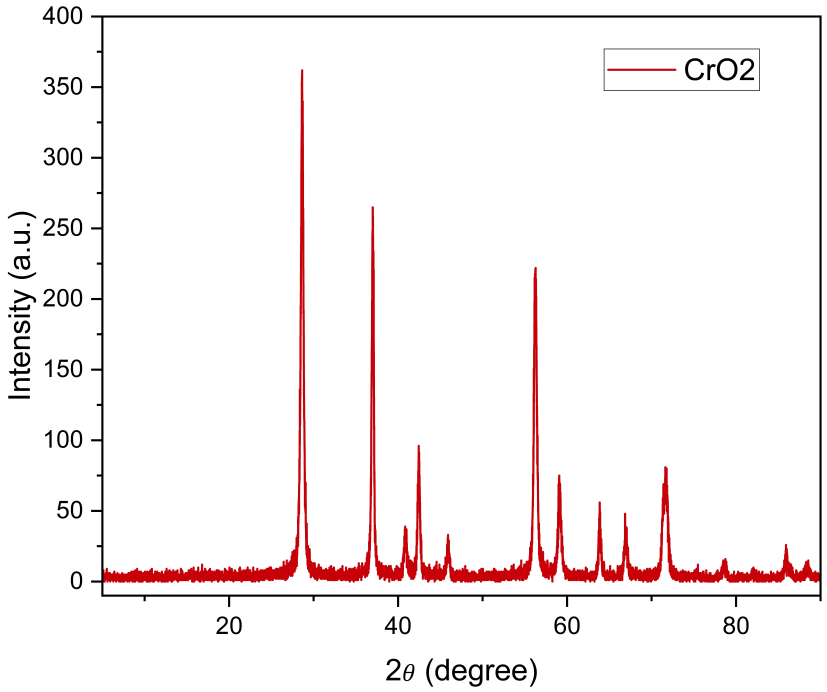

Figure 7.12: XRD graphs obtained for chromium dioxide nanoparticles

The characteristic peaks for eighteen crystalline planes of chromium dioxide were identified by

Diffrac.EVA software from Bruker (Billerica, USA). Below, in Table 7.12, interplanar spacings (d) and scattering angles (2θ) from card JCPDS 75-0078 standard data are reported and compared with data measured from the acquired XRD pattern. The anticipated CrO2 crystalline structure is found.

Locations of crystallinity peaks are found to be in good accordance with standard reported data. No significant effects deriving from the presence of impurities or high strains in the lattice can be observed.

Moreover, some observations on the intensity of the peaks can be formulated.
High and sharp peaks, as can be seen in Figure 7.12, suggest the presence of a strong diffraction signal. This allows to confirm the presence of a distributed and well defined crystalline structure. Finally, the calculated crystallite size for this nanopowder is 19.49 nm.

Table 7.12: Diffraction peaks from XRD data of CrO2 (Miller indices, interplanar spacings and scattering angles)

	Standard data		**Measured data**	
hkl	**d (Å)**	2θ **(°)**	**d (Å)**	2θ **(°)**
110	3.118	28.603	3.110	28.680
101	2.429	36.981	2.427	37.011
200	2.205	40.894	2.199	41.007
111	2.128	42.454	2.125	42.509
210	1.972	45.981	1.967	46.109
211	1.633	56.306	1.630	56.417
220	1.559	59.214	1.555	59.386
002	1.455	63.932	1.455	63.932
310	1.395	67.058	1.391	67.259
221	1.374	68.180	1.372	68.339
112	1.319	71.495	1.318	71.533
301	1.312	71.900	1.309	72.075
311	1.258	75.543	1.255	75.733
320	1.223	78.069	1.220	78.314
202	1.214	78.735	1.213	78.810
212	1.171	82.280	1.170	82.373
321	1.128	86.182	1.125	86.422
400	1.103	88.643	1.100	88.939

7.3.4. Discussion

Magnetic properties of Chromium Dioxide showed some interesting features. Even though the found retentivity and coercivity have low and almost negligible values, the hysteresis loop area presented two "lobes". Explanation to this behaviour was found to be linked to its atomic configuration and response to the applied sinusoidal field.
The "pinched" hysteresis loop is typical of mem-systems, i.e. materials used for memory storage. A similar behaviour is also shown by TiO_2, another memristor used in data storage of computers, which presents the same rutile crystallographic structure of CrO_2 [13].
In the context of this research, both saturation magnetization (28.99 emu/g) and Curie temperature (113.85 C) of CrO_2 were found to be much lower than the values found for magnetite and nickel nanoparticles, suggesting lower heat release capabilities of CrO_2.
This confirms what was found via MagneTherm induction tests, which indicated overall poor heating performance of this material even at the highest applied field strength and frequency.

7.4. Nickel-Zinc Ferrite nanopowder

This section presents results and characterization data obtained from tests performed on Ni-Zn ferrite ($NiZnFe_4O_4$) nanopowder.
Thermogravimetric experiments were performed to study the Curie temperature of the material. Furthermore, results from SQUID measurements are reported and explained to interpret the heat generation capabilities of Ni-Zn ferrite powder shown previously in section 6.1.

7.4.1. Thermogravimetric Analysis

Thermogravimetric analysis of Ni-Zn ferrite samples was conducted, following the procedure described in section subsection 5.2.3. In this case, a heating rate of 5 ° C / min was chosen, in order to reduce any possible kinetic effect of reactions and transitions.
Data was acquired and manipulated. Analysis of gravimetric points (acquired as absolute mass data) was performed by calculating how the mass of the sample is affected in relation to the initial sample mass.

The graph of relative mass (m %) plotted against temperature is reported below in Figure 7.13.

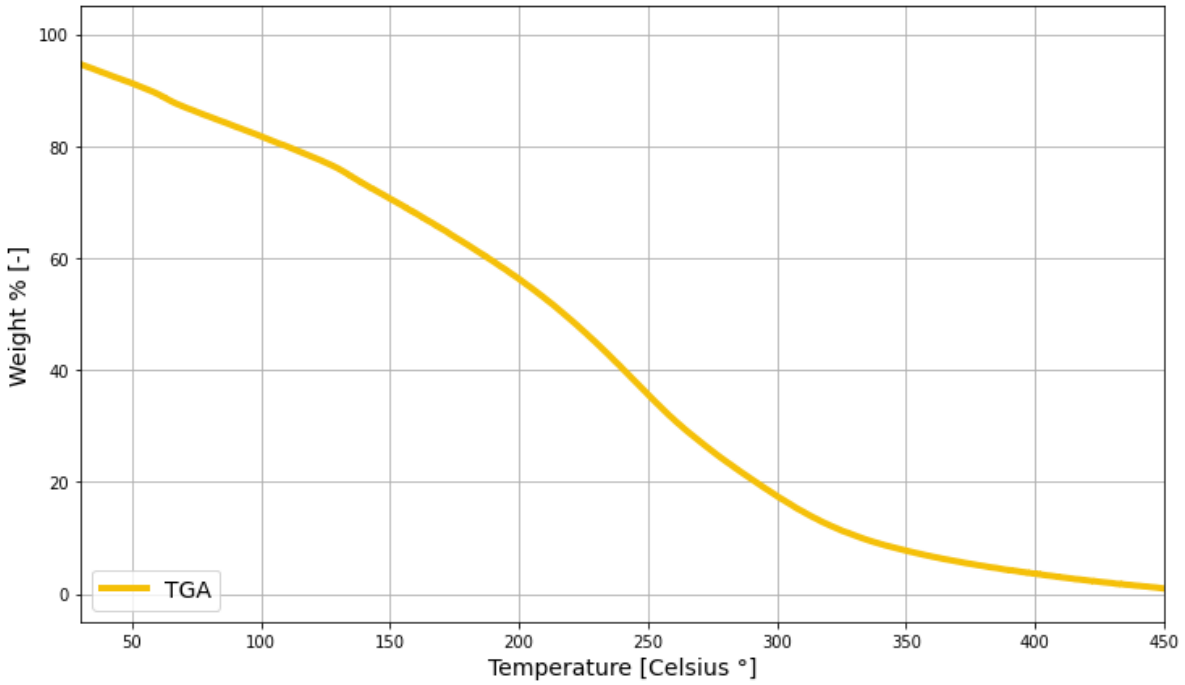

Figure 7.13: TGA of Ni-Zn Ferrite nanopowder with applied magnetic field

From significant values of TGA parameters, reported below in Table 7.13, a relative mass loss of 10.3 % was found.
In this case, the curve offset was not clearly visible. This identifies a more gradual transition of the powder from its ferromagnetic to its paramagnetic behaviour. Curie temperature was found to be 306.86° C, slightly lower than the Nickel powder one.

Table 7.13: Summary of thermomagnetic data from TGA measurements of Ni-Zn ferrite nanopowder

TGA parameter	Value
Initial mass [mg]	9.31
Delta m [mg]	0.96
DTGA peak [°C]	239.22
Tc from offset [°C]	306.86±2.56

7.4.2. SQUID

Magnetic properties of the Ni-Zn ferrite nanopowder were studied by measurements conducted via SQUID equipment. A SQUID machine (Superconducting Quantum Interference Device), as explained in subsection 5.2.4, was used to perform measurements at room temperature (300 K) in the -1 to 1 T range.
The magnetization curve of $NiZnFe_4O_4$ from SQUID is given in Figure 7.14. All relevant parameters are then extrapolated and reported in Table 7.14.

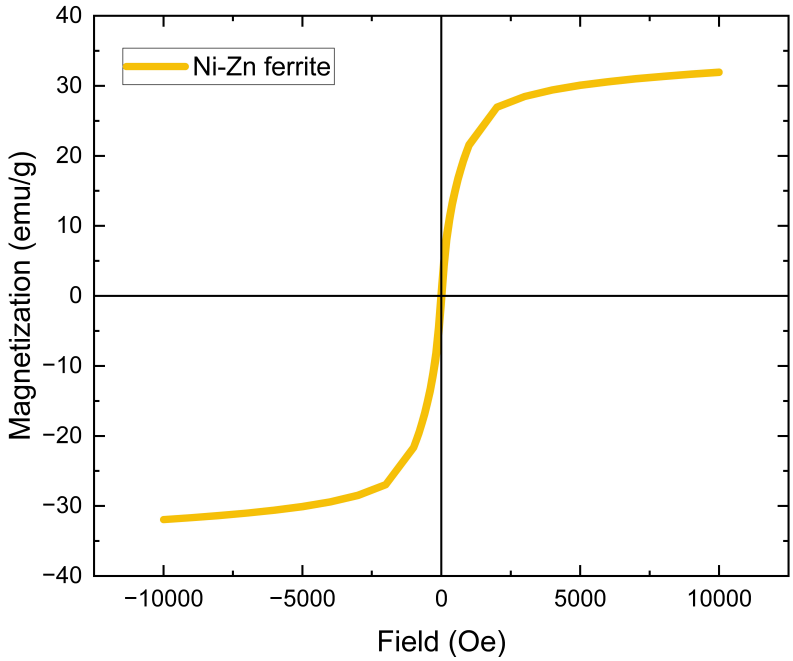

Figure 7.14: Magnetization curve of Ni-Zn ferrite nanopowder obtained from SQUID equipment

Table 7.14: Magnetic properties of Ni-Zn ferrite nanopowder from SQUID measurement

Hysteresis loop parameter	Value
Sample mass [mg]	1.47
Coercivity [Oe]	14.94
Saturation magnetization [emu/g]	31.93
Retentivity [emu/g]	0.78

8

Conclusion and recommendations

The aerospace industry is currently prioritizing sustainability by focusing on reducing aircraft weight and developing environmentally friendly materials. This shift has led to the increasing adoption of polymers and polymer composites over metal alloys for structural components. Thermoplastic polymers, in particular, have gained interest due to their recyclability, reshaping, and remolding capabilities. However, joining thermoplastic composites presents challenges related to weight, design, processing, risks, and cost-effectiveness. Fusion bonding, or fusion welding, is expected to replace traditional joining techniques such as mechanical fastening and adhesive bonding in the near future. Among fusion bonding methods, induction welding is especially promising due to its non-contact nature and potential for continuous processing. Conventional induction welding relies on metal mesh or carbon fibers as susceptors to convert electromagnetic energy into heat. However, these materials can cause non-uniform heating and reduce mechanical properties. Magnetic nanoparticles (MNPs) offer a potential solution as minimally invasive conductive susceptors. Originally explored in the biomedical field for cancer treatment via targeted hyperthermia, MNPs generate heat through hysteresis losses when subjected to an alternating magnetic field (AMF). Their ability to heat polymers above their melting temperatures makes them viable candidates for induction welding. A critical challenge in this process is preventing thermoplastic degradation due to overheating. To address this, recent studies have proposed selecting susceptors with Curie temperatures compatible with the processing temperatures of thermoplastic polymers, enabling precise temperature control and self-regulation during welding.

This research has investigated the heating capabilities of various magnetic nanoparticles and their potential as self-regulating susceptors for induction welding of thermoplastic materials. This thesis will hopefully contribute to the development of the new generation of fusion bonding techniques. This chapter provides a summary of the key results of this study, a discussion of their implications, and some recommendations for future research steps.

The main goal of this research project was to evaluate the heating behaviour and efficiency of magnetic nanoparticles and to correlate this data with their magnetic and morphological properties. In order to pursue these objectives, an extensive calorimetric study has been performed by using an induction heating equipment (MagneTherm) provided by Nanotherics. Five selected nanoparticles have been tested: magnetite (Fe_3O_4), Nickel (Ni), Nickel-Zinc ferrite ($NiZnFe_4O_4$) and Chromium Dioxide (CrO_2).
As can be seen below in Figure 8.1 (reproduced from section 6.1), magnetite showed the best heating efficiency, followed by Nickel and Nickel-Zinc ferrite. Chromium dioxide showed poor

heating capabilities in all the performed tests.

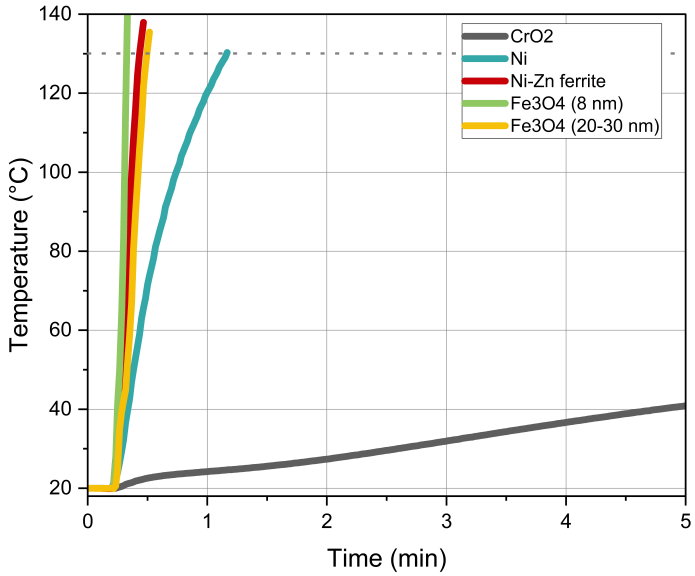

Figure 8.1: Temperature vs. time plot of MagneTherm tests performed on 50 mg of various nanoparticles types, 8-16 mT, 992 kHz. The graph shows a 10 seconds recording before exposure to AMF, followed by a 5 minute exposure.

Additional tests have been performed to evaluate the effect of chosen frequency and amplitude of the alternating magnetic field on the heating of MNPs. For these tests only magnetite nanoparticles have been taken into consideration.
It was proven that for MNPs in their superparamagnetic size range relaxation heating increases directly with higher values of frequency, according to the Linear Response Theory.
However, when the effect of field strength was studied, it was found the Linear Response Theory holds true only for field values up to 2 kA/m, in the case of 20-30 nm magnetite. As a consequence, while the quadratic relation of power generation with field amplitude ($SLP \propto H^2$) can be applied to 8 nm magnetite nanoparticles, it is not the proper model for the tested case. Therefore, it is suggested to better investigate the Rayleigh model ($SLP \propto H^3$) in order to be able to understand this behaviour.

Finally, by studying the effect of magnetic nanoparticles concentration on heat generation, it seems that an optimal concentration exists. It was found that magnetite in both 8 and 20-30 nm size ranges showed a peak in heat generation for a 10-20 mg/mL concentration in the suspension, indicating a possible optimal window where interparticle interactions are limited. These observations can be particularly significant in the case of a future application of MNPs as susceptors for welding of polymers. The embedding of nanoparticles in the polymer itself or in polymer film will require further investigation on the effects of concentrations. A distribution of MNPs in a solid polymer can potentially show similar effects as a too densely concentrated suspension (as it was found for concentrations above 20 mg/mL).

All the experiments conducted by MagneTherm brought to the light two main obstacles. Firstly, precise knowledge of dispersity, size and shape of the considered nanoparticles is necessary to obtain reliable research outcomes. Therefore, it is essential for future projects to perform extensive morphology assessments via TEM to gain knowledge on these aspects. It has been verified that commercial nanoparticles, as the ones used for this project, are not good candidates for MNPs studies, as there is no possibility for tuning of their properties and often available information is limited. Therefore, it is recommended to synthesize particles in-house for future studies on similar topics.

Secondly, it was found that all measurements obtained via MagneTherm are strongly affected by heat losses. It has been mentioned that the building and existence of a fully adiabatic setup is not straightforward, however, taking into consideration and modeling all the thermodynamic interactions has been proven to be as cumbersome. Therefore, it is recommended to alter the testing equipment in order to obtain more reliable measurements. The insulation system should be improved in order to limit both heat losses from the sample due to air convection and heat gains from external heat sources, such as the induction coil. Finally, additional development of a finite element model of the system could significantly improve the understanding and analysis of heat dissipation and heat generation effects.

In the second part of this research project, characterization of magnetic nanoparticles was performed in order to understand and justify their heat generation capabilities. Magnetic properties of all magnetic nanoparticles were measured via SQUID. Summary of this is shown below in Figure 8.2 and Figure 8.3.

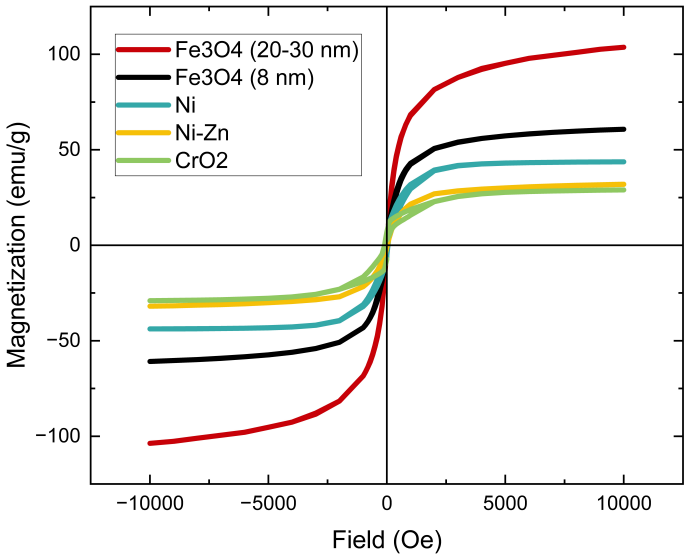

Figure 8.2: SQUID magnetization curves of all magnetic nanopowders used in this research

The analysis of magnetic results confirms a close correlation between saturation magnetization and heating capabilities of the nanoparticles, following the model provided by Linear Response Theory. Overall, Chromium Dioxide nanopowder did not show impressive magnetic properties, confirming the cause of its poor heating capabilities. On the other end of the spectrum, magnetite always showed superior heating capabilities and magnetization values. However, high Curie temperatures of Fe_3O_4 make them unsuitable to realize self-regulating MNP susceptors for thermoplastics.

Aim of this thesis was not only to understand the applicability and limitations of magnetic nanoparticles, but also to find reliable procedures to test them. The collected data proved that thermogravimetric analysis (TGA) can be used as a reliable method to find the Curie temperature of materials. Good accordance was found between values reported in literature and the ferromagnetic-paramagnetic transitions for tested nanopowders.
In addition, an interesting observation can be made on the graphs obtained from TGA. It can be speculated that a correlation between the relative mass loss and the magnetization of tested nanoparticles exists. As it can be seen below in Figure 8.4, all the nanopowder, except Nickel, showed a direct correlation between their magnetization and mass loss from TGA

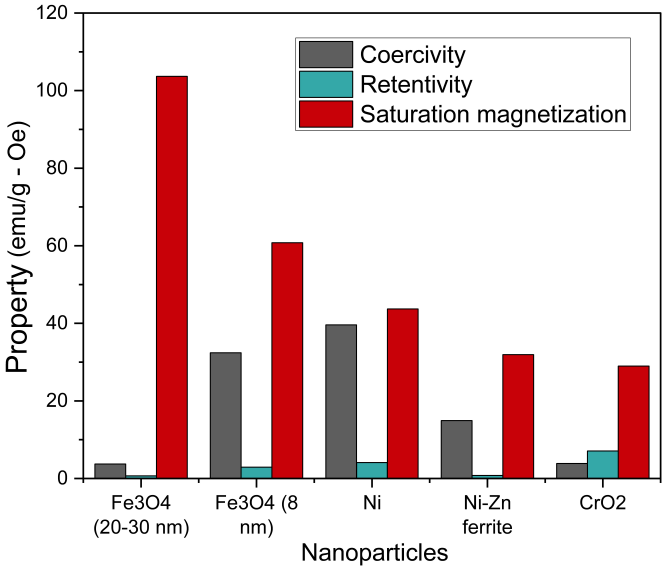

Figure 8.3: Summary of magnetic properties of all magnetic nanopowders used in this research

under applied magnetic field.
This behaviour has not been previously observed in literature and will require further investigation to fully confirm the correlation. In order to do this, it is recommended to perform additional TGA measurements with magnetic nanoparticles of different compositions and to validate the results with Vibrating Sample Magnetometer equipment, which can confirm both values of Curie temperature from TGA and saturation magnetization from SQUID.

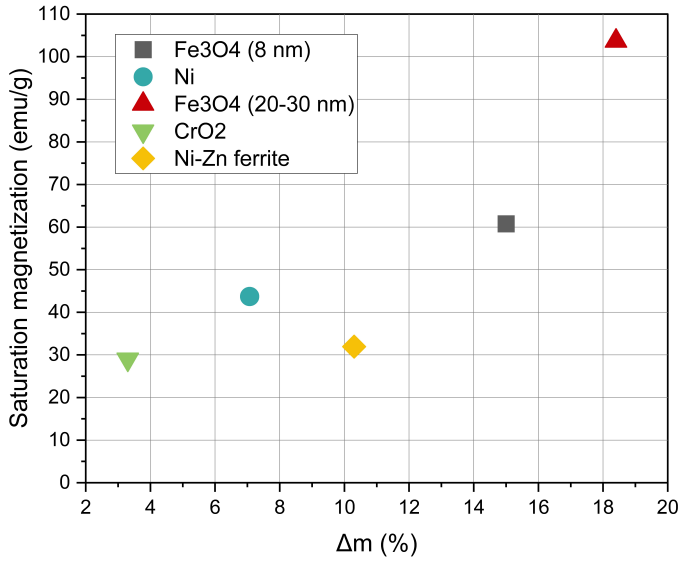

Figure 8.4: Plot correlating saturation magnetization and relative mass loss (ΔM %) from TGA of all magnetic nanopowders used in this research

From TGA experiments, nickel and nickel zinc ferrite powders showed Curie temperatures (respectively 342.61°C and 306.86°C) that fall within the temperature processing window of multiple thermoplastics. This is an encouraging aspect, as it confirms the suitability of these particles for potential self-regulating induction melting of polymers. More specifically, nickel nanoparticles appear to be a good candidate to realize minimally invasive susceptors for

PPS, with a processing window of 310-330°C, and LM-PAEK matrices (330-350°C), previously employed within the research group to test the compounding and embedding of MNPs.
More extensive research should be conducted to confirm the aforementioned aspects of nickel and nickel zinc ferrite nanoparticles. It has been reported that Ni-Zn ferrites can achieve Curie temperatures within the 270-400°C range (Appendix C), making them suitable candidates as magnetic nanoparticles for creating self-regulating susceptors for induction welding of thermoplastics. Therefore, synthesis of Ni-Zn ferrite with various doping contents of Zinc is recommended to achieve proper Curie temperature in the needed temperature range.

In conclusion, optimization of the composition of magnetic nanoparticles and further testing, as well as additional polymer compounding prototypes, will be critical steps to develop future research in the field of thermoplastic welding.

References

[1] *2. Classes of Magnetic Materials | College of Science and Engineering*. en. URL: https://cse.umn.edu/irm/2-classes-magnetic-materials (visited on 08/30/2024).

[2] Majid Abdellahi, Mohammad Tajally, and Omid Mirzaee. "The effect of the particle size on the heating and drug release potential of the magnetic nanoparticles in a novel point of view". In: *Journal of Magnetism and Magnetic Materials* 530 (2021), p. 167938. ISSN: 0304-8853. DOI: https://doi.org/10.1016/j.jmmm.2021.167938. URL: https://www.sciencedirect.com/science/article/pii/S0304885321002146.

[3] T.J. Ahmed et al. "Induction welding of thermoplastic composites—an overview". en. In: *Composites Part A: Applied Science and Manufacturing* 37.10 (Oct. 2006), pp. 1638–1651. ISSN: 1359835X. DOI: 10.1016/j.compositesa.2005.10.009. URL: https://linkinghub.elsevier.com/retrieve/pii/S1359835X05003957 (visited on 09/02/2024).

[4] Rhiannon Anderson and Kristoff Davis. "Polymeric Materials Used in Aerospace Applications". In: (). URL: https://www.hilarispublisher.com/open-access/polymeric-materials-used-in-aerospace-applications-96960.html (visited on 08/28/2024).

[5] *Annales de chimie et de physique*. 1895. URL: https://gallica.bnf.fr/ark:/12148/bpt6k34905r (visited on 08/28/2024).

[6] Alexander Astafyev et al. "Thermomagnetometric analysis of nickel–zinc ferrites". In: *Journal of Thermal Analysis and Calorimetry* 142 (Sept. 2020), pp. 1–7. DOI: 10.1007/s10973-020-10182-3.

[7] Duck Bae et al. "Study on the Heating Behavior of Fe 3 O 4 -Embedded Thermoplastic Polyurethane Adhesive Film via Induction heating: Heating Behavior of Fe3O4-Embedded TPU Adhesive via Induction Heating". In: *Bulletin of the Korean Chemical Society* 37 (July 2016).

[8] DuckHwan Bae et al. "Heating behavior of ferromagnetic Fe particle-embedded thermoplastic polyurethane adhesive film by induction heating". In: *Journal of Industrial and Engineering Chemistry* 30 (Oct. 2015), pp. 92–97. ISSN: 1226-086X. DOI: 10.1016/j.jiec.2015.05.007. URL: https://www.sciencedirect.com/science/article/pii/S1226086X15001641 (visited on 09/02/2024).

[9] Inseok Baek and Seoksoon Lee. "A Study of Films Incorporating Magnetite Nanoparticles as Susceptors for Induction Welding of Carbon Fiber Reinforced Thermoplastic". In: *Materials* 13.2 (Jan. 2020). Number: 2 Publisher: Multidisciplinary Digital Publishing Institute. ISSN: 1996-1944. DOI: 10.3390/ma13020318. URL: https://www.mdpi.com/1996-1944/13/2/318 (visited on 08/31/2024).

[10] Allan Barbosa. "Superparamagnetic Fe3O4 Nanoparticle Based Susceptors For Induction Heating". en. In: *TU Delft Repository* (2022).

[11] Thomas Bayerl, Ralf Schledjewski, and Peter Mitschang. "Induction Heating of Thermoplastic Materials by Particulate Heating Promoters". en. In: *Polymers and Polymer Composites* 20.4 (May 2012), pp. 333–342. ISSN: 0967-3911, 1478-2391. DOI: 10.1177/096739111202000401. URL: http://journals.sagepub.com/doi/10.1177/096739111202000401 (visited on 08/01/2024).

[12] Lisa van den Berg. "Development of 2nd Generation Proteinous Bioplastics". In: (Jan. 2009).

[13] Dalibor Biolek et al. "Computing areas of pinched hysteresis loops of mem-systems in OrCAD PSPICE". In: *Applied Mechanics and Materials* 278 (Mar. 2013), pp. 1081–1090. DOI: 10.4028/www.scientific.net/AMM.278-280.1081.

[14] F. Bødker, S. Mørup, and S. Linderoth. "Surface effects in metallic iron nanoparticles". In: *Physical Review Letters* 72.2 (Jan. 1994). Publisher: American Physical Society, pp. 282–285. DOI: 10.1103/PhysRevLett.72.282. URL: https://link.aps.org/doi/10.1103/PhysRevLett.72.282 (visited on 08/01/2024).

[15] Oscar Bomatí-Miguel et al. "Magnetic nanoparticles prepared by laser-induced pyrolysis". In: (Jan. 2002). DOI: 10.1109/INTMAG.2002.1001479.

[16] M. Cobianchi et al. "Experimental determination of the frequency and field dependence of Specific Loss Power in Magnetic Fluid Hyperthermia". In: *Journal of Magnetism and Magnetic Materials* 444 (2017), pp. 154–160. ISSN: 0304-8853. DOI: https://doi.org/10.1016/j.jmmm.2017.08.014. URL: https://www.sciencedirect.com/science/article/pii/S0304885317320577.

[17] John F. Cochran and Bretislav V. Heinrich. *6.1: Introduction to Ferromagnetism*. Mar. 2020. URL: https://phys.libretexts.org/Bookshelves/Electricity_and_Magnetism/Book%3A_Applications_of_Maxwells_Equations_(Cochran_and_Heinrich)/06%3A_Ferromagnetism/6.01%3A_Introduction (visited on 08/28/2024).

[18] J. M. D. Coey and Stuart S.P. Parkin, eds. *Handbook of Magnetism and Magnetic Materials*. en. Cham: Springer International Publishing, 2021. ISBN: 978-3-030-63208-3 978-3-030-63210-6. URL: https://link.springer.com/10.1007/978-3-030-63210-6 (visited on 08/27/2024).

[19] *CrO2 nanoparticles prepared via oxidation method*. July 2012. URL: http://english.ipe.cas.cn/Newsroom/ResearchNews/202103/t20210303_264692.html (visited on 02/01/2025).

[20] *Curie temperature*. en. June 2024. URL: https://en.wikipedia.org/w/index.php?title=Curie_temperature&oldid=1229210052 (visited on 08/29/2024).

[21] Cindi Dennis and Robert Ivkov. "Physics of heat generation using magnetic nanoparticles for hyperthermia". In: *International journal of hyperthermia : the official journal of European Society for Hyperthermic Oncology, North American Hyperthermia Group* 29 (Oct. 2013). DOI: 10.3109/02656736.2013.836758.

[22] Cindi L. Dennis and Robert Ivkov. "Physics of heat generation using magnetic nanoparticles for hyperthermia". In: *International Journal of Hyperthermia* 29.8 (Dec. 2013), pp. 715–729. ISSN: 0265-6736, 1464-5157. DOI: 10.3109/02656736.2013.836758. URL: https://www.tandfonline.com/doi/full/10.3109/02656736.2013.836758 (visited on 08/28/2024).

[23] Dnyandevi Deorukhkar. "Synthesis of magnetic nanoparticles for magnetic induction welding". en. In: *TU Delft Repository* (2024).

[24] Silvio Dutz et al. “Hysteresis losses of magnetic nanoparticle powders in the single domain size range”. In: *Journal of Magnetism and Magnetic Materials* 308 (Jan. 2007), pp. 305–312. DOI: 10.1016/j.jmmm.2006.06.005.

[25] P. Eaton et al. “A direct comparison of experimental methods to measure dimensions of synthetic nanoparticles”. In: *Ultramicroscopy* 182 (Nov. 2017), pp. 179–190. ISSN: 0304-3991. DOI: 10.1016/j.ultramic.2017.07.001. URL: https://www.sciencedirect.com/science/article/pii/S0304399116302091 (visited on 08/30/2024).

[26] Remzi Ece, Fahrettin Ozturk, and Merve Çobanoğlu. “Recent advancements in thermoplastic composite materials in aerospace industry”. In: 0(0) (Dec. 2023), pp. 1–33. DOI: 10.1177/08927057231222820.

[27] K. Fabian, V. P. Shcherbakov, and S. A. McEnroe. “Measuring the Curie temperature”. In: *Geochemistry, Geophysics, Geosystems* 14.4 (2013), pp. 947–961. ISSN: 1525-2027. DOI: 10.1029/2012GC004440. URL: https://onlinelibrary.wiley.com/doi/abs/10.1029/2012GC004440 (visited on 08/26/2024).

[28] Rouhollah Dermanaki Farahani, Mathieu Janier, and Martine Dubé. “Conductive films of silver nanoparticles as novel susceptors for induction welding of thermoplastic composites”. In: *Nanotechnology* 29.12 (Feb. 2018). Publisher: IOP Publishing, p. 125701. ISSN: 0957-4484. DOI: 10.1088/1361-6528/aaa93c. URL: https://dx.doi.org/10.1088/1361-6528/aaa93c (visited on 09/01/2024).

[29] Joel R. Fried. *Polymer science and technology*. 3rd ed. Boca Raton, FL, USA: Pearson Education, 2014.

[30] Thomas Girardet et al. “Spinel Magnetic Iron Oxide Nanoparticles: Properties, Synthesis and Washing Methods”. In: *Applied Sciences* 12 (Aug. 2022), p. 8127. DOI: 10.3390/app12168127.

[31] A. González. “1.5 X-Ray Crystallography: Data Collection Strategies and Resources”. In: *Comprehensive Biophysics*. Ed. by Edward H. Egelman. Amsterdam: Elsevier, Jan. 2012. ISBN: 978-0-08-095718-0. DOI: 10.1016/B978-0-12-374920-8.00106-5. URL: https://www.sciencedirect.com/science/article/pii/B9780123749208001065 (visited on 08/30/2024).

[32] Pablo Guardia, Amilcar Labarta, and Xavier Batlle. “Tuning the Size, the Shape, and the Magnetic Properties of Iron Oxide Nanoparticles”. In: *The Journal of Physical Chemistry C* 115.2 (2011), pp. 390–396. DOI: 10.1021/jp1084982.

[33] I.H. Gul, W. Ahmed, and A. Maqsood. “Electrical and magnetic characterization of nanocrystalline Ni–Zn ferrite synthesis by co-precipitation route”. In: *Journal of Magnetism and Magnetic Materials* 320.3 (2008), pp. 270–275. ISSN: 0304-8853. DOI: https://doi.org/10.1016/j.jmmm.2007.05.032. URL: https://www.sciencedirect.com/science/article/pii/S0304885307007470.

[34] Robert Ivkov Hattie L. Ring Anirudh Sharma and John C. Bischof. “The impact of data selection and fitting on SAR estimation for magnetic nanoparticle heating”. In: *International Journal of Hyperthermia* 37.3 (2020), pp. 100–107. DOI: 10.1080/02656736.2020.1810332. URL: https://doi.org/10.1080/02656736.2020.1810332.

[35] W.M. Haynes. *CRC Handbook of Chemistry and Physics*. 95th ed. Boca Raton, FL, USA: CRC Press, 2014.

[36] Rudolf Hergt, Silvio Dutz, and Michael Röder. "Effects of size distribution on hysteresis losses of magnetic nanoparticles for hyperthermia". In: *Journal of Physics: Condensed Matter* 20.38 (Sept. 2008), p. 385214. ISSN: 0953-8984, 1361-648X. DOI: 10.1088/0953-8984/20/38/385214. URL: https://iopscience.iop.org/article/10.1088/0953-8984/20/38/385214 (visited on 08/28/2024).

[37] *IR Spectroscopy and FTIR Spectroscopy: How an FTIR Spectrometer Works and FTIR Analysis*. en. URL: http://www.technologynetworks.com/analysis/articles/ir-spectroscopy-and-ftir-spectroscopy-how-an-ftir-spectrometer-works-and-ftir-analysis-363938 (visited on 08/30/2024).

[38] Santosh Jadhav et al. "Effect of Cation Proportion on the Structural and Magnetic Properties of Ni-Zn Ferrites Nano-Size Particles Prepared By Co-Precipitation Technique". In: *Chinese J. Chemical Physics* 21 (Aug. 2008), p. 381. DOI: 10.1088/1674-0068/21/04/381-386.

[39] Jeffrey A. Jansen. *The Importance of Crystallinity in Plastics Performance*. Jan. 2023. URL: https://madisongroup.com/the-importance-of-crystallinity-in-plastics-performance/ (visited on 08/30/2024).

[40] D. Jiles. *Introduction to magnetism and magnetic materials*. 2nded. London, UK: CRC Press, 1991.

[41] Seema Joshi et al. "Structural, magnetic, dielectric and optical properties of nickel ferrite nanoparticles synthesized by co-precipitation method". In: *Journal of Molecular Structure* 1076 (2014), pp. 55–62. ISSN: 0022-2860. DOI: https://doi.org/10.1016/j.molstruc.2014.07.048. URL: https://www.sciencedirect.com/science/article/pii/S0022286014007844.

[42] Mehran Kardar. *Statistical physics of particles*. eng. Cambridge: Cambridge University Press, 2007. ISBN: 978-0-521-87342-0.

[43] Hyung Kim and Sunghyun Yoon. "Frequency Dependence of Initial Heat Generation in Granular Magnetite Nanoparticles". In: *Journal of the Korean Physical Society* 77 (Aug. 2020), pp. 293–297. DOI: 10.3938/jkps.77.293.

[44] Diana Kostyukova and Yong Hee Chung. "Synthesis of Iron Oxide Nanoparticles Using Isobutanol". In: *Journal of Nanomaterials* 2016.1 (2016). _eprint: https://onlinelibrary.wiley.com/doi/pdf/ p. 4982675. ISSN: 1687-4129. DOI: 10.1155/2016/4982675. URL: https://onlinelibrary.wiley.com/doi/abs/10.1155/2016/4982675 (visited on 08/30/2024).

[45] S. Kumar et al. "Structural and Magnetic Properties of Copper-Substituted Nickel–Zinc Nanoparticles Prepared by Sol-Gel Method". In: *Journal of Superconductivity and Novel Magnetism* 33 (Mar. 2020), pp. 1–13. DOI: 10.1007/s10948-019-05407-y.

[46] Sanjeev Kumar et al. "Synthesis, characterization and magnetic properties of monodisperse Ni, Zn-ferrite nanocrystals". In: *Journal of Magnetism and Magnetic Materials* 379 (2015), pp. 50–57. ISSN: 0304-8853. DOI: https://doi.org/10.1016/j.jmmm.2014.12.006. URL: https://www.sciencedirect.com/science/article/pii/S0304885314012086.

[47] Yongsung Kwon, Duckhwan Bae, and MinYoung Shon. "Comparison of Heating Behavior of Various Susceptor-embedded Thermoplastic Polyurethane Adhesive Films via Induction Heating". In: *Composites Research* 30.3 (2017). Publisher: The Korean Society for Composite Materials, pp. 181–187. ISSN: 2288-2103. DOI: 10.7234/composres.2017.30.3.181. URL: https://koreascience.kr/article/JAKO201720861203995.page (visited on 09/01/2024).

[48] Xabier Lasheras et al. “Chemical Synthesis and Magnetic Properties of Monodisperse Nickel Ferrite Nanoparticles for Biomedical Applications”. In: *The Journal of Physical Chemistry C* 120 (Jan. 2016). DOI: 10.1021/acs.jpcc.5b10216.

[49] Bernard Legendre and M. Sghaier. “Curie temperature of nickel”. In: *Journal of Thermal Analysis and Calorimetry - J THERM ANAL CALORIM* 105 (July 2011), pp. 141–143. DOI: 10.1007/s10973-011-1448-2.

[50] O. M. Lemine et al. “Assessing the Heat Generation and Self-Heating Mechanism of Superparamagnetic Fe3O4 Nanoparticles for Magnetic Hyperthermia Application: The Effects of Concentration, Frequency, and Magnetic Field”. In: *Nanomaterials* 13.3 (2023). ISSN: 2079-4991. URL: https://www.mdpi.com/2079-4991/13/3/453.

[51] Qing Li et al. “Correlation between particle size/domain structure and magnetic properties of highly crystalline Fe3O4 nanoparticles”. In: *Scientific Reports* 7 (Dec. 2017). DOI: 10.1038/s41598-017-09897-5.

[52] Zimin Li et al. “Mechanism and kinetics of magnetite oxidation under hydrothermal conditions”. In: *RSC Advances* 9 (Oct. 2019), pp. 33633–33642. DOI: 10.1039/C9RA03234G.

[53] Taegyu Lm et al. “Heating behavior and adhesion performance of induction-heated multilayered thermoplastic polyurethane adhesive film”. In: *The Journal of Adhesion* 96 (Jan. 2019), pp. 1–12. DOI: 10.1080/00218464.2019.1565757.

[54] K. Maaz et al. “Synthesis and magnetic characterization of nickel ferrite nanoparticles prepared by co-precipitation route”. In: *Journal of Magnetism and Magnetic Materials* 321.12 (2009), pp. 1838–1842. ISSN: 0304-8853. DOI: https://doi.org/10.1016/j.jmmm.2008.11.098. URL: https://www.sciencedirect.com/science/article/pii/S0304885308012535.

[55] *Magnetic Properties of Materials*. en. URL: https://www.sigmaaldrich.com/NL/en/technical-documents/technical-article/materials-science-and-engineering/solid-state-synthesis/properties (visited on 08/30/2024).

[56] Sara Majetich, Tianlong Wen, and Olin Mefford. “Magnetic Nanoparticles”. In: *MRS bulletin / Materials Research Society* 38 (Nov. 2013), pp. 899–903. DOI: 10.1557/mrs.2013.230.

[57] P. K. Mallick. *Processing of polymer matrix composites*. 1st ed. Boca Raton, FL, USA: CRC Press, 2017.

[58] Romain Martin et al. “Material Selection Methodology for an Induction Welding Magnetic Susceptor Based on Hysteresis Losses”. In: *Advanced Engineering Materials* 24 (Oct. 2021). DOI: 10.1002/adem.202100877.

[59] Elsa M. Materón et al. “Magnetic nanoparticles in biomedical applications: A review”. In: *Applied Surface Science Advances* 6 (2021), p. 100163. ISSN: 2666-5239. DOI: https://doi.org/10.1016/j.apsadv.2021.100163. URL: https://www.sciencedirect.com/science/article/pii/S2666523921001094.

[60] Jennifer Mathias. *How Does FTIR Analysis Work?* Dec. 2022. URL: https://www.innovatechlabs.com/newsroom/672/stuff-works-ftir-analysis/ (visited on 08/30/2024).

[61] Karrina McNamara and Syed A. M. Tofail. “Nanoparticles in biomedical applications”. In: *Advances in Physics: X* 2.1 (2017), pp. 54–88. DOI: 10.1080/23746149.2016.1254570. URL: https://doi.org/10.1080/23746149.2016.1254570.

[62] R. Mohr et al. “Initiation of shape-memory effect by inductive heating of magnetic nanoparticles in thermoplastic polymers”. In: *Proceedings of the National Academy of Sciences* 103 (Mar. 2006). Publisher: Proceedings of the National Academy of Sciences, pp. 3540–3545. DOI: 10.1073/pnas.0600079103. URL: https://www.pnas.org/doi/full/10.1073/pnas.0600079103 (visited on 09/02/2024).

[63] Allan H. Morrish. “The Magnetic Field”. In: *The Physical Principles of Magnetism*. 2001, pp. 1–30. DOI: 10.1109/9780470546581.ch1.

[64] Sam Mugiraneza and Alannah M. Hallas. “Tutorial: a beginner’s guide to interpreting magnetic susceptibility data with the Curie-Weiss law”. In: *Communications Physics* 5.1 (Apr. 2022), p. 95. ISSN: 2399-3650. DOI: 10.1038/s42005-022-00853-y. URL: https://doi.org/10.1038/s42005-022-00853-y.

[65] Kritika N. and Indrajit R. “Therapeutic applications of magnetic nanoparticles: recent advances”. In: *Materials Advances* 3 (Aug. 2022). DOI: 10.1039/D2MA00444E.

[66] G. Nabiyouni et al. “Characterization and Magnetic Properties of Nickel Ferrite Nanoparticles Prepared by Ball Milling Technique”. In: *Chinese Physics Letters* 27.12 (Dec. 2010), p. 126401. DOI: 10.1088/0256-307X/27/12/126401. URL: https://dx.doi.org/10.1088/0256-307X/27/12/126401.

[67] Venkatesha Narayanaswamy et al. “Role of Magnetite Nanoparticles Size and Concentration on Hyperthermia under Various Field Frequencies and Strengths”. In: *Molecules* 26 (Feb. 2021), p. 796. DOI: 10.3390/molecules26040796.

[68] Gouri Nayanar. “Mesoscale Alignment of Discontinuous Composites with Nanoscale Magnetic Particles”. en. In: *TU Delft Repository* (2021).

[69] S. Nepijko and Roland Wiesendanger. “Size Dependence of the Curie Temperature of Separate Nickel Particles Studied by Interference Electron Microscopy”. In: *EPL (Europhysics Letters)* 31 (July 2007), p. 567. DOI: 10.1209/0295-5075/31/9/011.

[70] Aleksey A. Nikitin et al. “Magneto-Mechanical Approach in Biomedicine: Benefits, Challenges, and Future Perspectives”. In: *International Journal of Molecular Sciences* 23.19 (2022). ISSN: 1422-0067. DOI: 10.3390/ijms231911134. URL: https://www.mdpi.com/1422-0067/23/19/11134.

[71] Gopal Niraula et al. “The Curie temperature: a key playmaker in self-regulated temperature hyperthermia”. In: *Journal of Materials Chemistry B* 12.2 (2024), pp. 286–331. ISSN: 2050-750X, 2050-7518. DOI: 10.1039/D3TB01437A. URL: https://xlink.rsc.org/?DOI=D3TB01437A (visited on 08/29/2024).

[72] *Nondestructive Evaluation Physics: Magnetism*. URL: https://www.nde-ed.org/Physics/Magnetism/twoends.xhtml (visited on 08/30/2024).

[73] S.D. Norem, M.J. O’Neill, and A.P. Gray. “The use of magnetic transitions in temperature calibration and performance evaluation of thermogravimetric systems”. In: *Thermochimica Acta* 1.1 (1970), pp. 29–38. ISSN: 0040-6031. DOI: https://doi.org/10.1016/0040-6031(70)85026-2. URL: https://www.sciencedirect.com/science/article/pii/0040603170850262.

[74] NPTEL. *Introduction:History and overview of spin electronics, Classes of magnetic materials*. URL: https://archive.nptel.ac.in/content/storage2/courses/115103039/module1/lec1/1.html (visited on 08/19/2024).

[75] Wei-ping Pan, Weibing Xu, and Sen Li. *Fundamentals of TGA and SDT*. 2005. URL: https://api.semanticscholar.org/CorpusID:53897876.

[76] Carolyn Pearce, Richard Pattrick, and David Vaughan. "Electrical and Magnetic Properties of Sulfides". In: *Reviews in Mineralogy and Geochemistry* 61 (Jan. 2006). DOI: 10.2138/rmg.2006.61.3.

[77] Carolyn Pearce, Richard Pattrick, and David Vaughan. "Electrical and magnetic properties of sulfides". In: *Reviews in Mineralogy and Geochemistry* 61 (Jan. 2006). DOI: 10.2138/rmg.2006.61.3.

[78] PerkinElmer. "TGA 8000 Temperature Performance - Technical note". In: *Materials Advances* (2016).

[79] Curbell Plastics. *HDPE: Durable, versatile, low cost, abrasion and chemically resistant plastic material*. 2024. URL: https://www.curbellplastics.com/materials/plastics/hdpe/?srsltid=AfmBOoo_z-lEZuVcyztwDxg-GSorHTKv5Iz7LUSSI_db_4XYhw0nPZhq (visited on 08/26/2024).

[80] E. Rafatmah and B. Hemmateenejad. *Metal nanoparticles for sensing applications - ScienceDirect*. URL: https://www.sciencedirect.com/science/article/pii/B9780323884310000193 (visited on 08/30/2024).

[81] Izaz Raouf et al. "A review on numerical modeling for magnetic nanoparticle hyperthermia: Progress and challenges". In: *Journal of Thermal Biology* 91 (June 2020), p. 102644. DOI: 10.1016/j.jtherbio.2020.102644.

[82] R.E. Rosensweig. "Heating magnetic fluid with alternating magnetic field". In: *Journal of Magnetism and Magnetic Materials* 252 (2002). Proceedings of the 9th International Conference on Magnetic Fluids, pp. 370–374. ISSN: 0304-8853. DOI: https://doi.org/10.1016/S0304-8853(02)00706-0. URL: https://www.sciencedirect.com/science/article/pii/S0304885302007060.

[83] Sarah E. Sandler, Benjamin Fellows, and O. Thompson Mefford. "Best Practices for Characterization of Magnetic Nanoparticles for Biomedical Applications". In: *Analytical Chemistry* 91.22 (Nov. 2019). Publisher: American Chemical Society, pp. 14159–14169. ISSN: 0003-2700. DOI: 10.1021/acs.analchem.9b03518. URL: https://doi.org/10.1021/acs.analchem.9b03518 (visited on 08/30/2024).

[84] Jose Schwerdt et al. "Magnetic Field-Assisted Gene Delivery: Achievements and Therapeutic Potential". In: *Current gene therapy* 12 (Feb. 2012), pp. 116–26. DOI: 10.2174/156652312800099616.

[85] Lili Sha et al. "Experimental investigation on the convective heat transfer of Fe3O4/water nanofluids under constant magnetic field". In: *Applied Thermal Engineering* 113 (2017), pp. 566–574. ISSN: 1359-4311. DOI: https://doi.org/10.1016/j.applthermaleng.2016.11.060. URL: https://www.sciencedirect.com/science/article/pii/S1359431116331362.

[86] T.J. Shinde, A.B. Gadkari, and P.N. Vasambekar. "Magnetic properties and cation distribution study of nanocrystalline Ni–Zn ferrites". In: *Journal of Magnetism and Magnetic Materials* 333 (2013), pp. 152–155. ISSN: 0304-8853. DOI: https://doi.org/10.1016/j.jmmm.2012.12.049. URL: https://www.sciencedirect.com/science/article/pii/S0304885312010359.

[87] E. Spain and A. Venkatanarayanan. "13.02 - Review of Physical Principles of Sensing and Types of Sensing Materials". In: *Comprehensive Materials Processing*. Ed. by Saleem Hashmi et al. Oxford: Elsevier, Jan. 2014, pp. 5–46. ISBN: 978-0-08-096533-8. DOI: 10.1016/B978-0-08-096532-1.01302-9. URL: https://www.sciencedirect.com/science/article/pii/B9780080965321013029 (visited on 08/30/2024).

[88] Ch. Srinivas et al. "Effect of Ni2+ substitution on structural and magnetic properties of Ni–Zn ferrite nanoparticles". In: *Journal of Magnetism and Magnetic Materials* 382 (2015), pp. 15–19. ISSN: 0304-8853. DOI: https://doi.org/10.1016/j.jmmm.2015.01.008. URL: https://www.sciencedirect.com/science/article/pii/S0304885315000104.

[89] Vijay K. Stokes. "Joining methods for plastics and plastic composites: an overview". In: *Polymer Engineering and Science* 29 (1989), pp. 1310–1324. URL: https://api.semanticscholar.org/CorpusID:136960376.

[90] W. Suwanwatana, S. Yarlagadda, and J. W. Gillespie. "Hysteresis heating based induction bonding of thermoplastic composites". In: *Composites Science and Technology* 66.11 (Sept. 2006), pp. 1713–1723. ISSN: 0266-3538. DOI: 10.1016/j.compscitech.2005.11.009. URL: https://www.sciencedirect.com/science/article/pii/S0266353805004173 (visited on 09/01/2024).

[91] W. Suwanwatana, S. Yarlagadda, and J. W. Gillespie. "Influence of particle size on hysteresis heating behavior of nickel particulate polymer films". In: *Composites Science and Technology* 66.15 (Dec. 2006), pp. 2825–2836. ISSN: 0266-3538. DOI: 10.1016/j.compscitech.2006.02.033. URL: https://www.sciencedirect.com/science/article/pii/S0266353806001035 (visited on 09/01/2024).

[92] Maria Cristina Tanzi, Silvia Farè, and Gabriele Candiani. "Chapter 7 - Techniques of Analysis". In: *Foundations of Biomaterials Engineering*. Ed. by Maria Cristina Tanzi, Silvia Farè, and Gabriele Candiani. Academic Press, 2019, pp. 393–469. ISBN: 978-0-08-101034-1. DOI: https://doi.org/10.1016/B978-0-08-101034-1.00007-4. URL: https://www.sciencedirect.com/science/article/pii/B9780081010341000074.

[93] *The History of Aviation Materials*. July 2019. URL: https://aipprecision.com/the-history-of-aviation-materials/ (visited on 08/28/2024).

[94] Loi Tonthat et al. "Thermosensitive Ferromagnetic Implant for Hyperthermia Using a Mixture of Magnetic Micro-/Nanoparticles". In: *IEEE Transactions on Magnetics* 54 (2018), pp. 1–6. URL: https://api.semanticscholar.org/CorpusID:49353504.

[95] A.I. Tovstolytkin et al. "Nickel-zinc spinel nanoferrites: Magnetic characterization and prospects of the use in self-controlled magnetic hyperthermia". In: *Journal of Magnetism and Magnetic Materials* 473 (2019), pp. 422–427. ISSN: 0304-8853. DOI: https://doi.org/10.1016/j.jmmm.2018.10.075. URL: https://www.sciencedirect.com/science/article/pii/S0304885318328440.

[96] A. Tufaile, B. Tufaile, and A. Tufaile. "Hysteresis Loops, Dynamical Systems and Magneto-Optics". In: *The 13th CHAOS 2020 International Conference* 10 (2020).

[97] G Vallejo-Fernandez et al. "Mechanism of hyperthermia in magnetic nanoparticles". In: *Journal of Physics D: Applied Physics* 46 (July 2013), p. 312001. DOI: 10.1088/0022-3727/46/31/312001.

[98] G. Vallejo-Fernandez and K. O'Grady. "Effect of the distribution of anisotropy constants on hysteresis losses for magnetic hyperthermia applications". In: *Applied Physics Letters* 103.14 (Oct. 2013), p. 142417. ISSN: 0003-6951. DOI: 10.1063/1.4824649. URL: https://doi.org/10.1063/1.4824649.

[99] Denis Vinnik et al. "Ni substitution effect on the structure, magnetization, resistivity and permeability of zinc ferrites". In: *Journal of Materials Chemistry C* 9 (Mar. 2021). DOI: 10.1039/D0TC05692H.

[100] A.E. Virden and K. O'Grady. "Structure and magnetic properties of NiZn ferrite nanoparticles". In: *Journal of Magnetism and Magnetic Materials* 290-291 (2005). Proceedings of the Joint European Magnetic Symposia (JEMS' 04), pp. 868–870. ISSN: 0304-8853. DOI: https://doi.org/10.1016/j.jmmm.2004.11.398. URL: https://www.sciencedirect.com/science/article/pii/S0304885304016683.

[101] Eric D Wetzel and Bruce K Fink. "Feasibility of Magnetic Particle Films for Curie Temperature-Controlled Processingof CorhpositeMaterials". In: (2001). Ed. by Army Research Laboratory.

[102] S. Wijskamp and E. Kramer. *Properties of thermoplastic composites*. Enschede, NL: TPRC.

[103] Rogier Wildeboer, Paul Southern, and Quentin Pankhurst. "On the reliable measurement of specific absorption rates and intrinsic loss parameters in magnetic hyperthermia materials". In: *Journal of Physics D: Applied Physics* 47 (Nov. 2014), p. 495003. DOI: 10.1088/0022-3727/47/49/495003.

[104] Kai Wu et al. "Magnetic nanoparticles in nanomedicine: a review of recent advances". In: *Nanotechnology* 30 (Sept. 2019). DOI: 10.1088/1361-6528/ab4241.

[105] Qi Yang et al. "Design of Functional Magnetic Nanocomposites for Bioseparation". In: *Colloids and Surfaces B: Biointerfaces* 191 (July 2020), p. 111014. ISSN: 0927-7765. DOI: 10.1016/j.colsurfb.2020.111014. URL: https://www.sciencedirect.com/science/article/pii/S0927776520302447 (visited on 08/27/2024).

[106] Mohsen Khodadadi Yazdi et al. "16 - Magnetic nanoparticles in cancer therapy". In: *Magnetic Nanoparticle-Based Hybrid Materials*. Ed. by Andrea Ehrmann et al. Woodhead Publishing Series in Electronic and Optical Materials. Woodhead Publishing, 2021, pp. 425–445. ISBN: 978-0-12-823688-8. DOI: https://doi.org/10.1016/B978-0-12-823688-8.00025-9. URL: https://www.sciencedirect.com/science/article/pii/B9780128236888000259.

[107] Ali Yousefpour, Mehdi Hojjati, and Jean-Pierre Immarigeon. "Fusion Bonding/Welding of Thermoplastic Composites". In: *Journal of Thermoplastic Composite Materials - J THERMOPLAST COMPOS MATER* 17 (July 2004), pp. 303–341. DOI: 10.1177/0892705704045187.

[108] X. Zhang et al. "Theoretical and experimental analysis of magnetic inductive heating in ferrite materials". In: *Journal of Applied Physics* 93 (June 2003), pp. 7124–7126. DOI: 10.1063/1.1557309.

A

Differential Scanning Calorimetry of CrO2

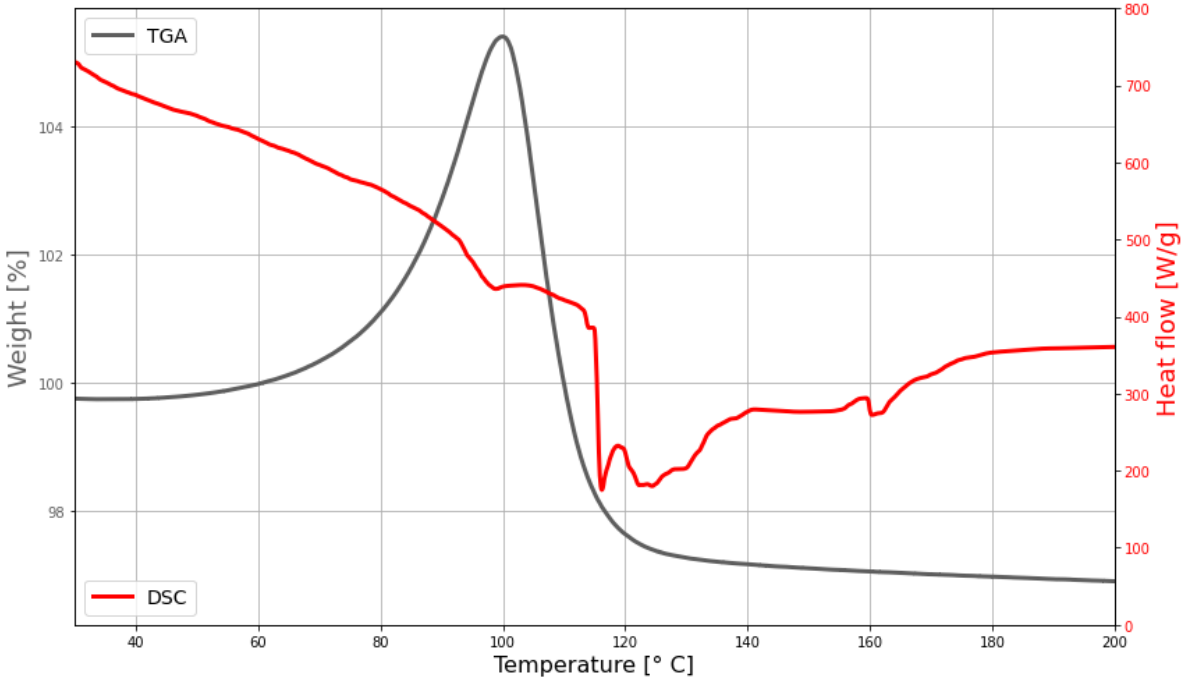

Figure A.1: Plot comparing TGA and DSC measurements for CrO2 nanopowder. The minimum of the heat flow curve deriving from DSC (116.18° C) shows a 2% error difference with the verified Curie temperature of CrO_2 obtained from TGA (113.85° C). This indicates that heat flow curves might provide a good indication of the Curie temperature as an endothermic peak (also named "lambda transition").

B

Standard TGA of CrO2

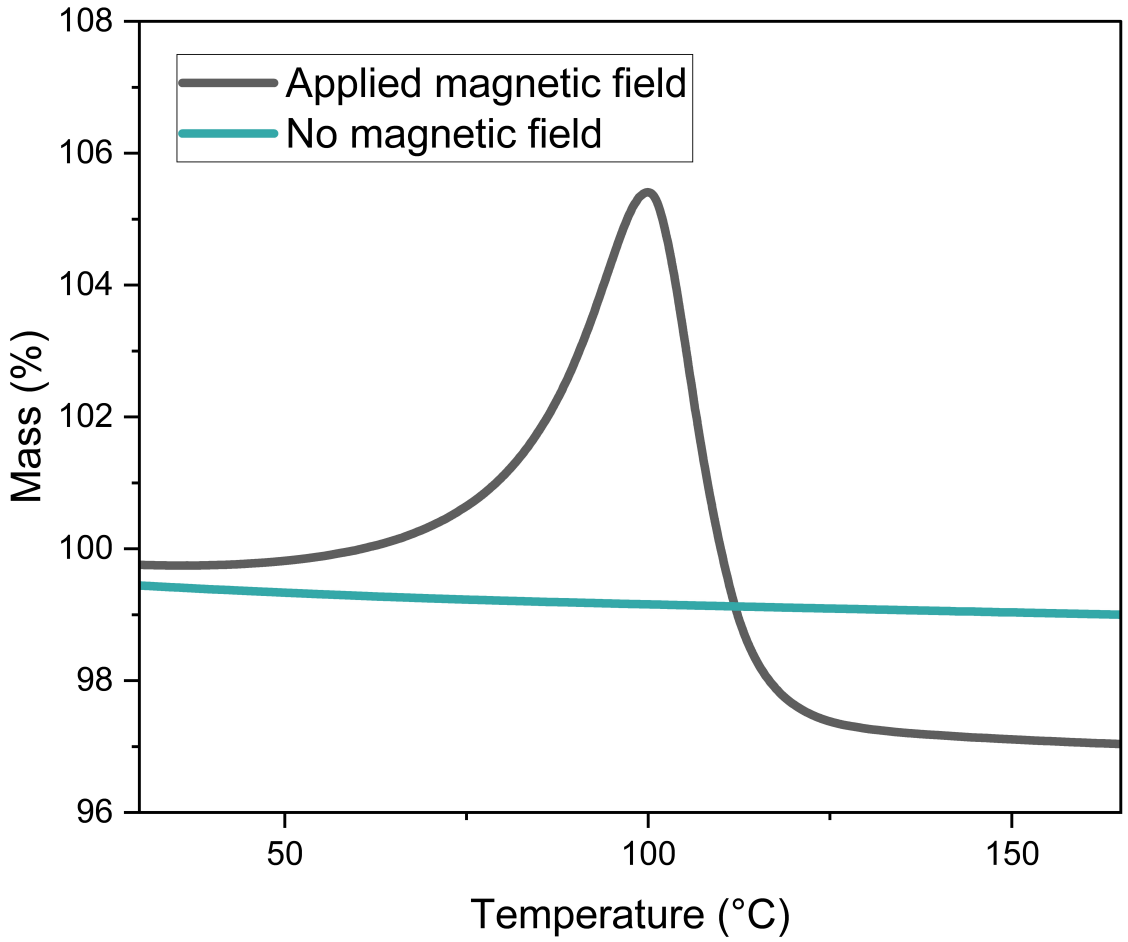

Figure B.1: Plot comparing TGA of CrO2 nanopowder with and without applied magnetic field, heating rate 5° C/min

C

Literature review of Ni-Zn ferrites

Table C.1: Summary of properties of Nickel Ferrite nanoparticles found in literature

Synthesis technique	**Fe:Ni ratio**	**NP size(s) [nm]**	**Curie temperature [°C]**	**Saturation magnetization [emu/g]**	**Reference**
Ball milling + thermal annealing	2:1	10, 12, 31	517	24	[66]
Thermal decomposition + seed growth	2.69:0.31	8-18 nm		73-100	[48]
	2.57:0.43				
	2.30:0.70				
	2.14:0.86				
	2.69:0.31				
Co-precipitation	2:1	8-18 nm		9-40.5	[54]
Co-precipitation	02:01	8-20 nm	477-530	20-35	[41]

Table C.2: Summary of properties of Nickel-Zinc Ferrite nanoparticles found in literature (part 1)

Synthesis technique	Ni:Zn ratio	NP size(s) [nm]	Curie temperature [° C]	Saturation magnetization [emu/g]	Reference
Co-precipitation	0.75:0.25	44	177-80	35-1.4	[95]
	0.5:0.5	47			
	0.25:0.75	63			
	0.20:0.80	71			
	0.15:0.85	58			
	0.10:0.90	52			
	0.05:0.95	66			
	0:1	66			
Sol-gel	0.65:0.35	21.5	431	74.3	[45]
Co-precipitation + annealing	0.5:0.5	10.6		26.09	[88]
	0.6:0.4	11.8		32.76	
	0.7:0.3	12.3		41.69	
Co-precipitation	1:0	30.51	597	46	[86]
	0.8:0.2	31.16	492	59	
	0.6:0.4	30.6	387	68	
	0.4:0.6	30.71	269	59	
	0.2:0.8	28.56	89	18	
	0:1	29.76*			
Solid phase synthesis + annealing	1:0		584		[6]
	0.8:0.2		480		
	0.7:0.3		416		
Co-precipitation	01:00	32-57		65	[38]
	0.9:0.1		599	65	
	0.8:0.2		566	64	
	0.7:0.3		547	62	
	0.6:0.4		523	60	
	0.5:0.5		461	57	
	0.4:0.6		431	57	
	0.3:0.7		399	54	

Table C.3: Summary of properties of Nickel-Zinc Ferrite nanoparticles found in literature (part 2)

Synthesis technique	Ni:Zn ratio	NP size(s) [nm]	Curie temperature [° C]	Saturation magnetization [emu/g]	Reference
Co-precipitation	0.7:0.3	8-12	~270		[100]
	0.5:0.5		~210		
	0.4:0.6		~170		
	0.3:0.7		~160		
Microemulsion	1:0	1	550	0.59	[46]
	0.8:0.2	1-2	260	1	
Co-precipitation	0.75:0.25	15	~270		[33]
Solid phase synthesis + sol-gel autocombustion	0.2:0.8	95-45	300-330	20-75	[99]
	0.4:0.6				
	0.6:0.4				

D

MagneTherm software

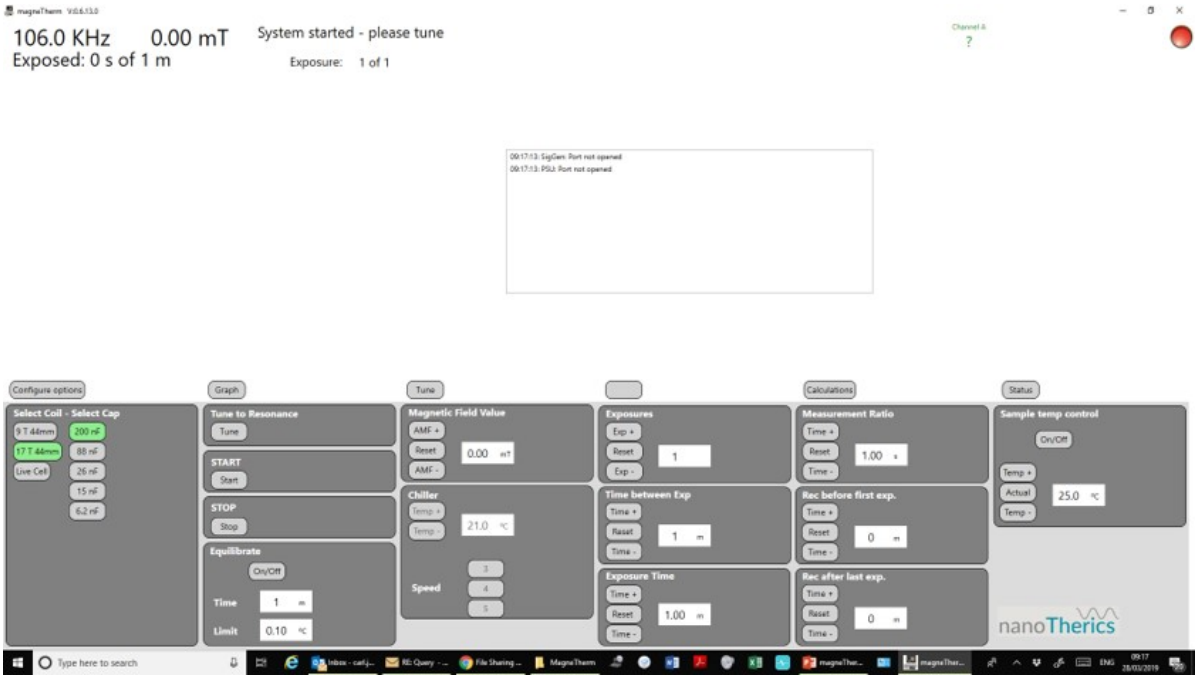

Figure D.1: MagneTherm software for control of induction heating parameters

E

Heating of induction coil

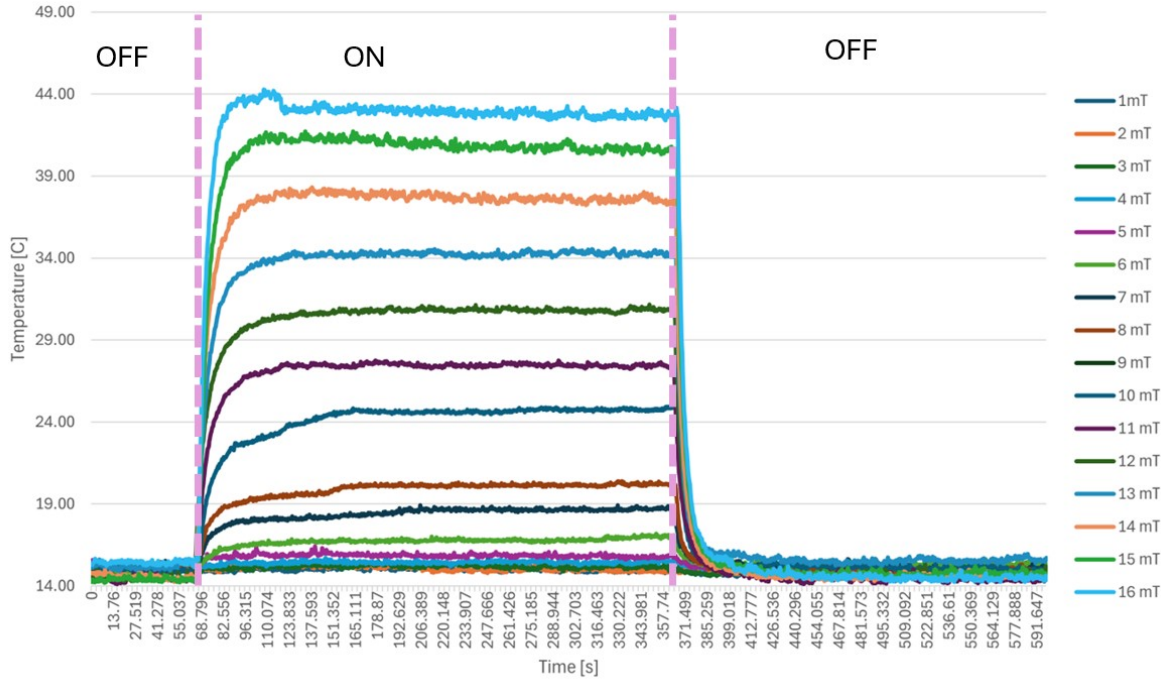

Figure E.1: Heat generation from induction coil, 992 kHz, 16 mT, Measured with FLIR thermal camera. Coil ON indicates exposure to AMF

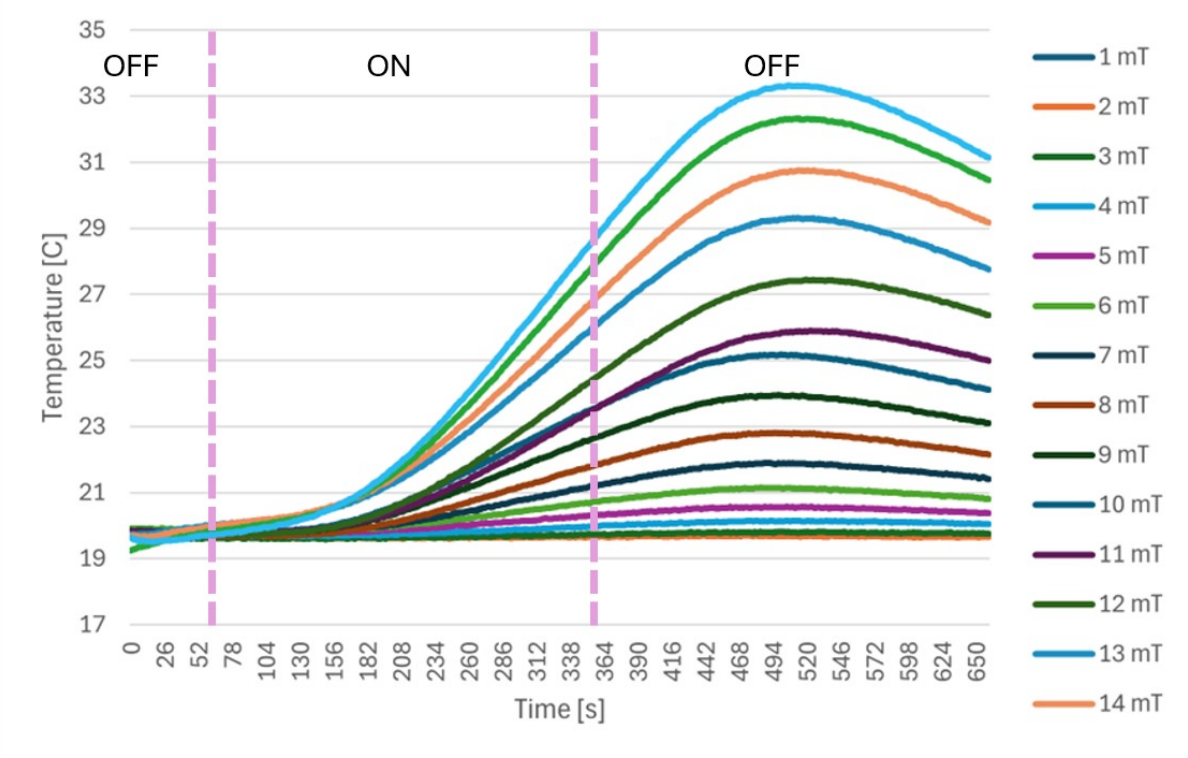

Figure E.2: Temperature increment vs. time for a non-magnetic sample (silicone oil) exposed to AMF, 992 kHz, 16 mT, for 5 minutes. Measured with FLIR thermal camera. Coil ON indicates exposure to AMF.

F

SQUID magnetometry

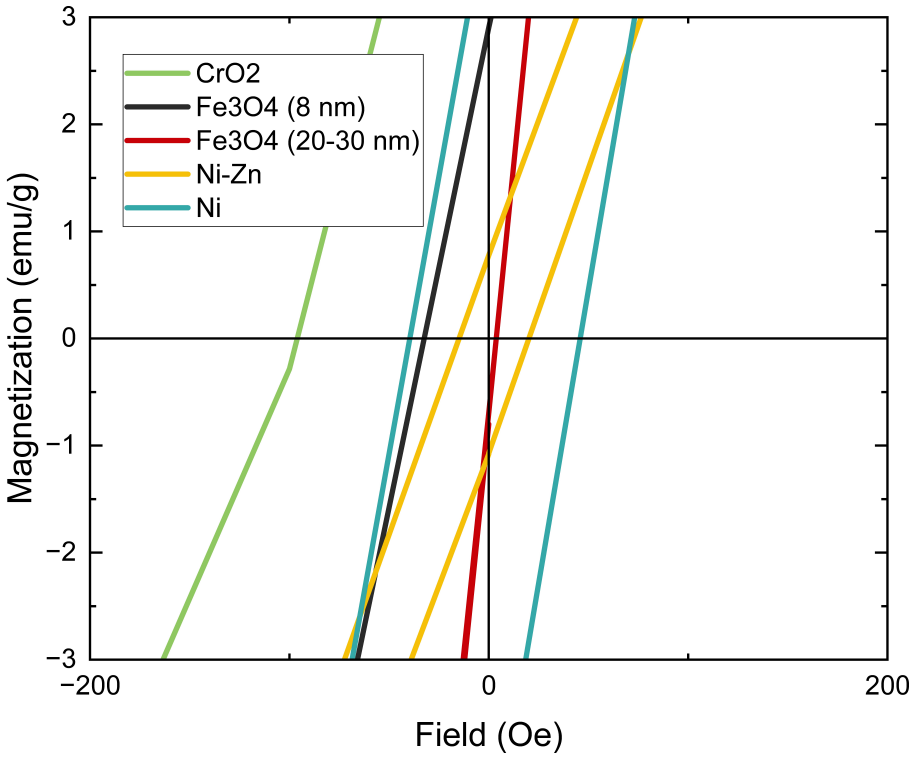

Figure F.1: Magnetization curves of magnetic nanoparticles obtained from SQUID equipment. The graph is enlarged to visualize coercivity and retentivity.